Peridynamic Modeling of Crystal Plasticity with an Adaptive Dynamic Relaxation Solver

by

Jiangyi Luo

A dissertation submitted in partial fulfillment
of the requirements for the degree of
Doctor of Philosophy
(Mechanical Engineering)
in the University of Michigan
2019

Doctoral Committee:

Associate Professor Vikram Gavini, Co-Chair
Associate Professor Veera Sundararaghavan, Co-Chair
Assistant Professor Yue Fan
Associate Professor Emmanuelle Marquis

Jiangyi Luo

jiangyi@umich.edu

ORCID iD: 0000-0001-6101-0497

© Jiangyi Luo 2019

All Rights Reserved

To my beloved parents & teachers

ACKNOWLEDGEMENTS

Foremost, I would like to express my sincere gratitude to my dissertation chair Professor Veera Sundararaghavan. He consistently provided me a large amount of freedom in research and allowed my own thinking, in the meantime, steering me in the right direction. His office door was always open whenever I had a question about my research or ran into a trouble in life. He encouraged me a lot during the darkest time when I was in depression. He has always been a source of inspiration and guidance throughout my stay at the University of Michigan. His optimism, patience, enthusiasm, and immense knowledge have helped me the most in the successful completion of the present work.

I also wish to thank Professor Vikram Gavini for his insightful instructions on my preparation of thesis. His hard questions on basic theories encouraged me to widen my research from various perspectives. Same gratitude to my other two committee members, Professor Emmanuelle Marquis and Professor Yue Fan. Thanks for all your consideration and help.

My sincere thanks also goes to all my lab mates, in particular, Dr. Sriram, Dr. Shardul, Dr. Sun Shang, Siddhartha, and Aaditya for offering me continued support in research and leading me working on diverse exciting projects.

Finally, I must express my very profound gratitude to my parents for their continuous encouragement and unfailing support throughout my years of study including the process of researching and writing this thesis. I am thankful to all the teachers through my life.

The work presented here was funded by Office of Naval Research (ONR) grant N00014-12-1-0013 and National Science Foundation CAREER award (CMMI-0954390).

TABLE OF CONTENTS

LIST OF FIGURES

Figure

LIST OF TABLES

Table

LIST OF APPENDICES

Appendix

ABSTRACT

A primary challenge in modeling polycrystalline materials under large deformation is capturing strong strain localizations, in the form of micro-scale sharp shear bands. Classical numerical approaches such as finite element methods are inefficient in handling discontinuities because continuum mechanics approximations become inaccurate. Peridynamics, introduced as an alternative integral formulation for continuum mechanics, has attracted significant attention in solid mechanics for its special treatment in the presence of high gradients and discontinuities. In addition, peridynamic models are powerful in predicting damage nucleation and propagation with an intrinsic characteristic length scale. Given this background, a peridynamic implementation of crystal plasticity with an adaptive dynamic relaxation method is presented in this thesis.

Specifically, a parallelized code for non-ordinary state-based peridynamics via Newmark's dynamic method with artificial damping is developed in this work. Elasticity problems are tested first in order to understand numerical behavior of the algorithm comprehensively. A rate-independent crystal plasticity model is then introduced to conduct simulations of planar polycrystalline microstructures under plane strain pure shear and compression. The peridynamic solver is compared with the crystal plasticity finite element method for predicting the stress and strain fields, texture, and homogenized stress-strain response. Sharper and more numerous shear bands are observed in the peridynamic model. Emphasis is placed on the accuracy and efficiency of the peridynamics solver via development of new higher order approxima-

tion schemes for the deformation gradient and new boundary condition treatments. We have also proposed a new solution for achieving numerical stability based on the stress-point method. The thesis thus presents the first three-dimensional polycrystal plasticity simulations using peridynamics theory with strain fields and texture compared against experiments and published literature.

CHAPTER I

Introduction

Developing computational models for microstructure evolution of polycrystalline alloys in industrial applications remains an active challenge. Recent experiments have observed micro-scale strain localizations, in the form of fine shear bands, on the surface of polycrystals undergoing large deformation using a combination of the scanning electron microscopy and digital image correlation [4, 5]. These micro-scale shear bands can act as precursors for damage and failure. New theories such as strain gradient plasticity have been proposed and attempting to attribute the non-homogeneous strain localization to geometrically necessary dislocations as a result of strong local strain gradients [6]. However, other factors such as grain sizes and inter-grain strain incompatibilities due to grain boundaries are also pointed out as factors for the initialization of shear bands [5]. Therefore, considering the complexity of fracture problems and absence of robust theoretical basis, no satisfactory numerical predictions have been obtained that compare well to experimental results on the formation of micro-scale strain localizations.

In the classical solid mechanics, fundamental properties such as stress and strain are defined as limits on an infinitesimally small area. These limit definitions work perfectly as long as the computational field is smooth and differentiable. Nevertheless, as discontinuities and singularities emerge, e.g., cracks and sharp corners, the

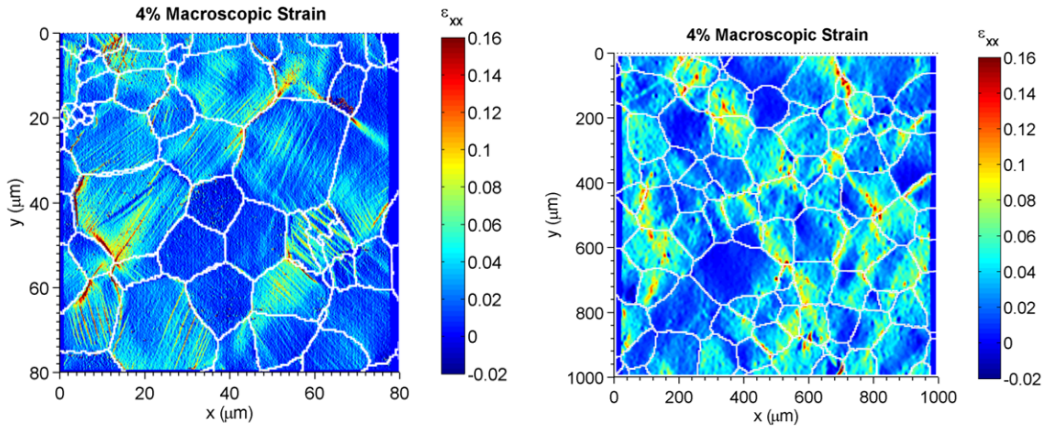

(a) (b)

Figure 1.1: *Tensile strain fields of a magnesium alloy microstructure for two different heat treatments. Experiment data is obtained using the micro-scale digital image correlation technique [4]. Fine shear bands due to strain localizations are observed in (a).*

continuum model fails and fracture mechanics is necessarily applied. Some solutions are to introduce stress intensity factors around crack tips and then to estimate stress at a point by functions containing these factors [7]. Though a plastic region may be brought in around the crack tip due to stress concentration, the model out of the crack is still based on the continuum assumption.

Element-based numerical programs, such as the finite element method (FEM), play an important role in computational solid mechanics. One of challenges when employing FEM to fracture models is that the element-based mesh will, with a strong possibility, become tangled or degenerate during large deformation and cannot produce correct values. Hence, more flexible ways to eliminate the reliance on elements naturally come into view. These are called meshfree methods [8], in which domains are discretized as arbitrarily separate particles and original properties such as the deformation gradient and strain are assigned to single nodes taking upon interactions of each particle within a prescribed horizon rather than mesh elements. Consequently, the process of breaking bonds between particles can be regarded as an essential and natural way to simulate cracks growing and propagating. Fig. 1.2 is a simple illus-

tration of meshfree methods.

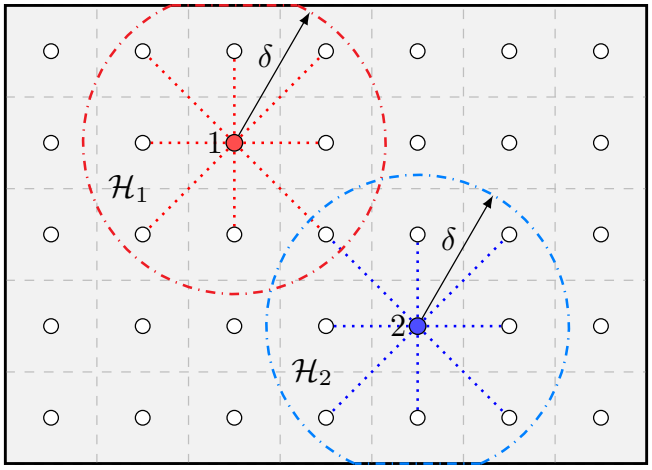

Figure 1.2: *Particle interactions in the meshfree model. Each particle occupies a finite volume and only interacts with other particles (connected with dotted lines) within a horizon with radius δ. Two particles 1,2 and their corresponding horizons are plotted by red and blue, respectively.*

Peridynamics (PD), introduced as an alternative integral formulation for continuum mechanics, is a relatively new theory that naturally lends itself to the use of meshfree and particle-based discretizations [9, 10]. This non-local method calculates the response of material at a particle by tracking the motion of surrounding particles. The first version of peridynamics is bond-based, in which forces between particles are assumed pairwise, equal but direction-reversed. However, in many cases it is oversimplified with a fixed Poisson's ratio as 1/3 and unable to handle plasticity due to its sensitivity of volumetric deformation. To address the above issues, a more generalized state-based peridynamic model is afterwards proposed [10]. Forces between particles are represented by force states, which can be computed form conventional constitutive models. Thus, the nonlocality is conveniently introduced without the need to alter the underlying constitutive equations. The deformation measure in this model is computed by integrating motion of particles across a finite horizon via the correspondence principle. State-based peridynamics has been proven to be useful and efficient in many recent studies, which is able to give a better view of discontinuities

than continuum mechanics [11, 12, 13, 14, 15, 16].

Crystal plasticity (CP) theory describes dislocation motion and their interaction through continuum laws such as flow and hardening rules. Finite element analysis of polycrystalline aggregates using crystal plasticity theory [17, 18, 19, 20, 21, 22] has allowed better understanding of mechanical properties of polycrystalline alloys. In CPFE models, grains are discretized into finite-volume elements where the crystal plasticity formulations are applied on each element to compute mechanical responses, crystallographic slips, and reorientation of grains or texturing at both microscopic and macroscopic scales [23, 24]. The method has been successful in predicting texture development during deformation processing and has been used for alloy optimization through texture control - leading to a variety of applications - including development of high strength aluminum alloys [25, 26, 27], soft magnetic materials with low hysteresis [28, 29] and multifunctional alloys with high field induced strains [30, 31, 32] . While crystal plasticity has been validated in the past against macroscopic texture measurements [33, 34, 35], modern experimental tools such as SEM-DIC [36, 4] and high resolution EBSD [37, 38] reveal a hidden landscape of micro–scale plastic phenomena that have not yet been predicted through crystal plasticity finite element methods. Such features include the size dependent, non–smooth and highly localized banding patterns associated with crystal plasticity (as seen in Fig. 1.3). The localizations have now been observed in a variety of experiments including micropillar compression [39], nanoindentation [40], and in-situ cyclic loading [41] known to act as precursors for failure. These localizations happen even at small strains at the sub–grain level and generally follow crystallographic directions, differentiating them from macroscopic non–crystallographic shear bands that occur at large deformations. These small scale localizations are typically modelled using dislocation dynamics [42, 43, 44] or molecular dynamics [45, 46] models that invoke non–local interactions. However, computational complexity limits applications of such techniques

to small volumes and high loading rates. However, localization phenomena of interest in this proposal occur at slow loading rates and at microstructural scales. The key issues are explained below:

1. **Band localizations** Slip localization naturally occurs in deforming polycrystalline aggregates in the form of lamellar bands of fractions of microns in thickness [47]. The wavelengths of the slip bands decrease with increasing plastic deformation while the thickness increases [48]. Early work have generally associated localizations with degradation in material strength, in the form of strain softening [49, 50]. Indeed, instabilities such as Lüders band are preceded by strain softening and advance by formation of new slip bands parallel to the old ones. However, in–situ SEM–DIC experiments under monotonic loading reveal sub–grain slip localizations under positive work-hardening rates [4, 51]. The analytical work of Asaro and Rice [52] showed the possibility that localization indeed can occur with positive hardening rates due to multiple slip interactions that arise in crystal plasticity theory. Such slip localization cannot be naturally modeled in crystal plasticity finite element models. Existing works use prescribed perturbations to trigger slip band formation. Such perturbations consist of material imperfections, geometric inhomogeneities, mesh elements with variable properties or perturbed boundary conditions [53, 54, 55, 56]. The distribution of perturbation elements has a major influence on slip banding behavior [48]. Numerical approach also plays a role in the predicted localizations. When using standard finite elements, the element size determines the size of shear bands; producing mesh dependent models [57]. Various enhancements of finite element method have been studied in the past to address this issue. Early approaches involved development of traction-separation softening laws whose slope was made to depend on the element size [58]. In the limiting case of zero element size, the localization appears as a sharp discontinuity.

Later approaches such as the extended finite element methods (X-FEM, [59]) or variational multiscale methods (VMM, [60]) directly represented sharp discontinuities on coarse elements by enriching the finite element interpolations using fine–scale strain functions. While analytical work shows that localizations should naturally happen, none of these methods are capable of initiating slip band localization naturally without any imperfection or initiation criterion.

2. **Size effects** Size effects play an important role in the plastic response [61, 62]. Such effects include Hall-Petch relationship [63, 64], strain-gradient strengthening [65], indentation size dependent pop-in stress [66] etc. Traditional crystal plasticity models [67] were developed largely without a connection to grain size and shape effects. Incorporation of grain size effect into constitutive models for single slip began with Armstrong [68] who modified the Hall–Petch equation to correspond to the flow stress on a slip system (the 'micro–Hall–Petch relation'). The interrelationship between grain size and texture was not considered until Weng [69] employed the mean grain size in the equation for slip system resistance through the micro–Hall–Petch relation[70, 71]. However, such approximations are incapable of accurately modeling strain and orientation gradients that dictate the size effect. Effect of free surfaces is another important aspect of metal plasticity. Micropillar compression experiments [72, 73, 74] reveal plastic behavior characterized by strain bursts under stress controlled conditions. Strain bursts are associated with the strain gradient in the internal local region, as indicated by time-resolved Laue diffraction [75]. The strain gradients are strongly affected by the free surfaces, for example, just coating the surface tends to inhibit strain bursts [76, 77]. Since no inherent length scales are invoked in conventional crystal plasticity, they have difficulties in predicting such size dependent behavior.

The development of slip bands and size effect in a ductile crystalline metal is a

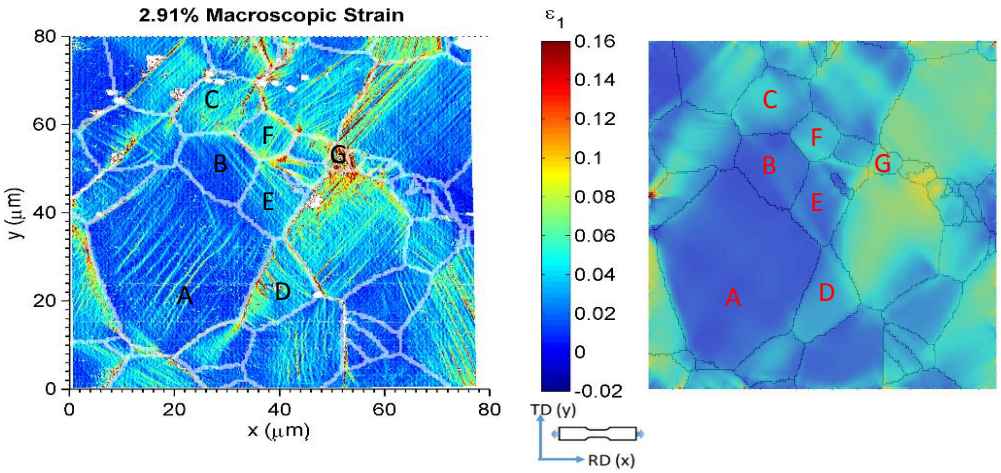

Figure 1.3: *(left) Tensile strain field in a WE43 Magnesium alloy microstructure as experimentally seen using micro-scale digital image correlation ([4], Prof. S. Daly, personal communication). Strains are seen to localize into intense localization bands within grains. (right) Crystal plasticity finite element simulations using the PI's open source code PRISMS-Plasticity reveals homogeneous strain fields that do not capture these localizations.*

non-local phenomenon, i.e. the crystallographic slip at a material point is influenced by the deformation of material within a finite neighborhood. A significant body of recent work has employed gradient theories [78, 79, 80, 81, 82] to model size effects. These models typically consider strain gradient dependent hardening terms in crystal plasticity that simulate the evolution of geometrically necessary dislocations (GNDs). However, such second order gradient theories do not retain sufficient long–range interactions to model width and spacing of slip bands accurately. As Asaro and Rice's early work [52] shows, the localization can happen even in local–theories without the need to invoke gradient terms. Experiments reveal localizations even under low strain homogeneous loading where GNDs are minimally active [4]. This suggests that long range mechanisms acting at the scale of at least the nearest–neighbor grains impact the localization process. Presumably, inclusion of higher-order strain gradients could improve the constitutive description, but this would require significant amount of calibration at the constitutive level – necessitating costly experiments for detailed dislocation density characterization[37, 38].

In this thesis, we propose an alternate route to predict strain localizations. We do not enforce non-locality at the constitutive level. Instead, non-locality is introduced at the level of the governing equilibrium equations via the method of peridynamics [9, 83]. In peridynamics, the body is represented as a set of particles interacting via an integral form of the linear momentum balance equation. A state-based theory of peridynamics [10] will be used where the forces in the bonds between particles are computed from stress tensors obtained from crystal plasticity. The stress tensor at a particle, in turn, is computed using non–local strains calculated by tracking the motion of surrounding particles over a distance horizon. Compared to gradient plasticity theories, this approach is simpler because it can employ popular crystal plasticity models of 'local' nature while avoiding the need to invoke higher order terms at the constitutive level. Our approach has some precedent in the form of diffusion-reaction type models of dislocation plasticity [84, 85] that have displayed the capability to model localization patterns using gradient terms at the level of governing equations. However, such models have not yet been applied to model slip band localizations at the mesoscale. Another approach that might be competitive are phase field approaches that model localization using a multi-well potential with gradient terms [86]. However, the present peridynamics approach is a more straightforward approach since it avoids the need for any additional constitutive model development.

Although peridynamics has been proven effective and robust in prediction of discontinuities and damage, there are still some intrinsic issues of its numerical implementations, among which are zero-energy modes and non-trivial treatment of boundary conditions [87, 88, 89, 90]. In 1D problems, the correspondence principle relates three displacements to one deformation gradient. This results in a null space where some deformations do not play a role in the computed gradient. Therefore, different techniques have been applied. Recent papers have attempted to resolve the hourglass-like instability using fictitious springs between particles and hourglass force

terms [87, 91]. However, these methods have failed to completely remove the instability and, in addition, employed coefficients or formulations are sensitive to the mesh size and chosen on a case-by-case basis. Another branch of methods is to modify the influence functions, either to provide an average-weighted displacement [89] or to use higher-order approximations to solve non-local peridynamic equations[92, 93]. These methods are effective in increasing the accuracy with enlarged horizons, nevertheless, zero-energy modes are still in the deformation gradient due to the absence of the center particle.

In the current work, we propose the use of stress points to mitigate the zero–energy mode. The stress-point approach has been proposed in the past for other particle methods such as smoothed particle hydrodynamics but for tensile instability [94, 95]. The idea is straightforward. Addition of even one more independent stress point in 1D problems leads to two gradients and three displacements which significantly reduces the null space. This stress-point peridynamic model is first demonstrated in a simple 1D problem and then applied to higher-dimensional problems. Using these numerical examples, we show that zero-energy-mode oscillations in solution are completely damped.

In addition to zero-energy modes, the non-ordinary state-based peridynamics also experiences the difficulty of enforcing boundary conditions [89]. Since peridynamics utilizes an integral–form equation of motion, different from the partial differential equations in the conventional continuum mechanics, the enforcement of kinematic constraints at boundaries is not able to follow the standard way. Special numerical boundary treatments have been tried in the other particle/meshfree approaches.

Another numerical issue, not for peridynamics but the crystal plasticity model, is its demanding computation cost of calculating the Jacobian matrix, i.e., the tangent modulus [22]. A recent study has shown the advantages of CPPD models on the computation cost over CPFE models based on the implicit Newton-Raphson solver

[21]. However, both models are time-consuming, though implicit methods are traditionally favored compared to explicit dynamic methods for their accuracy at larger time steps [96, 97, 98]. Therefore, this thesis presents a fully explicit implementation of state-based peridynamics for modeling quasi-static deformation of polycrystals. An adaptive dynamic relaxation method for quasi-static PD simulations as proposed by Kilic [99] is adopted, where an artificial damping ratio estimated from Rayleigh's quotient is selected to dampen the system leading to a steady-state solution. The critical time step is approximated by a numerical analysis of hyperbolic partial differential equations. Accuracy and effectiveness of this new dynamic CPPD model will be demonstrated with numerical examples.

There are seven chapters in this thesis with the introduction as Chapter I. Chapter II proposes the PD model with an adaptive dynamic relaxation solver. In this chapter, formulations of state-based peridynamics, the adaptive dynamic relaxation method, and their numerical discretization schemes will be reviewed. Numerical tests on 1D and 3D elastic problems are followed to prove the accuracy and stability of this new model. The crystal plasticity constitutive model will replace the elasticity model in Chapter III, where we conduct simulations for planar polycrystalline microstructures under plane strain pure shear and compression, respectively. The stress field distribution, texture formation, and homogenized stress-strain response predicted by the classical CPFE model and the new dynamic CPPD model are compared afterwards. In addition, we perform compression tests of three polycrystals with different orientation distributions to study the nature of localization bands identified from the dynamic CPPD method. Comments will be made on each class of numerical examples. A higher-order approximation approach is presented in Chapter IV to stabilize zero-energy modes in peridynamic solutions. Convergence has been observed in the planar CPPD results across a range of different horizon sizes. We focused on extending the new dynamic CPPD model to 3D polycrystal problems with comparison

to the experimental observations in Chapter V. Chapter VI proposes an improved stress-point method to stabilized the numerical oscillations in peridynamic solutions. Finally, conclusions of the this work and some future projects are discussed in the last chapter.

CHAPTER II

Non-Ordinary State-Based Peridynamics with an Adaptive Dynamic Relaxation Solver (PD-ADRS)

2.1 Non-Ordinary State-Based Peridynamics

The non-ordinary state-based peridynamic model is first presented by Silling [10] in 2007, which is a nonlocal integral reformulation of the continuum theory. Unlike bond–based peridynamics that is restricted to a single Poisson's ratio, the state–based peridynamic theory can be generalized to include materials with any Poisson's ratio. In addition, it is possible to apply classical constitutive material models in the state-based peridynamic framework. A review of important definitions of the state-based theory is provided below.

2.1.1 Vector states

A vector state is a function $\underline{\mathbf{A}}\langle\cdot\rangle$ mapping vectors to vectors: $\boldsymbol{\xi} \rightarrow \underline{\mathbf{A}}\langle\boldsymbol{\xi}\rangle$. Its concept is similar to a second order tensor. However, there are three main differences: 1) A state is not generally a linear function of $\boldsymbol{\xi}$. 2) A state can be a discontinuous function of $\boldsymbol{\xi}$. 3) The real Euclidean space of states is infinite-dimensional while second order tensors have dimension 9.

Therefore, vector states are more general than second order tensors. In other

words, second order tensors are a special case of vector states. This idea is clearly presented in their conversions, which are called "expansion", from second order tensors to vector states, and "reduction", in the reverse direction.

It is very straightforward to expand a second order tensor $\mathbf{Q}$ into a vector state $\underline{\mathcal{E}}(\mathbf{Q})$. The definition is

$$\underline{\mathcal{E}}(\mathbf{Q})\langle\boldsymbol{\xi}\rangle = \mathbf{Q}\boldsymbol{\xi}, \quad \forall\boldsymbol{\xi}. \tag{2.1}$$

However, more caution is needed in reducing a vector state into a second order tensor. The first step is to define a tensor product of two states $\underline{\mathbf{A}}$ and $\underline{\mathbf{B}}$, which is

$$\underline{\mathbf{A}} * \underline{\mathbf{B}} = \int_{\mathcal{H}} \omega(\boldsymbol{\xi})\underline{\mathbf{A}}\langle\boldsymbol{\xi}\rangle \otimes \underline{\mathbf{B}}\langle\boldsymbol{\xi}\rangle dV_{\boldsymbol{\xi}}, \tag{2.2}$$

where $\omega(\boldsymbol{\xi})$ is called an influence function[1], which is supposed to be nonzero only on horizon $\mathcal{H}$; symbol $\otimes$ represents the dyadic product of two vectors (for example, $\mathbf{C} = \mathbf{a} \otimes \mathbf{b}$ can be rewritten as $C_{ij} = a_i b_j$ in Einstein notation); $dV_{\boldsymbol{\xi}}$ is the finite volume of $\boldsymbol{\xi}$ in the horizon $\mathcal{H}$.

Assume the reference position vector state is $\underline{\mathbf{X}}\langle\boldsymbol{\xi}\rangle = \boldsymbol{\xi}$, then a shape tensor $\underline{\mathbf{K}}$ is defined as

$$\mathbf{K} = \underline{\mathbf{X}} * \underline{\mathbf{X}}. \tag{2.3}$$

Note that the shape tensor $\mathbf{K}$ is symmetric and positive definite, hence $\mathbf{K}^{-1}$ exits.

With the help of the shape tensor, reducing a vector state $\underline{\mathbf{A}}$ to a second order tensor $\mathcal{R}(\underline{\mathbf{A}})$ is then defined as

$$\mathcal{R}(\underline{\mathbf{A}}) = (\underline{\mathbf{A}} * \underline{\mathbf{X}})\mathbf{K}^{-1}. \tag{2.4}$$

[1] ω is originally defined as a vector state function, i.e., $\underline{\omega}\langle\cdot\rangle$. In this thesis, it is more convenient to use it as a simple scalar function on vector $\boldsymbol{\xi}$. In addition, it is also called weight function or kernel function in some other references.

It can be demonstrated that for any second order tensor $\mathbf{Q}$, $\mathcal{R}(\underline{\mathcal{E}}(\mathbf{Q})) = \mathbf{Q}$:

$$\begin{aligned}
\mathcal{R}_{ij}(\underline{\mathcal{E}}(\mathbf{Q})) &= \mathcal{R}_{ij}(\mathbf{Q}\boldsymbol{\xi}) \\
&= \left(\int_{\mathcal{H}} \omega(\boldsymbol{\xi}) \big(Q_{ip}\xi_p\big)\xi_k dV_{\boldsymbol{\xi}} \right) K^{-1}_{kj} \\
&= Q_{ip} \left(\int_{\mathcal{H}} \omega(\boldsymbol{\xi})\xi_p\xi_k dV_{\boldsymbol{\xi}} \right) K^{-1}_{kj} \\
&= Q_{ip} K_{pk} K^{-1}_{kj} \\
&= Q_{ip}\delta_{pj} \\
&= Q_{ij}. \qquad (2.5)
\end{aligned}$$

Nevertheless, the expansion of the reduction of a vector state is not in general the state itself, i.e., $\underline{\mathcal{E}}(\mathcal{R}(\underline{\mathbf{A}})) \neq \underline{\mathbf{A}}$, always.

Typically, a vector state $\underline{\mathbf{A}}$ can be also a function of position $\mathbf{x}$, time t, and another vector state $\underline{\mathbf{B}}$. It is called a state field denoted by

$$\underline{\mathbf{A}}\langle\boldsymbol{\xi}\rangle = \underline{\mathbf{A}}[\mathbf{x}, t](\underline{\mathbf{B}})\langle\boldsymbol{\xi}\rangle. \qquad (2.6)$$

Abbreviations should be applied in many situations, though.

At the end of this section, it is necessary to introduce the dot product of two vector states and derivatives on vector states. The dot product of two vector states $\underline{\mathbf{A}}$ and $\underline{\mathbf{B}}$ is defined as

$$\underline{\mathbf{A}} \bullet \underline{\mathbf{B}} = \int_{\mathcal{H}} \underline{A}_i \underline{B}_i dV_{\boldsymbol{\xi}}, \qquad (2.7)$$

where $\underline{A}_i$ and $\underline{B}_i$ are the vector components of $\underline{\mathbf{A}}$ and $\underline{\mathbf{B}}$, respectively.

Suppose Ψ is a function of vector states, i.e., $\Psi = \Psi(\underline{\mathbf{A}})$ and for any states $\underline{\mathbf{A}}$, there exists a state-valued function $\nabla\Psi(\underline{\mathbf{A}})$ satisfying

$$\Psi(\underline{\mathbf{A}} + \Delta\underline{\mathbf{A}}) = \Psi(\underline{\mathbf{A}}) + \nabla\Psi(\underline{\mathbf{A}}) \bullet \Delta\underline{\mathbf{A}} + o(||\Delta\underline{\mathbf{A}}||), \qquad (2.8)$$

where $\Delta\underline{\mathbf{A}}$ is a small increment and $o(||\Delta\underline{\mathbf{A}}||)$ is the higher-order term. Then the state-valued function Ψ is called differentiable and $\nabla\Psi(\underline{\mathbf{A}})$ is the Frechet derivative of Ψ. Note that $\nabla\Psi(\underline{\mathbf{A}})$ is always one-order higher than Ψ. For instance, if Ψ is a second-order tensor-valued function, $\nabla\Psi$ then produces third-order tensors.

2.1.2 Basic peridynamic formulation

Consider a material point $\mathbf{x}$ in the reference configuration which can only interact with its neighboring points $\mathbf{x}'$ in a self-center horizon $\mathcal{H}_{\mathbf{x}}$ with a finite radius δ. Given a displacement field $\mathbf{u}$, the current configuration is then represented by $\mathbf{y} = \mathbf{x} + \mathbf{u}$. Let the initial physical domain be $\mathcal{B}_0$ at time $t = 0$ while $\mathcal{B}_1$ is the deformed domain, as shown in Fig. 2.1.

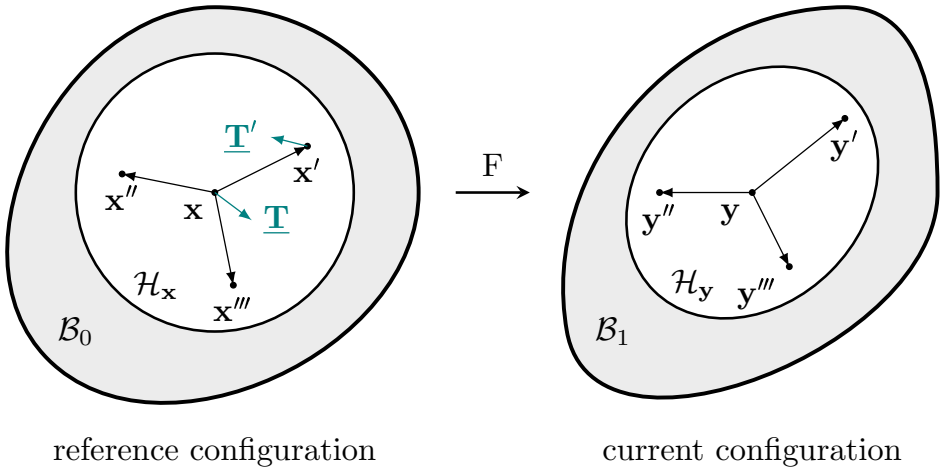

Figure 2.1: *Kinematics of non-ordinary state-based peridynamics. Particle* $\mathbf{x}$ *is bonded to neighboring particles (*$\mathbf{x}'$*,* $\mathbf{x}''$*, and* $\mathbf{x}'''$*) within a region* $\mathcal{H}_{\mathbf{x}}$*. Under the deformation, particle* $\mathbf{x}$ *maps to particle* $\mathbf{y}$ *and this process can be described by a corresponding deformation gradient* $\mathbf{F}$*.* $\underline{\mathbf{T}} = \underline{\mathbf{T}}[\mathbf{x}, t]\langle\mathbf{x}' - \mathbf{x}\rangle$ *and* $\underline{\mathbf{T}}' = \underline{\mathbf{T}}[\mathbf{x}', t]\langle\mathbf{x} - \mathbf{x}'\rangle$ *are force vector states in the reference configuration at particle* $\mathbf{x}$ *and* $\mathbf{x}'$*, respectively. In the non-ordinary state-based peridynamic theory, these two force vector states are not necessarily parallel and can be obtained from the classical stress tensor.*

The deformation vector state $\underline{\mathbf{Y}} = \underline{\mathbf{Y}}[\mathbf{x}, t]\langle\mathbf{x}' - \mathbf{x}\rangle = \mathbf{y}' - \mathbf{y}$ is introduced to describe the local deformation of bond $\boldsymbol{\xi} = \mathbf{x}' - \mathbf{x}$. $\underline{\mathbf{T}}[\mathbf{x}, t]\langle\mathbf{x}' - \mathbf{x}\rangle$ is the force vector state

that particle $\mathbf{x}'$ exerts on particle $\mathbf{x}$. More precisely, the force state is a state field, defined in (2.6), which operates on the bond $\boldsymbol{\xi}$ at particle $\mathbf{x}$ and time t. A general state-based peridynamic constitutive model can be written as

$$\underline{\mathbf{T}}\langle\boldsymbol{\xi}\rangle = \underline{\mathbf{T}}(\underline{\mathbf{Y}})\langle\boldsymbol{\xi}\rangle = \nabla W(\underline{\mathbf{Y}}), \tag{2.9}$$

where W is the strain energy density function and ∇W is its Frechet derivative.

Suppose a body $\mathcal{B}$ is subjected to a body force density $\mathbf{b}$, the energy balance at time t can be expressed as

$$\int_0^t \int_{\mathcal{B}} \mathbf{b} \cdot \dot{\mathbf{u}} dV dt = \frac{1}{2} \int_{\mathcal{B}} \rho \dot{\mathbf{u}} \cdot \dot{\mathbf{u}} dV + \int_{\mathcal{B}} W dV \tag{2.10}$$

where the left-hand side represents total external work, right-hand side are total kinetic energy and strain energy, respectively; $\dot{\mathbf{u}}$ is velocity and ρ is mass density. Differentiating (2.10) by time t results in

$$\int_{\mathcal{B}} \mathbf{b} \cdot \dot{\mathbf{u}} dV = \int_{\mathcal{B}} \rho \ddot{\mathbf{u}} \cdot \dot{\mathbf{u}} dV + \int_{\mathcal{B}} \dot{W} dV \tag{2.11}$$

Focus on the total strain energy term and use (2.7), (2.8), (2.9):

$$\int_{\mathcal{B}} \dot{W} dV = \int_{\mathcal{B}} \nabla W(\underline{\mathbf{Y}}) \bullet \underline{\dot{\mathbf{Y}}} dV = \int_{\mathcal{B}} \underline{\mathbf{T}} \bullet \underline{\dot{\mathbf{Y}}} dV. \tag{2.12}$$

The goal is to adjust (2.12) to be an equation containing $\underline{\mathbf{T}}$ only. The following abbreviations will be used:

$$\underline{\mathbf{T}} = \underline{\mathbf{T}}[\mathbf{x}, t], \quad \underline{\mathbf{T}}' = \underline{\mathbf{T}}[\mathbf{x}', t], \quad \mathbf{u} = \mathbf{u}(\mathbf{x}, t), \quad \mathbf{u}' = \mathbf{u}(\mathbf{x}', t). \tag{2.13}$$

Equation (2.12) then becomes

$$\begin{aligned}
\int_{\mathcal{B}} \underline{\mathbf{T}} \bullet \dot{\underline{\mathbf{Y}}} dV &= \int_{\mathcal{B}} \int_{\mathcal{B}} \underline{\mathbf{T}}\langle \boldsymbol{\xi} \rangle \cdot \dot{\underline{\mathbf{Y}}}\langle \boldsymbol{\xi} \rangle dV_{\boldsymbol{\xi}} dV \\
&= \int_{\mathcal{B}} \int_{\mathcal{B}} \underline{\mathbf{T}}\langle \mathbf{x}' - \mathbf{x} \rangle \cdot (\dot{\mathbf{u}}' - \dot{\mathbf{u}}) dV_{\mathbf{x}'} dV_{\mathbf{x}} \\
&= \int_{\mathcal{B}} \int_{\mathcal{B}} \underline{\mathbf{T}}\langle \mathbf{x}' - \mathbf{x} \rangle \cdot \dot{\mathbf{u}}' dV_{\mathbf{x}'} dV_{\mathbf{x}} - \int_{\mathcal{B}} \int_{\mathcal{B}} \underline{\mathbf{T}}\langle \mathbf{x}' - \mathbf{x} \rangle \cdot \dot{\mathbf{u}} dV_{\mathbf{x}'} dV_{\mathbf{x}} \\
&= \int_{\mathcal{B}} \int_{\mathcal{B}} \underline{\mathbf{T}}'\langle \mathbf{x} - \mathbf{x}' \rangle \cdot \dot{\mathbf{u}} dV_{\mathbf{x}'} dV_{\mathbf{x}} - \int_{\mathcal{B}} \int_{\mathcal{B}} \underline{\mathbf{T}}\langle \mathbf{x}' - \mathbf{x} \rangle \cdot \dot{\mathbf{u}} dV_{\mathbf{x}'} dV_{\mathbf{x}} \\
&= \int_{\mathcal{B}} \int_{\mathcal{B}} \{\underline{\mathbf{T}}'\langle \mathbf{x} - \mathbf{x}' \rangle - \underline{\mathbf{T}}\langle \mathbf{x}' - \mathbf{x} \rangle\} \cdot \dot{\mathbf{u}} dV_{\mathbf{x}'} dV_{\mathbf{x}}. \qquad (2.14)
\end{aligned}$$

A switch of variables $\mathbf{x}$ and $\mathbf{x}'$ is applied in the fourth step above considering both integrations are over the whole body $\mathcal{B}$. Return to (2.11) and reorganize the terms in the integration:

$$\int_{\mathcal{B}} \left(\rho \ddot{\mathbf{u}} - \mathbf{b} + \int_{\mathcal{B}} \{\underline{\mathbf{T}}'\langle \mathbf{x} - \mathbf{x}' \rangle - \underline{\mathbf{T}}\langle \mathbf{x}' - \mathbf{x} \rangle\} dV_{\mathbf{x}'} \right) \cdot \dot{\mathbf{u}} dV_{\mathbf{x}} = 0. \qquad (2.15)$$

The result holds for any velocity $\dot{\mathbf{u}}$ and body $\mathcal{B}$, hence,

$$\rho \ddot{\mathbf{u}} - \mathbf{b} + \int_{\mathcal{B}} \{\underline{\mathbf{T}}'\langle \mathbf{x} - \mathbf{x}' \rangle - \underline{\mathbf{T}}\langle \mathbf{x}' - \mathbf{x} \rangle\} dV_{\mathbf{x}'} = 0. \qquad (2.16)$$

In peridynamics, particles are assumed to be only interact with other particles in a small distance, which is described by a horizon $\mathcal{H}$. Let $\mathcal{H}_{\mathbf{x}}$ be the influence region of particle $\mathbf{x}$ and $\underline{\mathbf{T}}[\mathbf{x}]\langle \mathbf{x}' - \mathbf{x} \rangle = \mathbf{0}$ for any particle $\mathbf{x}'$ outside the horizon, i.e., $\mathbf{x}' \notin \mathcal{H}_{\mathbf{x}}$.

In a nutshell, the equation of motion for state-based peridynamics becomes

$$\rho\ddot{\mathbf{u}}(\mathbf{x},t) = \mathbf{L}(\mathbf{x},t) + \mathbf{b}(\mathbf{x},t),$$
$$\mathbf{L}(\mathbf{x},t) = \int_{\mathcal{H}_\mathbf{x}} \{\underline{\mathbf{T}}[\mathbf{x},t]\langle\mathbf{x}'-\mathbf{x}\rangle - \underline{\mathbf{T}}[\mathbf{x}',t]\langle\mathbf{x}-\mathbf{x}'\rangle\} dV_{\mathbf{x}'}, \tag{2.17}$$

where $\mathbf{L}(\mathbf{x},t)$ is a summation of the force per unit reference volume due to interaction with other particles. Compared with the classical equation of motion, no spatial derivatives appear in (2.17).

It is evident that the deformation vector state $\underline{\mathbf{Y}}$ represents a more general way of describing local body deformation compared to the classical deformation gradient tensor $\mathbf{F}$. Suppose there is a strain energy density function in the classical theory U such that

$$\underline{\mathbf{Y}}\langle\boldsymbol{\xi}\rangle = \mathbf{F}\boldsymbol{\xi} \quad \text{and} \quad W(\underline{\mathbf{Y}}) = U(\mathbf{F}), \tag{2.18}$$

the peridynamic constitutive model is then called correspondence to the classical constitutive model at $\mathbf{F}$.

A corresponding deformation gradient tenor, $\bar{\mathbf{F}}$ is derived using reduction defined in (2.4):

$$\bar{\mathbf{F}} = \mathcal{R}(\underline{\mathbf{Y}}) = \left(\int_{\mathcal{H}_\mathbf{x}} \omega(\underline{\mathbf{Y}} \otimes \boldsymbol{\xi}) dV_{\mathbf{x}'}\right)\mathbf{K}^{-1}, \tag{2.19}$$

where ω is the influence function defined at particle $\mathbf{x}$ in $\mathcal{H}_\mathbf{x}$, weighting the impact of each neighbor $\mathbf{x}'$ on the particle $\mathbf{x}$. It is selected as a spherical function based on the initial bond length, i.e., $\omega = \omega(|\boldsymbol{\xi}|)$. $\mathbf{K}$ is the symmetric shape tensor at particle $\mathbf{x}$, defined in (2.3):

$$\mathbf{K} = \int_{\mathcal{H}_\mathbf{x}} \omega(\boldsymbol{\xi} \otimes \boldsymbol{\xi}) dV_{\mathbf{x}'}. \tag{2.20}$$

In order to have an explicit formula of the force vector state $\underline{\mathbf{T}}$, it is more conve-

nient to define a peridynamic material model:

$$W(\underline{\mathbf{Y}}) = U(\bar{\mathbf{F}}(\underline{\mathbf{Y}})), \tag{2.21}$$

so that

$$\nabla W(\underline{\mathbf{Y}}) = \nabla U(\bar{\mathbf{F}}(\underline{\mathbf{Y}})) = \frac{\partial U}{\partial \bar{F}_{ij}} \nabla \bar{\mathbf{F}}(\underline{\mathbf{Y}}) = P_{ij} \nabla \bar{\mathbf{F}}(\underline{\mathbf{Y}}), \tag{2.22}$$

where P_{ij} is the component of the first Piola-Kirchhoff (PKI) stress $\mathbf{P}$, which is obtained from the approximate deformation gradient in (2.19) based on a classical constitutive model.

To find out the Frechet derivative $\bar{\mathbf{F}}(\underline{\mathbf{Y}})$, consider an incremental change in deformation vector state $\underline{\mathbf{Y}}$:

$$\begin{aligned}
\bar{F}_{ij}(\underline{\mathbf{Y}} + \Delta\underline{\mathbf{Y}}) &= \big(\int_{\mathcal{H}_{\mathbf{x}}} \omega(\underline{Y}_i + \Delta\underline{Y}_i)\xi_k dV_{\mathbf{x}'} \big) K^{-1}_{kj} \\
&= \bar{F}_{ij}(\underline{\mathbf{Y}}) + \int_{\mathcal{H}_{\mathbf{x}}} \omega \Delta\underline{Y}_i \xi_k K^{-1}_{kj} dV_{\mathbf{x}'} \\
&= \bar{F}_{ij}(\underline{\mathbf{Y}}) + \int_{\mathcal{H}_{\mathbf{x}}} \omega \delta_{il} \Delta\underline{Y}_l \xi_k K^{-1}_{kj} dV_{\mathbf{x}'} \\
&= \bar{F}_{ij}(\underline{\mathbf{Y}}) + (\omega \delta_{il} \xi_k K^{-1}_{kj}) \bullet \Delta\underline{Y}_l.
\end{aligned} \tag{2.23}$$

Therefore, based on the definition of Frechet derivatives in (2.8), the third-order tensor $\nabla \bar{\mathbf{F}}(\underline{\mathbf{Y}})$ can be expressed as

$$\nabla \bar{F}_{ijl}(\underline{\mathbf{Y}}) = \omega \delta_{il} \xi_k K^{-1}_{kj}. \tag{2.24}$$

Substitute (2.24) into (2.22):

$$\begin{aligned}\nabla W_l(\underline{\mathbf{Y}}) &= P_{ij}\omega\delta_{il}\xi_k K^{-1}_{kj} \\ &= \omega P_{lj}K^{-1}_{kj}\xi_k \\ &= \omega P_{lj}K^{-1}_{jk}\xi_k. \end{aligned} \tag{2.25}$$

The third step above considers that the shape tensor $\mathbf{K}$ is symmetric. Recalling the definition of expansion (2.1) and the peridynamic constitutive model (2.9), the vector state force $\underline{\mathbf{T}}$ is supposed to be

$$\underline{\mathbf{T}}\langle\boldsymbol{\xi}\rangle = \omega\underline{\mathcal{E}}(\mathbf{P}\mathbf{K}^{-1}) = \omega\mathbf{P}\mathbf{K}^{-1}\boldsymbol{\xi} \tag{2.26}$$

2.1.3 Conservation laws

The linear momentum balance is always satisfied for an arbitrary $\underline{\mathbf{T}}$ field due to Newton's third law. It can be demonstrated by integrating (2.17) over the body $\mathcal{B}$:

$$\begin{aligned}\int_{\mathcal{B}}(\rho\ddot{\mathbf{u}} - \mathbf{b})dV_{\mathbf{x}} &= \int_{\mathcal{B}}\int_{\mathcal{H}_{\mathbf{x}}}\{\underline{\mathbf{T}}\langle\mathbf{x}'-\mathbf{x}\rangle - \underline{\mathbf{T}}'\langle\mathbf{x}-\mathbf{x}'\rangle\}dV_{\mathbf{x}'}dV_{\mathbf{x}} \\ &= \int_{\mathcal{B}}\int_{\mathcal{B}}\{\underline{\mathbf{T}}\langle\mathbf{x}'-\mathbf{x}\rangle - \underline{\mathbf{T}}'\langle\mathbf{x}-\mathbf{x}'\rangle\}dV_{\mathbf{x}'}dV_{\mathbf{x}} \\ &= \mathbf{0}. \end{aligned} \tag{2.27}$$

This is because $\underline{\mathbf{T}}\langle\mathbf{x}'-\mathbf{x}\rangle = \mathbf{0}$ for particle $\mathbf{x}' \notin \mathcal{H}_{\mathbf{x}}$, and variables $\mathbf{x}$ and $\mathbf{x}'$ can be switched considering both integrations are over the whole body.

However, the balance of angular momentum may not be satisfied for a particular $\underline{\mathbf{T}}$. More precisely, if the force state $\underline{\mathbf{T}}\langle\boldsymbol{\xi}\rangle$ shares the same direction of $\boldsymbol{\xi}$, the material then automatically obeys the angular momentum balance and is called ordinary; otherwise, a restriction on $\underline{\mathbf{T}}$ is needed. Examples are shown in Fig. 2.2 to illustrate

the difference between peridynamic models.

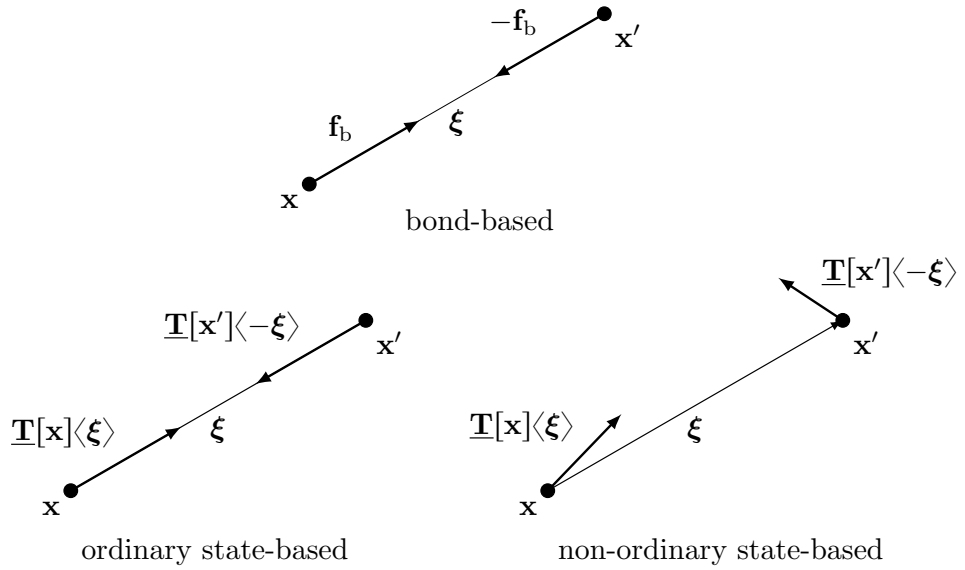

Figure 2.2: *Schematics of bond-based, ordinary state-based, and non-ordinary state-based material response.* $\mathbf{f}_{\mathrm{b}}$ *is a vector-valued function assumed interacting between each pair of particles in the bond-based peridynamic theory. All three responses satisfy the linear momentum balance due to Newton's third law; however, only the first two satisfy the angular momentum balance. A restriction on non-ordinary* $\underline{\mathbf{T}}$ *is needed to ensure the balance of angular momentum.*

Since (2.26) exhibits a non-ordinary force state field, it is necessary to demonstrate that the material body obeys the balance of angular momentum. Consider any deformation of body $\mathcal{B}$, the balance of angular momentum requires

$$\int_{\mathcal{B}} \mathbf{y}(\mathbf{x},t) \times \big(\rho\ddot{\mathbf{u}}(\mathbf{x},t) - \mathbf{b}(\mathbf{x},t)\big) dV_{\boldsymbol{\xi}} = 0 \quad \forall t \geq 0. \tag{2.28}$$

where $\mathbf{y}(\mathbf{x},t) = \mathbf{x} + \mathbf{u}(\mathbf{x},t)$ is the deformed bond, as shown in Fig. 2.1.

Substitute the peridynamic equation of motion (2.17) into (2.28):

$$\begin{aligned}
\int_{\mathcal{B}} \mathbf{y}\times(\rho\ddot{\mathbf{u}}-\mathbf{b})dV_{\boldsymbol{\xi}} &= \int_{\mathcal{B}} (\mathbf{x}+\mathbf{u})\times\int_{\mathcal{H}_{\mathbf{x}}} \{\underline{\mathbf{T}}\langle\mathbf{x}'-\mathbf{x}\rangle - \underline{\mathbf{T}}'\langle\mathbf{x}-\mathbf{x}'\rangle\}dV_{\mathbf{x}'}dV_{\mathbf{x}} \\
&= \int_{\mathcal{B}}\int_{\mathcal{B}} (\mathbf{x}+\mathbf{u})\times(\underline{\mathbf{T}}\langle\mathbf{x}'-\mathbf{x}\rangle - \underline{\mathbf{T}}'\langle\mathbf{x}-\mathbf{x}'\rangle)dV_{\mathbf{x}'}dV_{\mathbf{x}} \\
&= \int_{\mathcal{B}}\int_{\mathcal{B}} (\mathbf{x}+\mathbf{u})\times\underline{\mathbf{T}}\langle\mathbf{x}'-\mathbf{x}\rangle dV_{\mathbf{x}'}dV_{\mathbf{x}} \\
&\quad - \int_{\mathcal{B}}\int_{\mathcal{B}} (\mathbf{x}+\mathbf{u})\times\underline{\mathbf{T}}'\langle\mathbf{x}-\mathbf{x}'\rangle dV_{\mathbf{x}'}dV_{\mathbf{x}} \\
&= \int_{\mathcal{B}}\int_{\mathcal{B}} (\mathbf{x}+\mathbf{u})\times\underline{\mathbf{T}}\langle\mathbf{x}'-\mathbf{x}\rangle dV_{\mathbf{x}'}dV_{\mathbf{x}} \\
&\quad - \int_{\mathcal{B}}\int_{\mathcal{B}} (\mathbf{x}'+\mathbf{u}')\times\underline{\mathbf{T}}\langle\mathbf{x}'-\mathbf{x}\rangle dV_{\mathbf{x}'}dV_{\mathbf{x}} \\
&= -\int_{\mathcal{B}}\int_{\mathcal{B}} (\mathbf{x}'+\mathbf{u}'-\mathbf{x}-\mathbf{u})\times\underline{\mathbf{T}}\langle\mathbf{x}'-\mathbf{x}\rangle dV_{\mathbf{x}'}dV_{\mathbf{x}} \\
&= -\int_{\mathcal{B}}\int_{\mathcal{B}} \underline{\mathbf{Y}}\langle\mathbf{x}'-\mathbf{x}\rangle\times\underline{\mathbf{T}}\langle\mathbf{x}'-\mathbf{x}\rangle dV_{\mathbf{x}'}dV_{\mathbf{x}} \\
&= -\int_{\mathcal{B}}\int_{\mathcal{H}_{\mathbf{x}}} \underline{\mathbf{Y}}\langle\boldsymbol{\xi}\rangle\times\underline{\mathbf{T}}\langle\boldsymbol{\xi}\rangle dV_{\boldsymbol{\xi}}dV_{\mathbf{x}}. \qquad (2.29)
\end{aligned}$$

Variables $\mathbf{x}$ and $\mathbf{x}'$ are switched in the fourth step above. Hence, the equivalent form of the angular momentum balance in the state-based peridynamics is

$$\int_{\mathcal{H}_{\mathbf{x}}} \underline{\mathbf{Y}}\langle\boldsymbol{\xi}\rangle\times\underline{\mathbf{T}}\langle\boldsymbol{\xi}\rangle dV_{\boldsymbol{\xi}} = 0 \quad \forall\underline{\mathbf{Y}}. \qquad (2.30)$$

Substitute the non-ordinary force state vector $\underline{\mathbf{T}}$ in (2.26) into (2.30):

$$\begin{aligned}\left(\int_{\mathcal{H}_{\mathbf{x}}} \underline{\mathbf{Y}}\langle\boldsymbol{\xi}\rangle \times \underline{\mathbf{T}}\langle\boldsymbol{\xi}\rangle dV_{\boldsymbol{\xi}}\right)_i &= \epsilon_{ijk}\int_{\mathcal{H}_{\mathbf{x}}} \underline{y}_j\langle\boldsymbol{\xi}\rangle\big(\omega P_{kl}K^{-1}_{lm}\xi_m\big)dV_{\boldsymbol{\xi}} \\ &= \epsilon_{ijk}P_{kl}K^{-1}_{lm}\int_{\mathcal{H}_{\mathbf{x}}} \omega\underline{y}_j\langle\boldsymbol{\xi}\rangle\xi_m dV_{\boldsymbol{\xi}} \\ &= \epsilon_{ijk}P_{kl}K^{-1}_{lm}F_{jn}K_{nm} \\ &= \epsilon_{ijk}P_{kl}F_{jn}\delta_{nl} \\ &= \epsilon_{ijk}P_{kl}F_{jl}, \end{aligned} \tag{2.31}$$

where ϵ_{ijk} denotes the alternator tensor components. Recall the relation between PKI stress $\mathbf{P}$ and Cauchy stress tensor $\boldsymbol{\sigma}$:

$$\mathbf{P}\mathbf{F}^{\mathrm{T}} = \det(\mathbf{F})\boldsymbol{\sigma}. \tag{2.32}$$

Equation (2.31) then becomes:

$$\left(\int_{\mathcal{H}_{\mathbf{x}}} \underline{\mathbf{Y}}\langle\boldsymbol{\xi}\rangle \times \underline{\mathbf{T}}\langle\boldsymbol{\xi}\rangle dV_{\boldsymbol{\xi}}\right)_i = \det(\mathbf{F})\epsilon_{ijk}\sigma_{kj} = 0, \tag{2.33}$$

due to the symmetry of $\boldsymbol{\sigma}$. Thus, the non-ordinary force state $\underline{\mathbf{T}}$ obtained from (2.26) obeys the angular momentum balance.

Above is a short review of non-ordinary state-based peridynamics. More details can be seen in Silling's paper [10]. All peridynamic models used in the later chapters, shortened as PD models, are based on the non-ordinary state-based peridynamic theory elaborated in this chapter, if no specific comment is made.

2.2 Adaptive Dynamic Relaxation Solver (ADRS)

Since there is no large-matrix operation in the explicit method (e.g., computing the tangent modulus $\partial \mathbf{P}/\partial \mathbf{F}$), less computation cost compared to implicit solvers (described later) is foreseeable. In this paper, an explicit dynamic relaxation method with the quasi-static assumption is adopted, in which every time steps are selected carefully.

In dynamic methods, a nonlinear problem can be solved through artificial damping leading to a stable solution after a large number of iterations. With the body force ignored, the equation of motion (2.17) can be rewritten in a vector form as

$$\ddot{\mathbf{u}}(\mathbf{x}, t) + c\dot{\mathbf{u}}(\mathbf{x}, t) = \mathbf{f}(\mathbf{u}, \mathbf{x}, t), \tag{2.34}$$

where c is the damping ratio coefficient and the force vector $\mathbf{f}$ on the right side is defined as $\mathbf{f}(\mathbf{u}, \mathbf{x}, t) = \mathbf{\Lambda}^{-1}\mathbf{L}(\mathbf{x}, t)$, in which $\mathbf{\Lambda}$ is the fictitious diagonal density matrix. Based on the adaptive dynamic relaxation method, the most desired diagonal density matrix and damping coefficient can be determined by Greschgorin's theorem and Rayleigh's quotient, respectively [99].

Let $\mathbf{u}^n$, $\dot{\mathbf{u}}^n$, $\ddot{\mathbf{u}}^n$, and $\mathbf{f}^n$ denote the displacement, velocity, acceleration, and force vector field at $t = n$, respectively, and Δt be the time step size assumed constant. In the central difference scheme, the velocity and acceleration vectors are approximated as

$$\dot{\mathbf{u}}^n \approx \frac{1}{2\Delta t}(\mathbf{u}^{n+1} - \mathbf{u}^{n-1}), \tag{2.35}$$

$$\ddot{\mathbf{u}}^n \approx \frac{1}{\Delta t^2}(\mathbf{u}^{n+1} - 2\mathbf{u}^n + \mathbf{u}^{n-1}). \tag{2.36}$$

Then, substitute (2.35) and (2.36) into (2.34), and rearrange terms for $\mathbf{u}^{n+1}$:

$$\mathbf{u}^{n+1} = \left[2\Delta t^2 \mathbf{f}^n + 4\mathbf{u}^n + (c\Delta t - 2)\mathbf{u}^{n-1}\right]/(2 + c\Delta t) \tag{2.37}$$

which is the update scheme for the displacement field. Equation (2.38) is employed to approximate $\mathbf{u}^{-1}$ to initialize the displacement iteration:

$$\mathbf{u}^{-1} = \mathbf{u}^0 - \Delta t \dot{\mathbf{u}}^0 + \frac{\Delta t^2}{2}\ddot{\mathbf{u}}^0, \tag{2.38}$$

where $\mathbf{u}^0$, $\dot{\mathbf{u}}^0$, and $\ddot{\mathbf{u}}^0$ are the initial displacement, velocity, and acceleration vector, respectively. The velocity and acceleration vectors can be updated afterwards by (2.35) and (2.36), though not necessary.

With the assumption of a unit diagonal matrix $\mathbf{\Lambda}$, the time step size needs to be selected based on Greschgorin's theorem [99], which can be written as

$$\Delta t \leq \sqrt{4\Lambda_{ii} / \sum\nolimits_j |K_{ij}|}, \tag{2.39}$$

where Λ_{ii} is the diagonal coefficients of the density matrix and K_{ij} is the stiffness matrix of the equation system. Since this stiffness matrix K_{ij} is not explicitly obtained in computing the force vector $\mathbf{f}$ (see (2.17) and (2.34)), another approximation scheme is applied for the time step size.

An appropriate time step Δt for the 1D peridynamic model is based on the wave speed c_s using the Courant–Friedrichs–Lewy (CFL) condition [100]:

$$\Delta t \leq 2\Delta x / c_\mathrm{s}, \tag{2.40}$$

where Δx is the minimal grid size, or the minimal bond length in peridynamics. A detailed derivation of the time step size from a 1D elastic problem is described in

Appendix B.

In higher-dimensional cases, the CFL condition is more stringent. Assuming that we are dealing with n–dimensional problems using a uniform grid and the wave speeds along different directions are the same, the critical time step size becomes

$$\Delta t \leq \frac{2}{n}\Delta x \cdot \sqrt{\rho / E_{max}}, \tag{2.41}$$

in which ρ is the density and E_{max} is the maximum component of the elastic stiffness matrix is used to approximate the maximum possible wave speed. Note that the CFL limit condition in (2.41) could be quite conservative since the derivation is based on just the closest neighbors [101].

The damping ratio c is then selected carefully by the lowest frequency of the system using Rayleigh's quotient [99]:

$$c^n = 2\sqrt{\frac{(\mathbf{u}^n)^{\mathrm{T}}\mathbf{k}^n\mathbf{u}^n}{(\mathbf{u}^n)^{\mathrm{T}}\mathbf{u}^n}}, \tag{2.42}$$

where $\mathbf{k}^n$ is the diagonal local stiffness matrix, which is given as

$$k_{ii}^n = -(f_i^n/\Lambda_{ii} - f_i^{n-1}/\Lambda_{ii})/(u_i^n - u_i^{n-1}), \tag{2.43}$$

where f_i^n is the ith component of the force vector $\mathbf{f}$ at time $t = n$ and Λ_{ii} is set to be 1. Since the local stiffness matrix calculation involves division by the difference between current and old displacement components, it is highly possible to encounter a zero-component in the displacement field where the criteria fails [99]. Therefore, the local stiffness k_{ii}^n is set to be zero when the difference between displacement fields vanishes. Finally, an initial guess of damping ratio c_0 is given to start computation.

2.3 Numerical Discretization and Algorithm

Assume there are N neighbor particles of material point $\mathbf{x}$, then (2.17) can be discretized as (neglecting the body force $\mathbf{b}$ and only considering properties at current time t):

$$\mathbf{L}(\mathbf{x}) = \sum_{i=1}^{N} \{\underline{\mathbf{T}}[\mathbf{x}]\langle \mathbf{x}'_i - \mathbf{x}\rangle - \underline{\mathbf{T}}[\mathbf{x}'_i]\langle \mathbf{x} - \mathbf{x}'_i\rangle\} V_{\mathbf{x}'_i} = \mathbf{0}, \tag{2.44}$$

where $\mathbf{x}'_i$ is the ith particle in $\mathbf{x}$'s horizon and its corresponding volume is $V_{\mathbf{x}'_i}$.

Next, the deformation gradient $\mathbf{F}(\mathbf{x})$ and shape tensor $\mathbf{K}(\mathbf{x})$ at particle $\mathbf{x}$ are discretized as the following:

$$\begin{aligned} \mathbf{F}(\mathbf{x}) &= \Big[\sum_{i=1}^{N} \omega(\mathbf{y}'_i - \mathbf{y}) \otimes (\mathbf{x}'_i - \mathbf{x}) V_{\mathbf{x}'_i}\Big] \mathbf{K}(\mathbf{x})^{-1}, \\ \mathbf{K}(\mathbf{x}) &= \sum_{i=1}^{N} \omega(\mathbf{x}'_i - \mathbf{x}) \otimes (\mathbf{x}'_i - \mathbf{x}) V_{\mathbf{x}'_i}, \end{aligned} \tag{2.45}$$

where $\mathbf{y}'$ and $\mathbf{y}$ are the images of $\mathbf{x}'$ and $\mathbf{x}$, respectively. Given the constitutive model, represented by an operator $\mathcal{F}$, the force state $\underline{\mathbf{T}}[\mathbf{x}]\langle \mathbf{x}'_i - \mathbf{x}\rangle$ at particle $\mathbf{x}$ can be obtained from

$$\underline{\mathbf{T}}[\mathbf{x}]\langle \mathbf{x}'_i - \mathbf{x}\rangle = \omega \mathcal{F}\big(\mathbf{F}(\mathbf{x})\big) \mathbf{K}(\mathbf{x})^{-1} (\mathbf{x}'_i - \mathbf{x}). \tag{2.46}$$

As for the rest half terms in (2.44), $\underline{\mathbf{T}}[\mathbf{x}'_i]\langle \mathbf{x} - \mathbf{x}'_i\rangle$ can be found in a similar way, which is

$$\underline{\mathbf{T}}[\mathbf{x}'_i]\langle \mathbf{x} - \mathbf{x}'_i\rangle = \omega \mathcal{F}\big(\mathbf{F}(\mathbf{x}'_i)\big) \mathbf{K}(\mathbf{x}'_i)^{-1} (\mathbf{x} - \mathbf{x}'_i). \tag{2.47}$$

However, in order to acquire $\mathbf{F}(\mathbf{x}'_i)$ and $\mathbf{K}(\mathbf{x}'_i)$ at particle $\mathbf{x}'_i$, information about the ith particle's horizon needs to be known. Fig. 2.3 is an illustration of interactions of one particle with its nearest neighbors.

With all force vector states obtained, the adaptive dynamic relaxation method, elaborated in Section 2.2, is applied to solve the equation $\mathbf{L}(\mathbf{x}) = \mathbf{0}$. For a 2D

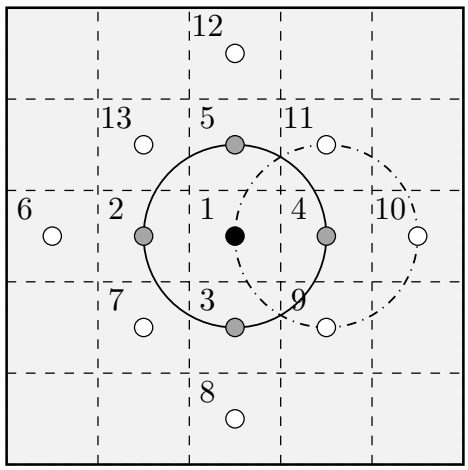

Figure 2.3: *Particle interactions with closest neighbors in the PD model. Particles i = 2, 3, 4, 5 are nearest neighbors of the particle 1 (denoted as $\mathbf{x}$); particles i = 1, 9, 10, 11 are nearest neighbors of the particle 4 (denoted as $\mathbf{x}'_i$). In this case, all 13 particles shown above should be included in order to obtain $\mathbf{L}(\mathbf{x})$ at particle $\mathbf{x}$ in* (2.44).

problem, the global equation of motion can be organized as a vector system with a size of $2 \times N_{\text{total}}$, where N_{total} is the total number of particles in the simulation. Since $\mathbf{L}(\mathbf{x})$ is completely dependent on the current field, the system can be explicitly started with initial guesses of displacement, velocity, and acceleration fields.

During dynamic iterations in one loading step, two absolute errors ε_1 and ε_2 are calculated at each iteration step with the definitions as

$$\varepsilon_1 = \frac{\|\mathbf{L}(\mathbf{x})\|_2}{N} \text{ and } \varepsilon_2 = \frac{\|\delta\mathbf{u}\|_2}{N}, \tag{2.48}$$

where l^2-norm is employed and N is the total number of particles. The first error ε_1 describes the degree to which the vector system approaches to zero while the second one ε_2 denotes the magnitude of displacement increments between two adjacent iteration steps. In order to normalize the error from initial guesses, two corresponding relative errors e_1 and e_2 are then computed and monitored, which are

$$e_1 = \frac{\varepsilon_1}{\varepsilon_1^0} \text{ and } e_2 = \frac{\varepsilon_2}{\varepsilon_2^0}, \tag{2.49}$$

where ε^0 is the initial absolute error in each loading step. Iterations stop only when both criteria, $e_{1,2} < e_l$, are satisfied, where $e_l = 10^{-6}$. All quantities are then updated into the next loading step.

To improve the computation performance, parallel libraries, OpenMP and Open MPI, are adopted in the codes. Given that kinematic properties, such as the displacement $\mathbf{u}$ and deformation gradient $\mathbf{F}$, are known before hand due to the explicit method, the constitutive model can be applied on different particles in parallel. In other words, the computation involved in acquiring $\mathbf{P}(\mathbf{x}) = \mathcal{F}\big(\mathbf{P}(\mathbf{x})\big)$ at particle $\mathbf{x}$ and $\mathbf{P}(\mathbf{x}') = \mathcal{F}\big(\mathbf{P}(\mathbf{x}')\big)$ at particle $\mathbf{x}'$ are completely independent. The computation domain is therefore partitioned into several groups with each group calculating its own stress tensor. Finally, all information is gathered in the assembly of the vector system $\mathbf{L}(\mathbf{x})$.

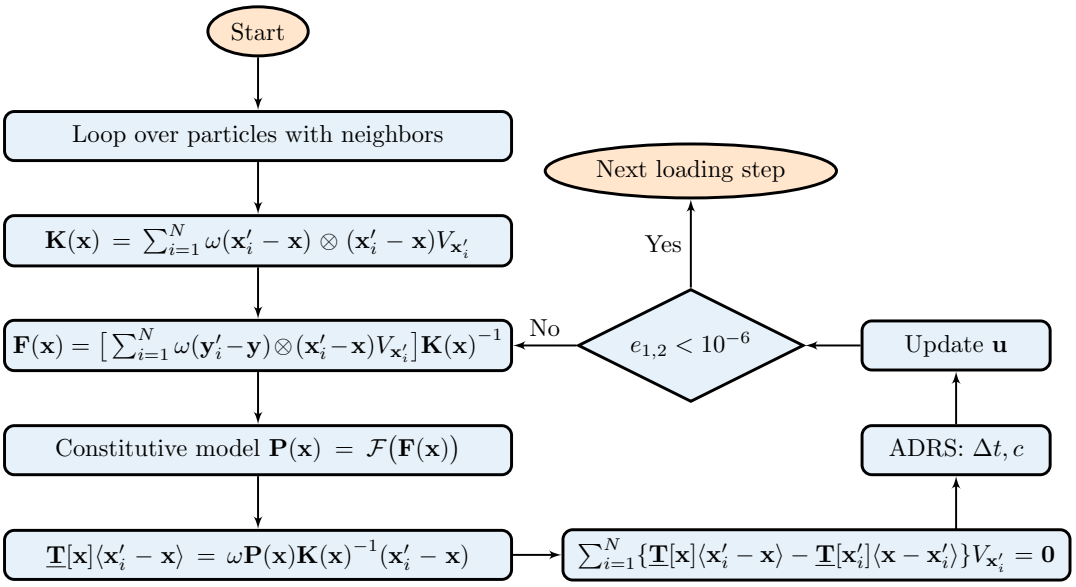

Figure 2.4: *PD-ADRS flowchart.*

Important computational steps of the PD-ADRS algorithm are summarized in the flowchart shown in Fig.2.4. Compared to implicit solvers, there is no matrix-inversion operation in explicit methods. Besides, this new adaptive dynamic relaxation method allows flexibility in applying different constitutive models and extending to 3D cases.

Next section will briefly explain the quasi-static implicit iterative scheme by Sun and Sundararaghavan [21].

2.4 Implicit Algorithm

The Newton Raphson iterative scheme is employed to solve the equation of motion (2.17). Take the derivative of the particle displacement vector $\mathbf{u}$:

$$\frac{\partial \mathbf{L}}{\partial \mathbf{u}} \delta \mathbf{u} = -\mathbf{L}(\mathbf{x}), \tag{2.50}$$

where $\delta \mathbf{u}$ is the increment of the particle displacement. With the same numerical discretization in Section 2.3, the Jacobian matrix $\frac{\partial \mathbf{L}}{\partial \mathbf{u}}$ can be then expressed as

$$\frac{\partial \mathbf{L}}{\partial \mathbf{u}} = \sum_{i=1}^{N} \big(\frac{\partial \underline{\mathbf{T}}[\mathbf{x}] \langle \mathbf{x}'_i - \mathbf{x} \rangle}{\partial \mathbf{u}} - \frac{\partial \underline{\mathbf{T}}[\mathbf{x}'_i] \langle \mathbf{x} - \mathbf{x}'_i \rangle}{\partial \mathbf{u}} \big) V_{\mathbf{x}'_i} = \mathbf{0}, \tag{2.51}$$

where $\mathbf{x}'_i$ is the ith particle in $\mathbf{x}$'s horizon and its corresponding volume is $V_{\mathbf{x}'_i}$. With the tangent modulus $\frac{\partial \mathbf{P}}{\partial \mathbf{F}}$ obtained from the constitutive model (e.g., crystal plasticity), the derivative of the force state $\underline{\mathbf{T}}[\mathbf{x}] \langle \mathbf{x}'_i - \mathbf{x} \rangle$ can be written using (2.26) as:

$$\frac{\partial \underline{\mathbf{T}}[\mathbf{x}] \langle \mathbf{x}'_i - \mathbf{x} \rangle}{\partial \mathbf{u}} = \frac{\partial \underline{\mathbf{T}}[\mathbf{x}] \langle \mathbf{x}'_i - \mathbf{x} \rangle}{\partial \mathbf{F}} \frac{\partial \mathbf{F}}{\partial \mathbf{u}} = \omega \frac{\partial \mathbf{P}}{\partial \mathbf{F}} \frac{\partial \mathbf{F}}{\partial \mathbf{u}} \mathbf{K}^{-1} (\mathbf{x}'_i - \mathbf{x}). \tag{2.52}$$

As the discrete deformation gradient $\mathbf{F}$ is given by (2.45), the final expression of the Jacobian matrix becomes

$$\begin{aligned} \frac{\partial \mathbf{L}}{\partial \mathbf{u}} = \sum_{i=1}^{N} \omega_i \frac{\partial \mathbf{P}}{\partial \mathbf{F}} \Big(- \sum_{j=1}^{N} \omega_j \mathbf{I} \otimes (\mathbf{x}'_j - \mathbf{x}) \mathbf{K}^{-1} V_{\mathbf{x}'_j} \Big) \mathbf{K}^{-1} (\mathbf{x}'_i - \mathbf{x}) V_{\mathbf{x}'_j} \\ - \sum_{i=1}^{N} \omega'_i \frac{\partial \mathbf{P}'}{\partial \mathbf{F}'} \Big(\omega'_i \mathbf{I} \otimes (\mathbf{x} - \mathbf{x}'_i) \mathbf{K}'^{-1} V_{\mathbf{x}} \Big) \mathbf{K}'^{-1} (\mathbf{x} - \mathbf{x}'_i) V_{\mathbf{x}'_i}. \end{aligned} \tag{2.53}$$

The following notation is used in the above equation:

1. $\mathbf{x}'_i$ is the i^{th} neighbor particle of $\mathbf{x}$

2. ω_i is the influence function value at $\mathbf{x}$ for the bond $(\mathbf{x}'_i - \mathbf{x})$ while ω'_i is at $\mathbf{x}'_i$ for the bond $(\mathbf{x} - \mathbf{x}'_i)$

3. N,$\mathbf{K}$, and $\frac{\partial \mathbf{P}}{\partial \mathbf{F}}$ are the number of neighboring particles, shape tensor, and tangent moduli of the particle $\mathbf{x}$, respectively; N',$\mathbf{K}'$,$\frac{\partial \mathbf{P}'}{\partial \mathbf{F}'}$ are the corresponding quantities of the particle $\mathbf{x}'_i$

The system of equations above can be solved iteratively until $||\delta \mathbf{u}|| < \epsilon_{\text{i}}$, where ϵ_{i} is the residual error limit. The sparseness of the Jacobian matrix in (2.53) depends on the radius of influence δ, and varies from sparsely populated for a small horizon size that only includes nearest neighbor interactions to a fully populated matrix for a large horizon size (a highly non–local system). The advantage of the implicit method explained here is that larger time steps can be used compared to the explicit method, however, each time step involves iterations based on solution of large systems of equations and it is necessary to compute the tangent modulus $\frac{\partial \mathbf{P}}{\partial \mathbf{F}}$ at the constitutive level for building such a system. Therefore, the explicit method explained previously avoids the need to build systems of equations and simplifies the constitutive model implementation.

2.5 Numerical Tests with Nearest-Neighbor Discretizations

Two numerical examples are presented in this section. The first 1D example is solved by hand to show some important properties in peridynamics, while the second 3D example verifies the PD-ADRS model. Both examples are based on meshless discretizations in which the PD horizon only consists of nearest neighbors. For one thing, smaller horizon size means less particle neighbors. When we solve the 1D example by hand, only the nearest left and right particles should be considered in the calculation. For another, larger horizons will bring a serious numerical stability

issue, i.e., zero-energy modes, and irregular or ill-posed defect horizons at boundary. Typically, the peridynamic family with nearest neighbors are the most stable and accurate compared to larger horizon sizes [87, 93]. It is one type of convergence defined in peridynamics that results are converging as the horizon size decreases on a fixed discretization [98].

2.5.1 A simple 1D elastic bar

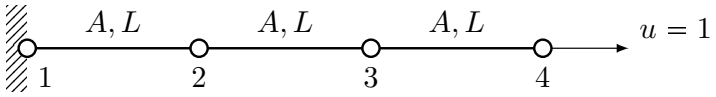

Figure 2.5: *A 1D elastic bar with a constant cross-sectional area A and a total length 3L is discretized into 4 particles. The Young's modulus is a constant E through the bar. Displacement boundary condition u = 1 is applied on particle 4 while particle 1 is fixed on the wall.*

Consider an elastic bar is fixed to its left and stretched by a displacement boundary condition $u = 1$ to its right, as shown in Fig. 2.5. The bar is then discretized into 4 particles and each particle owns a constant volume $V = AL$.

Let u_i, F_i, σ_i, and K_i be the 1D displacement, deformation gradient, stress, and shape tensor of particle i, respectively, where i is from 1 to 4. As the bar is assumed in elastic, the analytical solution for the displacement field should be linear, i.e., $u_i = (i-1)/3$. Furthermore, both strain and stress fields are constant.

Assume the horizon radius is L, i.e., particles only interact with nearest ones, and the influence factor $\omega = 1$, then substitute (2.46) and (2.47) into (2.44), we get the

governing equation at particle 2:

$$\begin{aligned}(-\sigma_1 K_1^{-1} L - \sigma_2 K_2^{-1} L)V + (\sigma_2 K_2^{-1} L + \sigma_3 K_3^{-1} L)V = 0 \\ \Longrightarrow \sigma_3 K_3^{-1} - \sigma_1 K_1^{-1} = 0 \\ \Longrightarrow K_1 = K_3, \end{aligned} \tag{2.54}$$

where $\sigma_1 = \sigma_3$ due to a constant stress field. Equation (2.54) shows that the shape tensor $\mathbf{K}$ is supposed to be constant in the material model with a fixed horizon size. Generally, a constant shape tensor is preferred in PD simulations due to its simplicity and precise physical meaning.

Similar to other meshfree numerical methods, the enforcement of kinematic constraints cannot follow the standard way as in the continuum mechanics. This is because the equation of motion (2.17) and deformation gradient (2.19) are expressed in integral forms. Hence, special numerical techniques are needed to deal with this issue, such as introducing shadow particles [99] or modifying the influence function at boundary [89].

For the nearest neighbor interactions, one can decide to calculate the shape tensor and deformation gradient at boundary with defective horizons, while holding a constant shape tensor based on an intact horizon for calculating force state vectors in (2.26).

The 1D elastic bar example is reconsidered to illustrate our boundary treatment. It is apparent that horizons of boundary particles 1 and 4 are defective or half-missing compared to horizons of inner particles 2 and 3 which are intact and complete. The shape tensors of particle 1 and 4 are computed with defective horizons as $K_1 = K_4 = AL^3$, while $K_2 = K_3 = 2AL^3$ for particle 2 and 3 based on intact horizons. Similar

to the treatment on shape tensors, the deformation gradients are then calculated as

$$\begin{aligned} F_1 &= [(u_2 - u_1) + L]AL^2/K_1 = (u_2 - u_1)/L + 1, \\ F_2 &= [-(u_1 - u_2 - L) + (u_3 - u_2 + L)]AL^2/K_2 = (u_3 - u_1)/2L + 1, \\ F_3 &= [-(u_2 - u_3 - L) + (u_4 - u_3 + L)]AL^2/K_3 = (u_4 - u_2)/2L + 1, \\ F_4 &= [-(u_3 - u_4) + L]AL^2/K_4 = (u_4 - u_3)/L + 1, \end{aligned} \tag{2.55}$$

where F_1 and F_4 are approximated by the displacements of two particles inside the boundary, F_2 and F_3 are by displacements of particles on the two sides. Take a linearly-distributed displacement field as a quick check, constant deformation gradients will be obtained by (2.55): $F_1 = F_2 = F_3 = F_4$, which is correct. This demonstrates that the boundary treatment is effective.

With regard to force vector states in the equation of motion (2.44), a constant shape tensor is used instead based on (2.54). We arbitrarily choose a shape tensor computed at inner particles with an intact horizon.

Same boundary treatment will be applied on the next 3D example to verify the PD-ADRS model.

2.5.2 Mesh convergence tests on a 3D elastic brick

A 3D elastic brick numerical example is considered in this section. The length-width-height ratio of the brick is $2L : 2L : L$, where L is set to be 1 for convenience. Displacements at its four sides are restricted, as shown in Fig. 2.6(a), while the top and bottom faces are left traction-free. The material is assumed isotropic with Young's modulus $E = 1000$, Poisson's ratio $\nu = 0.3$, and mass density $\rho = 1$.

The PD-ADRS model is applied on a simple 18-particles mesh in Fig. 2.6(b) to begin with. During iterations, the z-displacement w_c of the bottom center (particle 2 in Fig. 2.6(b) and two relative errors $e_{1,2}$, defined in (2.49), are monitored and plotted

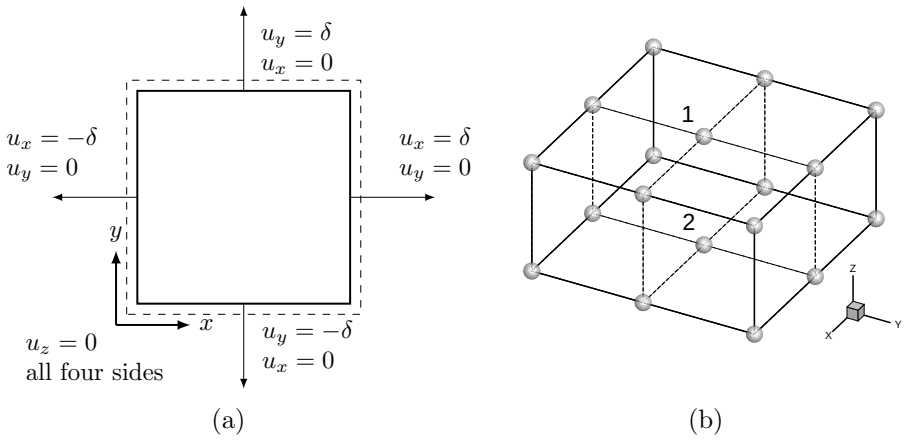

(a) (b)

Figure 2.6: *A 3D elastic brick example. (a) is an illustration of boundary conditions from the view of z direction. Displacement boundary conditions are applied on four sides while the top and bottom are left traction-free.* $\delta = 0.01$ *is a small increment. (b) is a simple mesh with 18 PD particles, where particle 1 is at the top center and 2 at the bottom center.*

in Fig. 2.7.

Based on the PD theory, the exact numerical solutions for particles 1 and 2 in Fig. 2.6(b) are

$$u_1 = u_2 = 0,\ v_1 = v_2 = 0,\ w_1 = -w_2 = -\frac{0.02\nu}{3-\nu}, \tag{2.56}$$

where u, v, and w are displacement components in x, y, and z direction, respectively, and ν is the Poisson's ratio.

Simulation results are shown in Fig. 2.7. Numerical solution w_c is exponentially converging to the exact $w = 1/300$ given that $\nu = 0.3$; in the meantime, two relative errors decrease linearly in the log-plot, though, with oscillations due to the explicit center-difference scheme. Note that both criteria $e_1 < 10^{-6}$ and $e_2 < 10^{-6}$ are satisfied.

Subsequently, a mesh convergence test is conducted on the 3D elastic brick with critical parameters listed in Table. 2.1. Take the case with a mesh size 8:8:4 for example: three numbers 8, 8, and 4 represent the number of particles in the x, y,

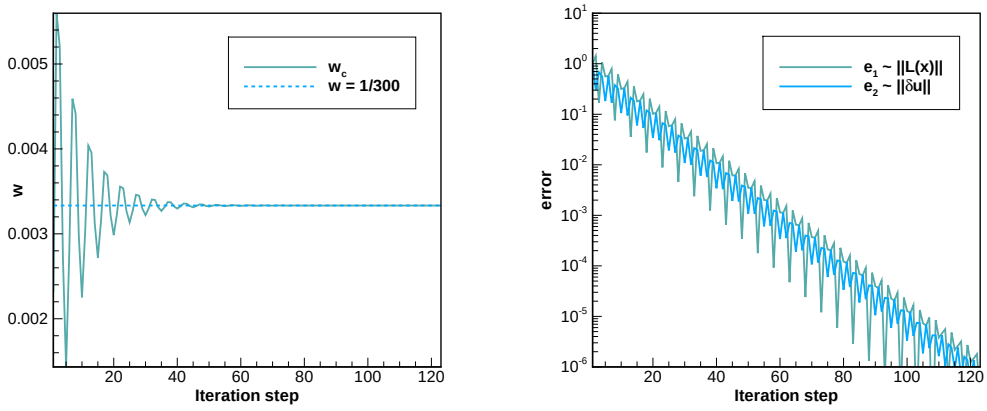

(a) (b)

Figure 2.7: *Convergence plots of a 3D elastic brick with 18 particles. The z-displacement w_c of the bottom center (particle 2) is monitored in (a) and two relative errors are in (b).*

and z direction, respectively; w_c is the numerical convergent z-displacement of the bottom center of PD results; error is the relative error between w_c and w^*, which is $|(w_c - w^*)/w^*|$, where w^* is the z-displacement of the bottom center of ANSYS simulations with a mesh size of 32:32:16; Δt_c is the critical time step computed by (2.41); Δt is the time step employed in the PD-ADRS model; finally, c^0 is the initial damping ratio to start the iteration.

Table 2.1: *Mesh convergence parameters: mesh size, numerical convergent z-displacement at the bottom center of PD results, relative error between w_c and w^*, critical time step, time step selected in PD simulations, and initial damping ratio.*

Mesh size	$w_c \times 10^3$	**error**[1]	Δt_c	Δt	c^0
2:2:1	3.333	19.0%	0.0316	0.02	100
4:4:2	2.636	36.0%	0.0158	0.01	100
8:8:4	3.666	10.9%	0.0079	0.005	100
16:16:8	4.009	2.6%	0.0040	0.003	100
32:32:16	4.076	1.0%	0.0020	0.001	200

[1] **error** $= |(w_c - w^*)/w^*|$, where $w^* = 4.116 \times 10^{-3}$

We applied a standard quasi-static FEM formulation with 8 noded hexahedral

elemetns in the 3D problem. The column of error indicates that PD results are approaching to ANSYS results as mesh is refined. In PD simulations with a mesh size of 32:32:16, the damping ratio and two relative errors are monitored and shown in Fig. 2.8(a) and 2.8(b), respectively. A comparative test with a constant damping ratio $c = 200$ is carried out. The adaptive dynamic method is proven to be stable and converging faster.

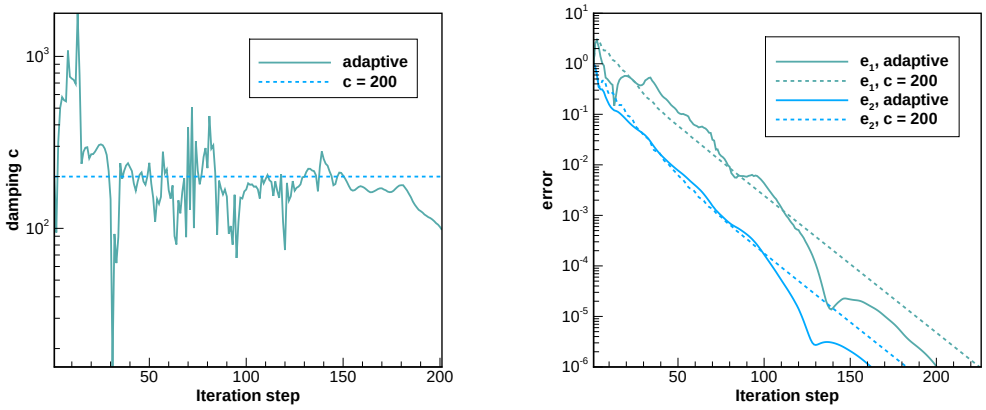

(a) (b)

Figure 2.8: *Convergence plots of the PD-ADRS model with a mesh size of 32:32:16. The damping ratio and two relative errors are monitored in (a) and (b), respectively. A comparative test with a constant damping ratio* $c = 200$ *is plotted in dashed lines while the adaptive relaxation method is in solid lines.*

Eventually, results are compared between the PD-ADRS model and ANSYS with a mesh size of 32:32:16, in which peridynamic particles are located at element nodes. Contours of z-displacement on the bottom face based on these two methods are plotted in Fig. 2.9. The overall contours are similar while disagreements exist. For example, there is no peak value at four corners in the PD model. This is mainly because peridynamics is based on a non-local integral formulation where singularities and discontinuities can be captured with appropriate approximations. In continuum mechanics, the singularity at conner point is a consequence of the failure of Cauchy

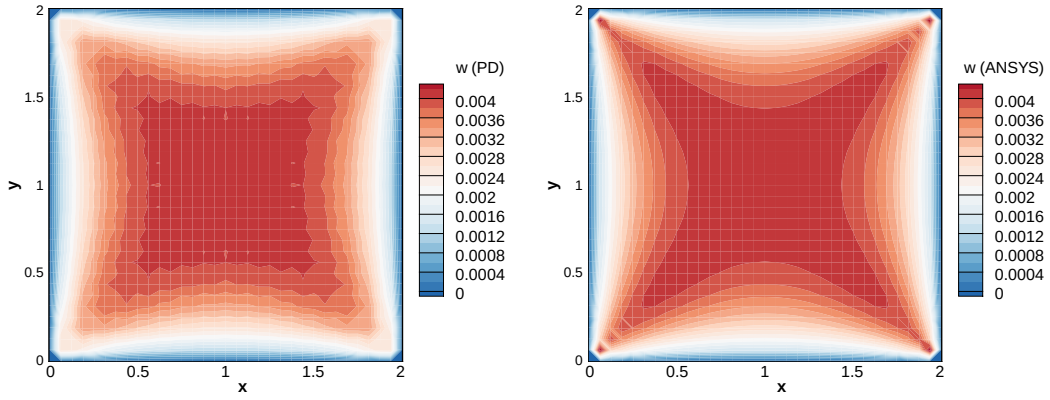

(a) (b)

Figure 2.9: *Contours of z-displacement on the bottom face obtained from (a) the dynamic PD model and (b) ANSYS.*

(stress-traction) relation due to lack of definition of the normal vector at corner.

To have a closer look at what happens around corners, different cross sections are selected at $x = 1/16$, $x = 1/2$, and $x = 1$, shown in Fig. 2.10(a), and z-displacements on the bottom face are plotted in Figs. 2.10(b), (c), and (d) for each section. The singularities of ANSYS at corners are obvious with abrupt jumps in Fig. 2.10(b). As traveling from side to middle, the differences between two models become smaller. Few disagreements can be found in Fig. 2.10(d).

However, oscillations in PD results are conspicuous. Compared to smooth results in ANSYS, PD simulations are serrated, which is attributed to zero-energy modes, or essentially, weak connections between PD particles. This intrinsic stability issue of peridynamics has been discussed by other researchers [99] and theoretically demonstrated in Silling's paper [102]. Nevertheless, no satisfactory solution has been achieved.

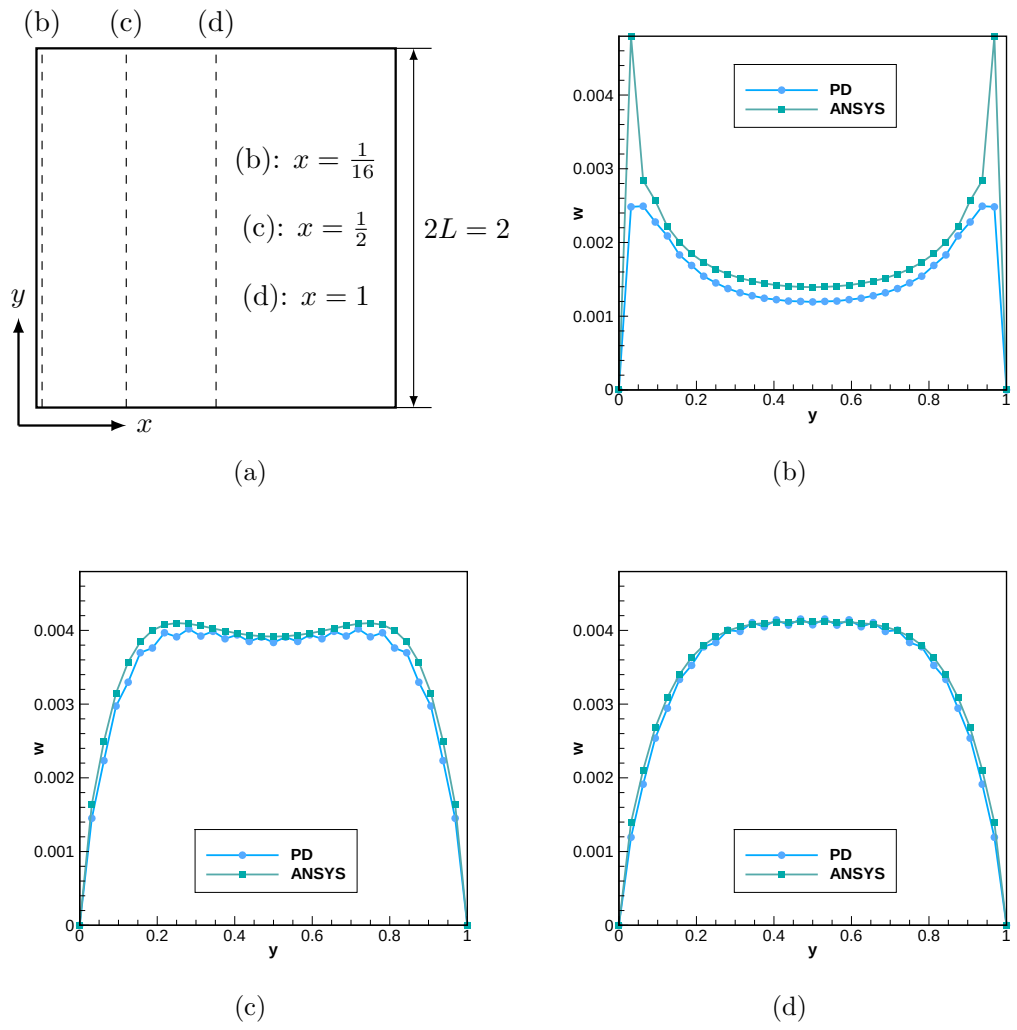

Figure 2.10: *The geometry of the 3D brick from the view of z direction is shown in (a) and z-displacement contours on the bottom of three cross sections obtained from the PD model (blue lines) and ANSYS (green lines) are plotted in (b) at* $x = 1/16$*, (c) at* $x = 1/2$*, and (d) at* $x = 1$*.*

2.6 Conclusions

A new PD-ADRS model is proposed and demonstrated stable and efficient in elastic problems consisting of nearest-neighboring peridynamic family. In the next chapter, this numerical model will be implemented with crystal plasticity in planar polycrystals.

CHAPTER III

2D PD-ADRS Implementation with Crystal Plasticity

As discussed in the Introduction, it becomes difficult for CPFE models to properly predict mechanical properties in regions with discontinuities or strong strain gradients such as plastic strain localization zones. Furthermore, the size of shear bands and magnitude of quantities computed by the standard FEM are highly determined by the element size [21, 103]. Therefore, improvements have been continuously made on CPFE models to address the issue of mesh dependency. For instance, the extended finite element method enriches the solution space with discontinuous functions to alleviate the cost of remeshing around cracks [104]. With an intrinsic characteristic length scale, determined by the horizon radius, the CPPD model is used in this chapter to study the origin and evolution of shear bands [105]. A rate-independent crystal elasto-plasticity model, proposed by Anand [103], is applied to simulate the mechanical response and evolution of individual grains in a polycrystal. In this constitutive model, each grain is assumed to be anisotropic with a certain orientation and plastic flow is attributed to glides of slip systems. With the Schmid factor analysis, activated slip planes are determined and the corresponding shear increment will be calculated. Activities of all single crystal are afterwards collected to simulate the developments and textures of a polycrystal. With respect to the PD stability issues, simulations in

this chapter will mostly adopt the smallest horizon radius to better compare with a continuum local CPFE formulation. First section is a brief review of crystal plasticity.

3.1 Crystal Plasticity Constitutive Model

The rate-independent crystal plasticity theory in [103] is applied to model the deformation response of particles within each crystal. In the crystal lattice coordinate frame, the deformation gradient $\mathbf{F}$ can be expressed into a multiplication of the elastic $\mathbf{F}^{\mathrm{e}}$ part and plastic $\mathbf{F}^{\mathrm{p}}$ part, which can be written as $\mathbf{F} = \mathbf{F}^{\mathrm{e}}\mathbf{F}^{\mathrm{p}}$ with $\det(\mathbf{F}^{\mathrm{p}}) = 1$. A simple schematic of the slip system under deformation is shown in Fig 3.1. More comprehesive schematics of various configurations can be referred to [7, 106, 1, 107].

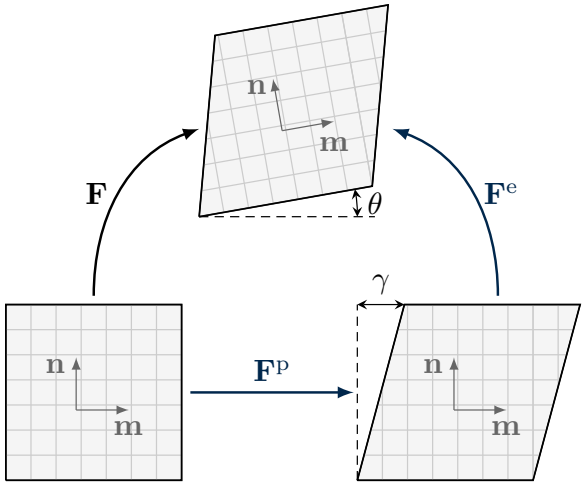

Figure 3.1: *Schematic of slip systems under deformation gradient* $\mathbf{F} = \mathbf{F}^{\mathrm{e}}\mathbf{F}^{\mathrm{p}}$. $\mathbf{m}^{\alpha}$ *and* $\mathbf{n}^{\alpha}$ *are the slip direction and normal vector, respectively.* γ *is the shear strain due to plastic deformation gradient* $\mathbf{F}^{\mathrm{p}}$ *while* θ *is the angle of rotation under elastic deformation gradient* $\mathbf{F}^{\mathrm{e}}$.

In the crystal plasticity theory, the plastic flow is attributed to dislocation gliding on prescribed slip systems. Assume there are N slip systems and the Schmid tensor of the αth slip system is $\mathbf{S}_0^{\alpha} = \mathbf{m}_0^{\alpha} \otimes \mathbf{n}_0^{\alpha}$, where $\mathbf{m}_0^{\alpha}$ and $\mathbf{n}_0^{\alpha}$ are the slip direction and normal vector at time $t = 0$, respectively. Then the plastic flow can be expressed as

a summation of efficient glides on all slip systems, which is

$$\dot{\mathbf{F}}^{\mathrm{p}}(\mathbf{F}^{\mathrm{p}})^{-1} = \sum_{\alpha} \dot{\gamma}^{\alpha} \mathbf{S}_0^{\alpha} \mathrm{sign}(\tau^{\alpha}), \tag{3.1}$$

where $\dot{\gamma}^{\alpha}$ and τ^{α} are the plastic shearing rate and resolved stress on the αth slip system, respectively.

The conjugate stress defined as $\bar{\mathbf{T}} = \det \mathbf{F}^{\mathrm{e}} (\mathbf{F}^{\mathrm{e}})^{-1} \boldsymbol{\sigma} (\mathbf{F}^{\mathrm{e}})^{-\mathrm{T}}$, in terms of the Cauchy stress $\boldsymbol{\sigma}$, is used to compute the resolved stress $\tau^{\alpha} = \bar{\mathbf{T}} \cdot \mathbf{S}_0^{\alpha}$ on the αth slip plane. Based on the constitutive relation, this conjugate stress can be obtained by $\bar{\mathbf{T}} = \mathcal{L}^{\mathrm{e}}[\bar{\mathbf{E}}^{\mathrm{e}}]$, in which $\mathcal{L}^{\mathrm{e}}$ is the fourth-order anisotropic elasticity tensor and $\bar{\mathbf{E}}^{\mathrm{e}}$ is the Green elastic strain, defined as $\bar{\mathbf{E}}^{\mathrm{e}} = \frac{1}{2}(\mathbf{F}^{\mathrm{e}\mathrm{T}} \mathbf{F}^{\mathrm{e}} - \mathbf{I})$.

To solve this elasto-plasticity crystal model, firstly, assume the slip system resistance on the αth slip system is s^{α} which works as a threshold of the resolved shear stress on the system. Only active slip systems, or those slip systems whose resolved shear stress exceeds the resistance ($\tau^{\alpha} > s^{\alpha}$), have positive shearing rates ($\dot{\gamma}^{\beta}(t) > 0$); otherwise, there is no plastic shearing rate ($\dot{\gamma}^{\beta}(t) = 0$). Secondly, the slip system resistance is evolves as:

$$\dot{s}^{\alpha}(t) = \sum_{\beta} h^{\alpha\beta} \dot{\gamma}^{\beta}(t), \text{ with } s^{\alpha}(0) = \tau_0^{\alpha}, \tag{3.2}$$

where $h^{\alpha\beta}$ is the hardening-coefficient matrix, $\dot{\gamma}^{\beta}(t) > 0$ is the plastic shearing rate on the βth slip system, and τ_0^{α} is the initial slip system resistance on the αth slip system.

Consequently, the plastic shear increment $\Delta\gamma^{\beta}$ can be solved from a matrix form (See Appendix). The plastic part of deformation gradient $\mathbf{F}^{\mathrm{p}}$ is afterwards updated using (3.1) while the elastic part computed from $\mathbf{F}^{\mathrm{e}} = \mathbf{F}(\mathbf{F}^{\mathrm{p}})^{-1}$. In order to convert the conjugate stress $\bar{\mathbf{T}}$ into the first Piola-Kirchhoff stress $\mathbf{P}$, the relation $\mathbf{P} = (\det \mathbf{F}) \boldsymbol{\sigma} \mathbf{F}^{-\mathrm{T}}$, or $\mathbf{P} = \mathbf{F}^{\mathrm{e}} \bar{\mathbf{T}} (\mathbf{F}^{\mathrm{p}})^{-\mathrm{T}}$ should be employed with the conjugate stress

computed from $\bar{\mathbf{T}} = \mathcal{L}^{\mathrm{e}}[\bar{\mathbf{E}}^{\mathrm{e}}]$. Finally, the slip resistances are updated at the end of each loading step using (3.2).

Since the equation of motion is solved by an explicit dynamic algorithm, the tangent modulus $\partial\mathbf{P}/\partial\mathbf{F}$ is not needed, which is, however, a necessary process in implicit methods, such as the Newton-Raphson method [21].

3.2 2D Numerical Examples

In planar polycrystals, each grain can be characterized by a 2D rotation tensor $\mathbf{R}$ which relates the local crystal lattice frame to the reference sample frame. Given an orientation θ, or the angle between crystal and sample axes, the associated rotation matrix supports parametrization as $\mathbf{R} = \cos(\theta)\mathbf{I} - \sin(\theta)\mathbf{E}$, where $\mathbf{E}$ is the 2D alternator ($E_{11} = E_{22} = 0, E_{12} = -E_{21} = 1$) and $\mathbf{I}$ is the 2D identity tensor. Due to planar symmetry, crystal orientations can be identified by parameters from a fundamental region $[-\pi/2, \pi/2)$, in which crystals with orientation $\theta = \pi/2$ are identical to those with $\theta = -\pi/2$.

The rotation tensor $\mathbf{R} = \mathbf{R}^e$ is evaluated through a polar decomposition of the elastic deformation gradient as $\mathbf{F}^e = \mathbf{R}^e\mathbf{U}^e$, the spin tensor $\mathbf{\Omega}$ is then defined as $\mathbf{\Omega} = \dot{\mathbf{R}}^e\mathbf{R}^{e\mathrm{T}} = -\dot{\theta}\mathbf{E}$, where $\dot{\theta} = \frac{\partial\theta}{\partial t}$ is the crystal reorientation velocity. In the component form, the crystal reorientation velocity can be expressed as $\dot{\theta} = (\Omega_{21} - \Omega_{12})/2$. Using the reorientation velocity, the crystal texturing is tracked by $\Delta\theta = \dot{\theta}\Delta t$ at each time step.

A 1×1 mm^2 polycrystalline microstructure with 21 grains, computationally generated by Voronoi construction, is considered here. The discretized computational domain is based on a pixel mesh (four-node square elements) and PD particles are located at the center of these elements. Each particle occupies a constant volume in the reference configuration equal to the area of the corresponding enclosed finite element. Twelve different orientations within the interval $[-\pi/2, \pi/2)$ are distributed

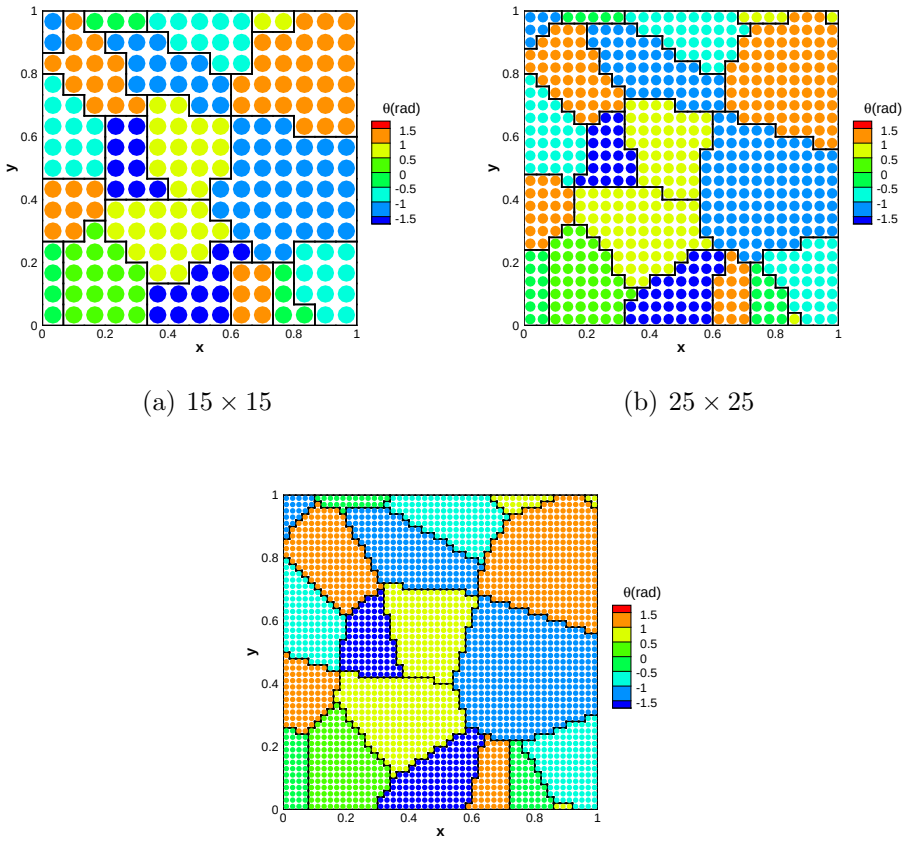

(a) 15×15 (b) 25×25

(c) 50×50

Figure 3.2: *Particle grids with three different mesh sizes. Orientation θ is the angle between the crystal and x axis. Particles are located at the center of elements in pixel-based grids.*

with a constant step size $\pi/12$ among grains. Three particle grids based on different mesh sizes are generated and shown in Fig. 3.2. Two slip systems at orientations $-\pi/6$ and $+\pi/6$ are considered.

The particular hardening law in (3.2) is chosen as follows [103]:

$$h^{\alpha\beta} = h_0^{\beta}(q + (1-q)\delta^{\alpha\beta})(1 - \frac{s^{\beta}(t)}{s_s^{\beta}})^a \text{ (no sum on } \beta), \tag{3.3}$$

where h_0^{β}, $s^{\beta}(t)$, and s_s^{β} are the hardening coefficient, the current resistance, and the saturation resistance of slip system β, respectively; $\delta^{\alpha\beta}$ is the Kronecker delta

function; a and q are constant terms. These hardening parameters are taken to be identical for both slip systems and are listed below:

$$h_0 = 10\text{MPa},\ s(0) = 10\text{MPa},\ s_s = 200\text{MPa},\ a = 2,\ q = 1.4, \tag{3.4}$$

where $s(0)$ is the initial value of slip system resistance.

A displacement boundary condition is enforced on boundary particles, which is $\mathbf{u} = \big(\exp(\mathbf{L}_{\text{vg}}t) - \mathbf{I}\big)\mathbf{x}$, where $\mathbf{L}_{\text{vg}} = \dot{\mathbf{F}}\mathbf{F}^{-1}$ is a macroscopic velocity gradient, t is time, and $\mathbf{I}$ is the 2D identity tensor. In the following examples, two different velocity gradients with the plane strain assumption are applied on microstructure boundaries to simulate the process of X-axis shear and Y-axis compression, respectively. They are

$$\mathbf{L} = \eta \begin{bmatrix} 0 & 1 \\ 1 & 0 \end{bmatrix} \text{(shear) and } \mathbf{L} = \eta \begin{bmatrix} 1 & 0 \\ 0 & -1 \end{bmatrix} \text{(compression)}, \tag{3.5}$$

where $\eta = 0.0020$ is a constant strain rate. Each simulation are performed over 30 steps with the corresponding velocity gradient leading to a final strain around 0.06. The 2D elastic stiffness matrix is taken as $D_{11} = 2$ GPa, $D_{12} = 1$ GPa, and $D_{33} = 2$ GPa.

3.2.1 Convergence tests under pure shear

The first test is to demonstrate the accuracy and mesh convergence of the new dynamic CPPD model. In order to compare with the CPFE model, the horizon radius in the PD model is kept minimum merely including the nearest neighbor particles and the influential function ω is set to be constant 1. With a constant influcence function, the deformation gradient definition is identical to that proposed by Zimmerman et at in 2009 [108] for modeling atomistic deformtation. Although not considered in this work, one may note that the influence function play much the same role as the

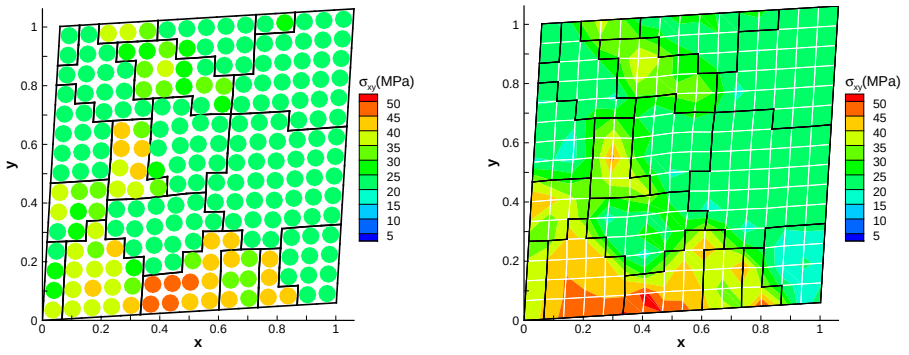

(a) 15×15, CPPD

(b) 15×15, CPFE

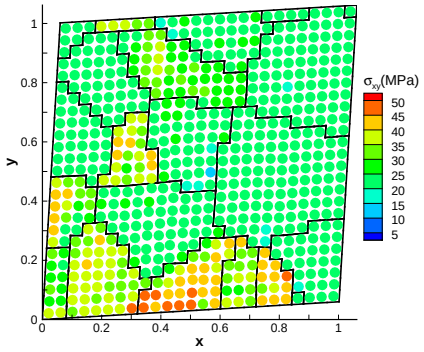

(c) 25×25, CPPD

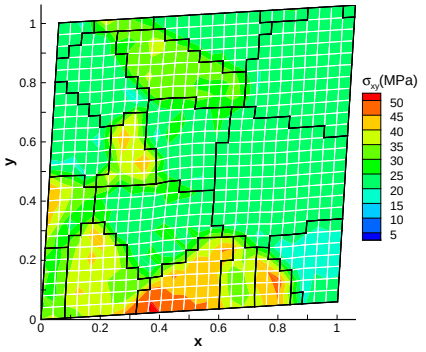

(d) 25×25, CPFE

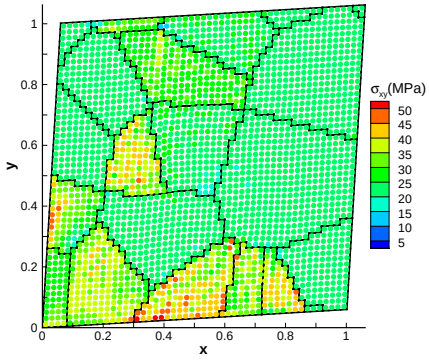

(e) 50×50, CPPD

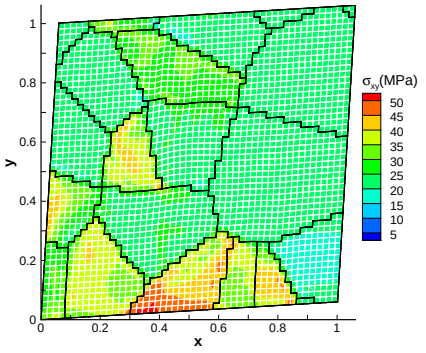

(f) 50×50, CPFE

Figure 3.3: *Comparison of σ_{xy} from CPPD and CPFE models in the pure shear test with a 225 particles/elements mesh in (a,b), a 625 particles/elements mesh in (c,d), and a 2500 particles/elements mesh in (e,f) at total strain of 0.06.*

nonlocal kernel in Eringen-type theories [109]. For instance, the dispersion curves of the material can be modulated using different forms of ω, going form a linear dispersion in continuum limit to nonlinear dispersion curves when using different influence parameters as shown in [110]. Secondly, by limiting to the nearest neighbor interactions, our formulation ensures both compatibility and traction continuity similar to the finite element problem.

Particles in the PD model are located at the center of elements in CPFE with the number of particles same as the number of elements. Linear basis functions and traditional implicit solver are employed in the CPFE model. Though different solvers are applied in CPPD and CPFE models, the same constraint on errors is set to be $e_l = 10^{-6}$. Particles in the PD simulation are colored with field values to compare with finite element contours obtained from the CPFE model. In Fig. 3.3, the shear stress σ_{xy} obtained from CPPD and CPFE models are compared at the final strain of 0.06 in 225, 625, and 2500 elements, respectively. The overall stress distribution and locations of maximum and minimum stresses are similar between these two models at the same degree of mesh refinement. Features of the stress response, such as the regions of stress concentration, are improved in the CPPD results as the mesh is refined.

In the case of CPPD with 2500 elements, two relative errors, $e_{1,2}$, and artificial damping ratios are monitored. Fig. 3.4 is the convergence plot of the CPPD-ADRS model at different loading steps. Both criteria $e_1 < 10^{-6}$ and $e_2 < 10^{-6}$ are satisfied. The damping ratio oscillates dramatically in a range from 10^0 to 10^4 at the start and becomes stable towards the end. A comparative test with a constant damping ratio $c = 500$ is carried out and the adaptive dynamic relaxation method is demonstrated as converging faster and stably with the CPPD model during different loading steps in both elastic and plastic regions.

Finally, a comparison is conducted between the explicit CPPD model and implicit

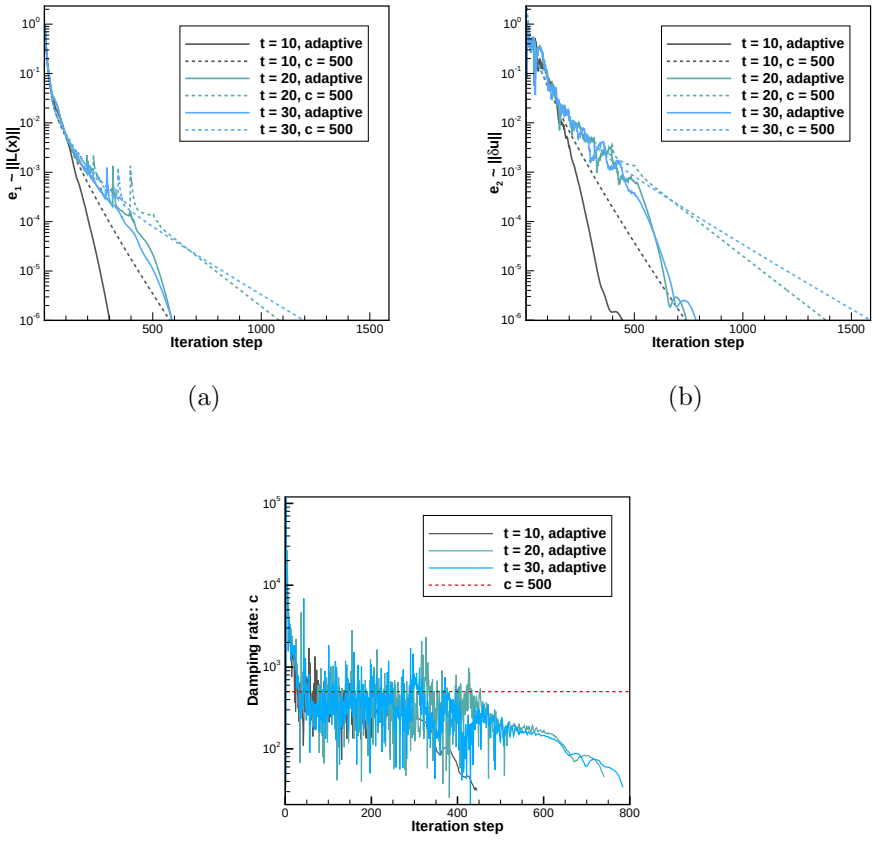

Figure 3.4: *The convergence plot of the dynamic CPPD model in the pure shear test with 2500 elements. Two relative errors, $e_{1,2}$, and artificial damping ratios are monitored during iterations in (a), (b), and (c), respectively, during iterations at $t = 10$, $t = 20$, and $t = 30$ (or at strain of 0.02, 0.04, and 0.06). A comparative test with a constant damping rate $c = 500$ is plotted in dashed lines.*

CPPD model from [21]. Three different mesh sizes are tested and both explicit and implicit simulations were run in the same single-core workstation without parallelization. The absolute error ϵ_1 in (2.48) and relative error e_1 in (2.49) are monitored in both models considering that these two errors indicate the extent to which convergence is achieved. $\varepsilon_1 < 10^{-6}$ and $e_1 < 10^{-6}$ are employed to be the convergence criteria. The computation time is divided into two parts, where the first includes the first 7 loading steps when material is mainly in the elastic region and the second one

contains the last 23 loading steps in the plastic region. The computational time for both models are illustrated in Fig. 3.5 in log-scale.

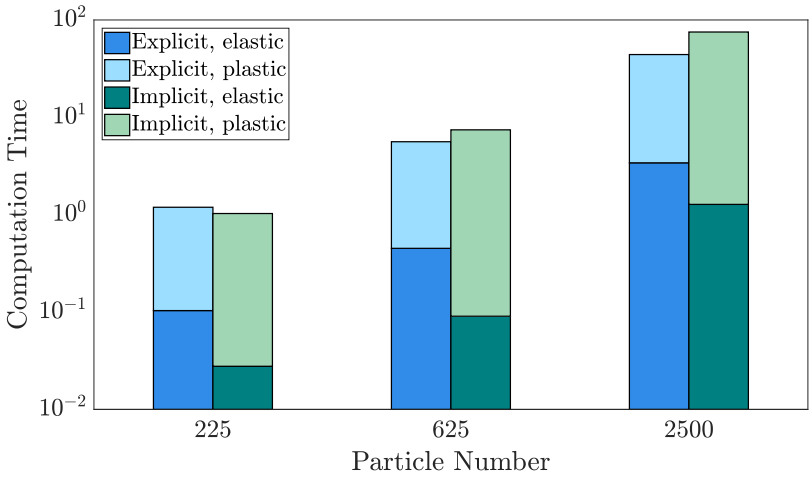

Figure 3.5: *Comparison of numerical efficiency between explicit and implicit CPPD models. The computation time is plotted in a log scale and normalized with the case of implicit model with 225 particles.*

For implicit methods, computation cost is mainly spent in computing the tangent modulus and inverting the global stiffness matrix [21]. In contrast, the explicit method is matrix-free and the speed primarily depends on the number of constitutive function calls. This explains why the implicit model is faster in the elastic region where tangent computation is avoided and it can converge in one iteration. Explicit methods are more stable and efficient in the plastic region where most of the simulation is carried out. As the particle number increases, the implicit model becomes more expensive because of repeated matrix inversion needed during convergence. In the plastic region, the explicit CPPD model's computational speed surpasses the implicit model.

3.2.2 Reorientation of grains and mircrostructural study of shear bands in a Y-axis compression test

Following is a Y-axis compression test based on the same microstructure in the previous pure shear test. Reorientation of grains predicted by CPPD and CPFE

models are compared in Fig. 3.6 at strain of 0.06. Significant reorientation is seen whithin shear bands in both models. The overall contours are similar. Although the locations and orientations of shear bands are identical, the localization bands seen from CPFE simulations are comparatively more diffuse due to lack of an internal length scale. Along the direction of arrows in Fig. 3.6, the width of a shear band obtained by CPPD simulations is smaller and its boundary is more conspicuous, which are qualitatively closer to those seen in experiments [4, 5]. In this example, the CPPD-ADRS model is shown capable of capturing sharp shear bands with an explicit length scale in the form of an interaction radius bridging two nearest particles. Some additional banding can be seen in CPPD results besides the one marked with an arrow. Same simulation results were found in [21], however, with an implicit Newton-Raphson method.

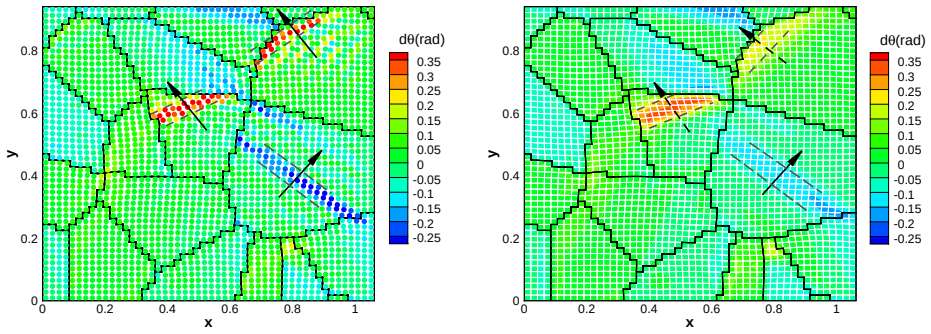

(a) (b)

Figure 3.6: *Orientation changes for 2500 particles under a Y-axis compression test from (a) CPPD (b) CPFE results at strain of 0.06. Along the direction of arrows, sharper and more number of shear bands can be seen in CPPD results.*

3.2.3 Study of the dependence of shear bands on initial orientation distributions

The CPPD-ADRS model is used to study the origin and evolution of shear bands on three different microstructures. The first microstructure applied is identical to that of the pure test while the other two are shown in Fig. 3.7. The structures and positions of grains in these three microstructures stay the same, however, the orientations of grains are assigned differently. The Y-axis compression boundary condition in (3.5) is applied.

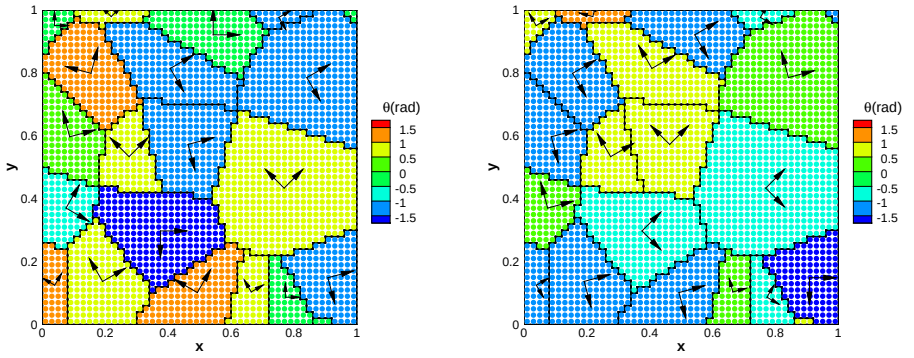

(a) (b)

Figure 3.7: *Microstructures 2 and 3 represented by 21 planar grains for CPPD simulations. Initial orientations are represented by a group of two arrows. The microstructure in the pure test in Fig. 3.2 is employed as microstructure 1.*

First off, potential active slip systems are identified using a rudimentary Schmid factor analysis. Let $\mathbf{l}_c$ and $\mathbf{l}_s$ be the loading axis in the current crystal frame and sample reference frame, respectively, and $\mathbf{l}_s = [1, 0]^T$ (or $\mathbf{l}_s = [0, -1]^T$, since their Schmid factors are the same). Then the loading axis in the current frame can be represented as $\mathbf{l}_c = \mathbf{R}^T\mathbf{l}_s$ where $\mathbf{R}$ is the rotation tensor in one crystal. Next, the Schmid factor for αth slip system is obtained by $\mathbb{S}^\alpha = |(\mathbf{m}_0^\alpha \cdot \mathbf{l}_c)(\mathbf{n}_0^\alpha \cdot \mathbf{l}_c)|$. Finally, the maximum Schmid factor is marked as the active system. Figs. 3.8(a), 3.9(a), and 3.10(a) are plots of the maximum Schmid factor in each grain for three different

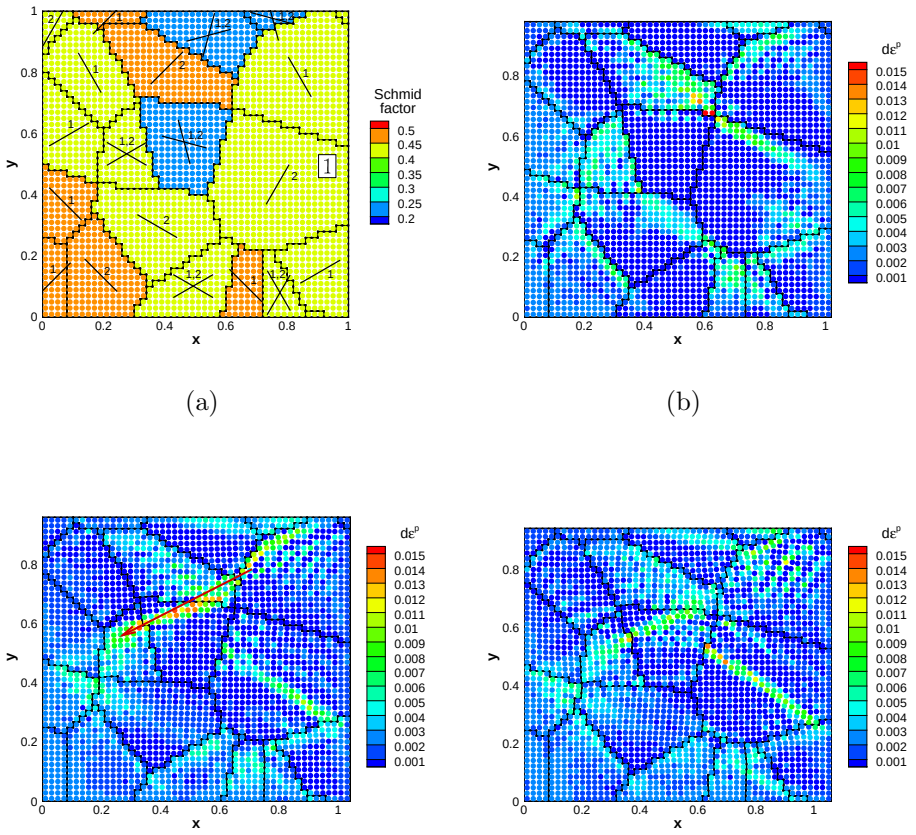

Figure 3.8: *Microstructure 1. (a) is the plot of the maximum Schmid factor in each grain with Grain 1 labeled. The equivalent plastic strain increment is shown in (b) at strain of 0.02, (c) at strain of 0.04, and (d) at strain of 0.06. The red arrow in (c) indicates a track of shear bands transmission across grains.*

microstructures. Each grain is marked with the slip system number ($\alpha = 1, 2$) that gives the maximum Schmid factor. If the Schmid factor for both slip systems are equal, both systems are marked in one grain. In that case, to distinguish the slip system numbers, travel clockwise. Since the angle between two slip directions is always an acute angle of $\pi/3$, the first slip line encountered before the acute angle is the 2nd slip system.

Evolutions of the equivalent plastic strain increment [1] are shown as a function of

[1]The equivalent plastic strain increment is defined as ([57]) $d\epsilon^{\mathrm{p}} = \frac{\sum_\alpha \tau^\alpha \Delta\gamma^\alpha}{\sigma_{\mathrm{eff}}}$, where σ_{eff} is the

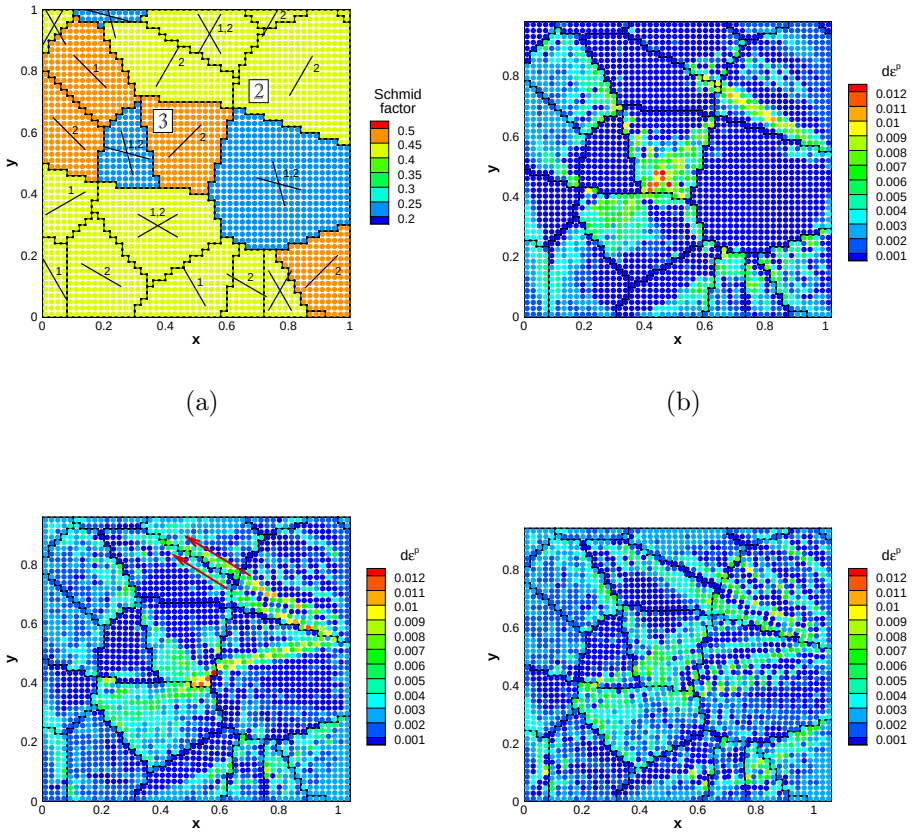

Figure 3.9: *Microstructure 2. (a) is the plot of the maximum Schmid factor in each grain with Grain 2 and 3 labeled. The equivalent plastic strain increment is shown in (b) at strain of 0.02, (c) at strain of 0.04, and (d) at strain of 0.06. The red arrow in (c) indicates a track of shear bands transmission across grains.*

the effective strain in Figs. 3.8, 3.9, and 3.10 for three microstructures. At low strain or strain of 0.02, deformation processes primarily occur in grains with high Schmid factors while little plasticity, if any, is seen in grains with the lowest Schmid factor. As the loading is increased, strain localization emerges in the form of a laminated pattern. Consequently, a new lamellar structure is generated with plentiful fine shear bands, as shown in Figs. 3.8(d), 3.9(d), and 3.10(d).

During this process, shear bands are transmitted from grains with higher Schmid

von Mises stress.

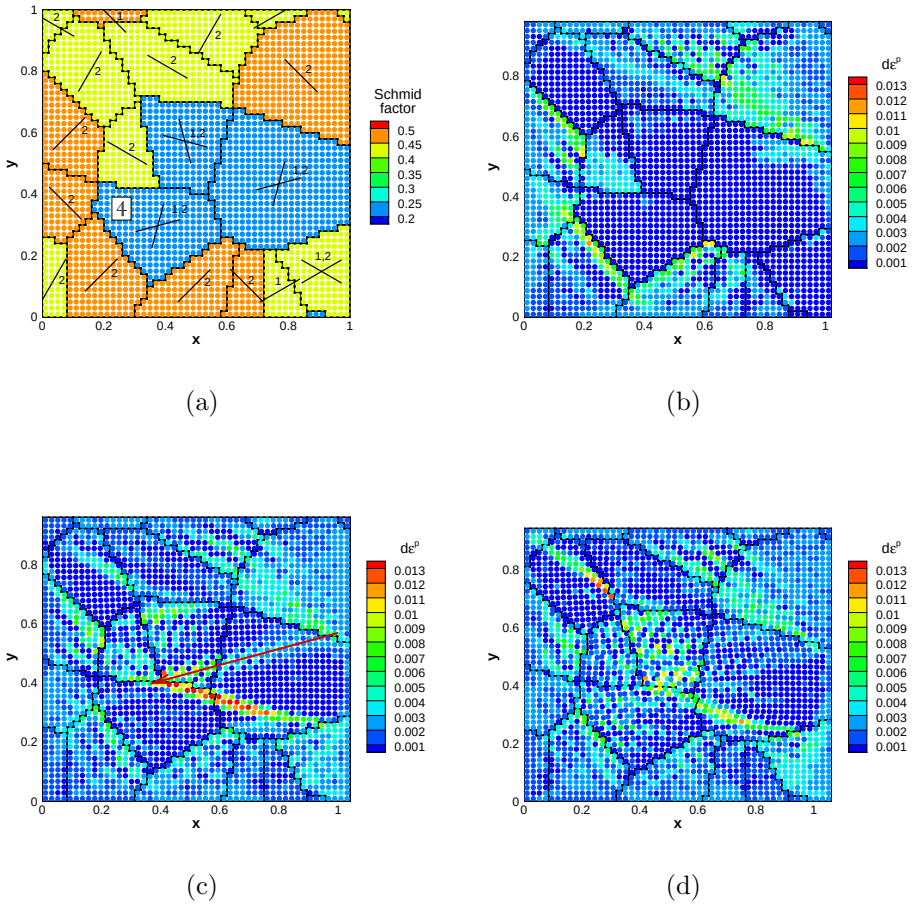

Figure 3.10: *Microstructure 3. (a) is the plot of the maximum Schmid factor in each grain with Grain 4 labeled. The equivalent plastic strain increment is shown in (b) at strain of 0.02, (c) at strain of 0.04, and (d) at strain of 0.06. The red arrow in (c) indicates a track of shear bands transmission across grains.*

factors to those with lower Schmid factors and merge into larger ones. This is a possible deformation mechanism in grains not favorably oriented for slip activity [21]. Red arrows show the track of transmission in Figs. 3.8(c), 3.9(c), and 3.10(c). One particular case of slip transmission can be found in Fig. 3.9(c). Grain 2 in microstructure 2 and the grain to its left are grains with slip system 2 active. At higher strain, shear bands travel through grain 2 and merge into the grains to its left.

Intensified plastic strain arises across grain boundaries that separate low and high Schmid factor grains. This is due to the inability of high-Schmid-factor grains to

transmit slip activity across to those grains with low Schmid factor. One example can be found at the grain boundary of Grain 3 in Fig. 3.9(b, c). Grain 3 is a grain with a high Schmid factor between two low-Schmid-factor grains. Another example is Grain 4 in Fig. 3.10(b, c, d), which is a low-Schmid-factor grain surrounded with high-Schmid-factor grains. Strong plastic strain is generated at the boundaries of these two grains, however, Grain 4 has localized strain around it rather than inside it. These grain boundaries may trigger cracks.

In order to identify the active slip systems within shear bands, maps of plastic shearing increments ($\Delta\gamma^1$ and $\Delta\gamma^2$) on slip systems 1 and 2 for Grain 1 in microstructure 1 at final strain of 0.06 are plotted in Fig. 3.11. Low strain is found in slip system 1 while shear bands are formed in slip system 2 as expected from the Schmid factor analysis. Particle alignments around the shear band are drawn with green lines in Fig. 3.11(b). The direction of alignment is the slip direction of slip system 2 in Grain 1 in Fig. 3.8(a), which is nearly perpendicular to the direction of the shear band. This is because dislocations are grouped along slip directions.

3.2.4 Stress-strain response

The homogenized stress-strain response of CPPD and CPFE models are compared in Fig. 3.12 for microstructures 1 and 2. The elastic responses for both models are very close, however, divergence occurs in the elasto-plastic region. The CPPD model shows an overall softer response in plastic regions, i.e., at the same strain level, the averaged stresses are lower. This is mainly due to sharper stress localizations or smaller regions with high stress in the CPPD model compared to the CPFE model.

3.3 Conclusions

A CPPD model with APDR is presented in this study. CPPD results are compared with the CPFE analysis on plane strain problems under pure shear and compression.

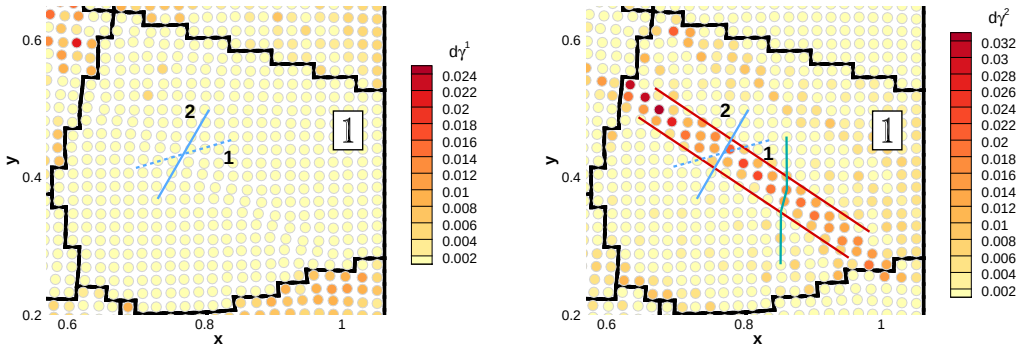

(a) (b)

Figure 3.11: *Plastic shear increments in grain 1 of microstructure 1 at strain of 0.06 for (a) slip system 1 and (b) slip system 2. Blue lines denote slip directions; red lines indicate shear bands; the green line shows the particle alignment across the shear band. The direction of the particle alignment is parallel to the slip direction of slip system 2 while nearly perpendicular to the shear band.*

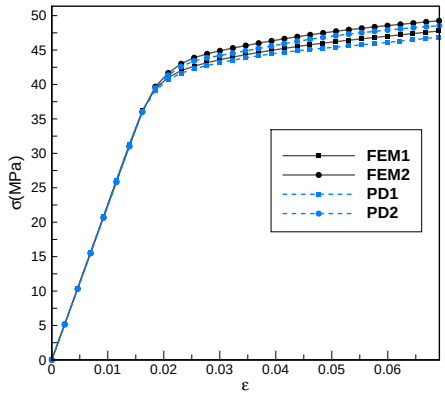

Figure 3.12: *Homogenized stress-strain responses from CPPD and CPFE models for microstructures 1 and 2 under Y-axis compression. CPPD stress is always lower than CPFE stress due to finer shear bands in CPPD results during plastic loadings.*

The mechanical properties, texturing, and stress-strain response predicted by two models are found to be largely similar. One highlight of the CPPD-ADRS model is its simplicity and numerical efficiency compared to implicit methods in the plastic

regime.

In the numerical results, shear bands show inhomogeneity in the plastic deformation and reorientation. Shear bands can merge and spread into grains, which are originally unfavorable to slip at small effective strain. Next chapter will introduce a more sophisticated control method of instabiltiy in state-based peridynamics. Larger horizons will be employed.

CHAPTER IV

Higher-Order Approximation to Suppress Zero-Energy Modes in PD-ADRS with Larger Horizons

Previous chapters have investigated the ability of CPPD models in handling strong strain gradients. Those results are restricted to the nearest-neighbor PD family. However, larger horizons are generally more preferable in the PD convergence test and damage analysis. Therefore, this chapter will investigate stable numerical solutions with PD-ADRS in the larger horizon families.

The most troublesome stability issue of the NOSB peridynamics is the zero-energy mode [111], which will be elaborated in the next section. In general, larger horizons exhibit stronger zero-energy modes compared to those of smaller horizons. Those accumulated zero-energy modes, shown as numerical oscillations, can eventually ruin the results. Fig. 4.1 provides an example of disordered results when we simply increase the horizon size in the CPPD model presented in the previous chapter with no control method applied. Though we can still observe a general outline in Fig 4.1(b) with $\delta = \sqrt{2}h$, zero-energy-mode noise has dominated and destroyed the results in Fig 4.1. In this example, the influence function ω is set to be 1 for all neighbor particles.

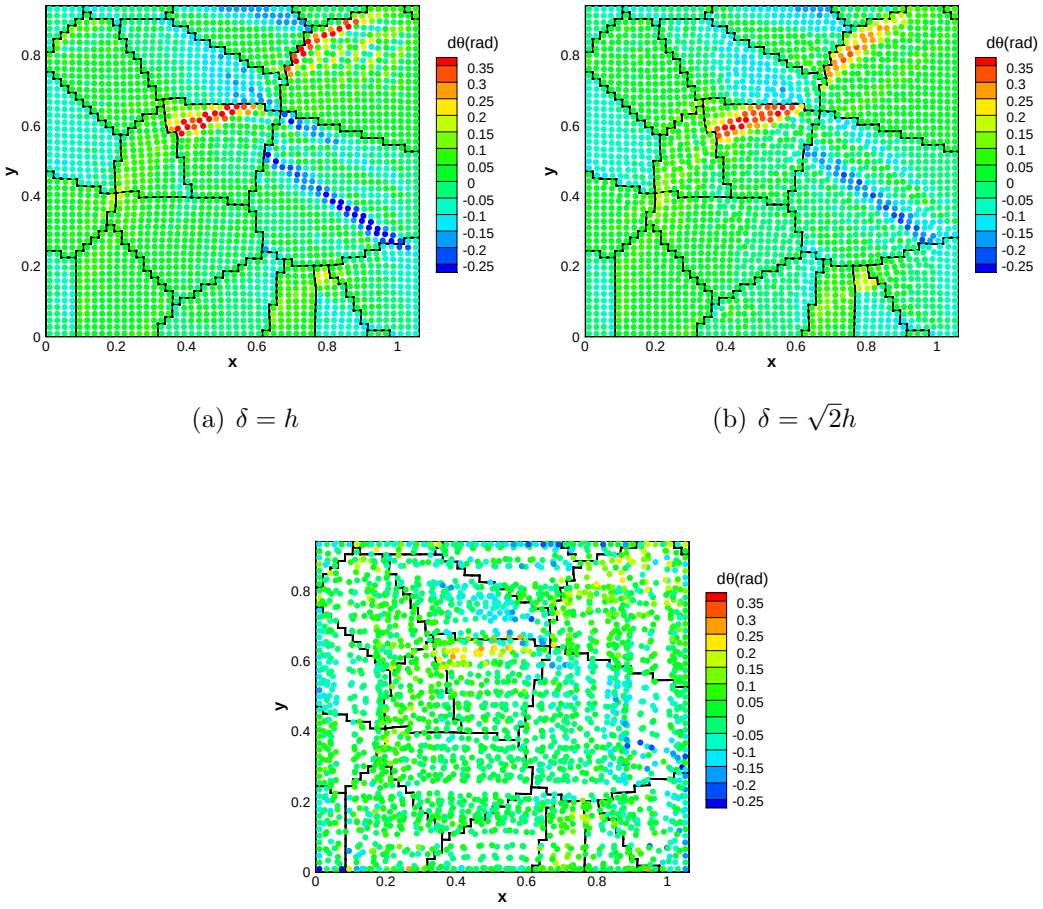

(a) $\delta = h$

(b) $\delta = \sqrt{2}h$

(c) $\delta = 2h$

Figure 4.1: *The effect of zero-energy modes in 2D CPPD results with different horizon sizes. h is the distance between nearest particles and δ is the horizon size. The influence function is set to be a constant among all neighbor particles in one horizon.*

4.1 Zero-Energy Modes

If a stress tensor is used as an intermediate step in determining the bond forces, it is called correspondence material model. Thus, the PD model in this thesis is a peridynamic correspondence material model based on (2.26), where the PKI stress $\mathbf{P}$ is used in determining the force state. Zero-energy modes have been demonstrated to be a material instability rather than a numerical instability in correspondence

materials [102]. Weak couplings between particles is one of the inherent reasons [87, 88, 89, 93]. A simple example is discussed below to help understanding its origin.

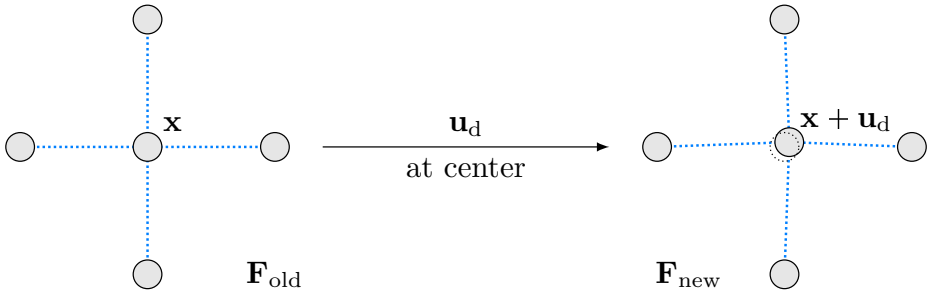

Figure 4.2: *An illustration of zero-energy modes in a 2D regular quadrilateral lattice. Although a small displacement disturbance* $\mathbf{u}_d$ *is applied on the center particle* $\mathbf{x}$*, there is no impact on calculating the deformation gradient.*

Consider a 2D regular quadrilateral lattice shown in Fig. 4.2. The original deformation gradient is $\mathbf{F}_\mathrm{old}$. A small displacement disturbance $\mathbf{u}_\mathrm{d}$ is then applied on the center particle $\mathbf{x}$. Based on (2.19), the new deformation gradient $\mathbf{F}_\mathrm{new}$ turns into

$$\begin{aligned}
\mathbf{F}_\mathrm{new} &= \Big(\int_{\mathcal{H}_\mathbf{x}} \omega(\underline{\mathbf{Y}}_\mathrm{new} \otimes \boldsymbol{\xi}) dV_{\mathbf{x}'}\Big)\mathbf{K}^{-1} \\
&= \Big(\int_{\mathcal{H}_\mathbf{x}} \omega\big[(\underline{\mathbf{Y}}_\mathrm{old} - \mathbf{u}_\mathrm{d}) \otimes \boldsymbol{\xi}\big] dV_{\mathbf{x}'}\Big)\mathbf{K}^{-1} \\
&= \mathbf{F}_\mathrm{old} - \mathbf{u}_\mathrm{d} \otimes \Big(\int_{\mathcal{H}_\mathbf{x}} \omega\boldsymbol{\xi} dV_{\mathbf{x}'}\Big)\mathbf{K}^{-1}. \qquad (4.1)
\end{aligned}$$

Due to the assumption of a uniform lattice discretization and a spherically symmetric influence function ω, the integration term on the right hand side becomes zero. This is a case of admissible displacement fields producing the same deformation gradient and potential energy, which is reasonably called zero-energy modes, or hourglass modes. The missing role of the center particle is one of the causes of zero-energy modes, which is a common stability issue when using correspondence material models in mesh-free methods, FEM, and numerical schemes with central difference discretization [7, 16,

100, 112].

Though there are several numerical methods to handle this practical difficulty, the higher-order approximation approach seems to be the best choice considering its feasibility and efficiency in problems with regular discretization patterns. We have made a thorough discussion on its accuracy and stability in the 1D elastic bar tension test in Chapter VI compared with other numerical control methods. In this chapter, we review the derivation and formulation of the higher-order approximation approach in different dimensions, and then focus on applying this method in the 2D CPPD model.

4.2 Higher-Order Approximation Theory

The higher-order approximation method is firstly proposed in Ref. [93]. The basic idea is to adjust the weight or influence function values based on the Taylor series expansions to better approximate the deformation gradient. This approach is demonstrated highly effective in suppressing zero-energy modes, though, not completely eliminating it. We describe another method that completely eliminates it albeit at a higher computational cost in Chapter VI. More importantly, higher order approximations are easily implementable within the state-based peridynamics framework where larger horizons can be used. A brief introduction is given below.

In the continuum mechanics, the difference between the deformed bond $\mathbf{y}' - \mathbf{y}$ and the reference bond $\mathbf{x}' - \mathbf{x}$, as shown in Fig. 4.3, can be expressed using the Taylor series expansion as

$$\mathbf{y}' - \mathbf{y} = \frac{\partial \mathbf{y}}{\partial \mathbf{x}}(\mathbf{x}' - \mathbf{x}) + O[(\mathbf{x}' - \mathbf{x})^2], \tag{4.2}$$

where the notation O denotes the order of the leading error term; $\frac{\partial \mathbf{y}}{\partial \mathbf{x}} = \mathbf{F}$, which is the classical definition of the deformation gradient tensor.

In order to compare with the state-based peridynamic deformation gradient, we

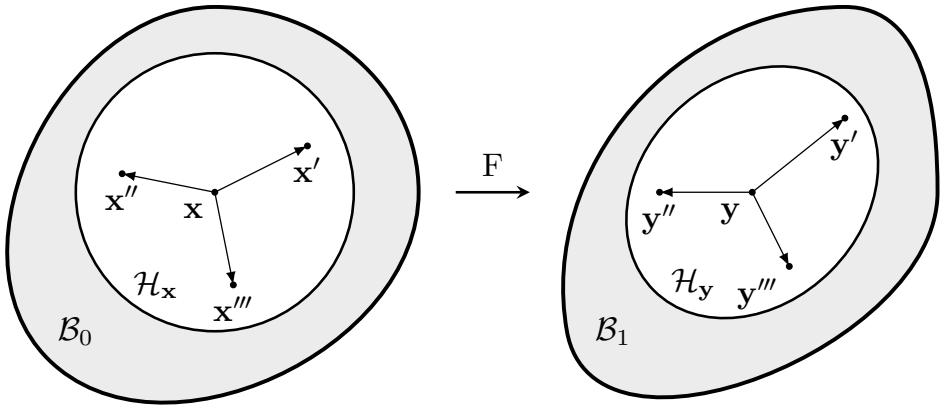

Figure 4.3: *Kinematics of non-ordinary state-based peridynamics. Particle* $\mathbf{x}$ *is bonded to neighboring particles (*$\mathbf{x}'$*,* $\mathbf{x}''$*, and* $\mathbf{x}'''$*) within a region* $\mathcal{H}_\mathbf{x}$*. Under the deformation, particle* $\mathbf{x}$ *maps to particle* $\mathbf{y}$ *and this process can be described by a corresponding deformation gradient* $\mathbf{F}$*.*

consider performing the tensor product on the reference bond $\mathbf{x}' - \mathbf{x}$ and then integrating both sides on the horizon:

$$\int_{\mathcal{H}_\mathbf{x}} \omega[(\mathbf{y}' - \mathbf{y}) \otimes (\mathbf{x}' - \mathbf{x})] dV_{\mathbf{x}'} = \int_{\mathcal{H}_\mathbf{x}} \frac{\partial \mathbf{y}}{\partial \mathbf{x}} \omega[(\mathbf{x}' - \mathbf{x}) \otimes (\mathbf{x}' - \mathbf{x})] dV_{\mathbf{x}'} + O[(\mathbf{x}' - \mathbf{x})]^3, \quad (4.3)$$

where ω is the weight or influence function.

Therefore, the deformation gradient tensor can be approximated by

$$\mathbf{F}(\mathbf{x}) = \frac{\partial \mathbf{y}}{\partial \mathbf{x}} = \left(\int_{\mathcal{H}_\mathbf{x}} \omega[(\mathbf{y}' - \mathbf{y}) \otimes (\mathbf{x}' - \mathbf{x})] dV_{\mathbf{x}'} \right) \mathbf{K}^{-1} + O(\mathbf{x}' - \mathbf{x}), \quad (4.4)$$

where $\mathbf{K} = \int_{\mathcal{H}_\mathbf{x}} \omega[(\mathbf{x}' - \mathbf{x}) \otimes (\mathbf{x}' - \mathbf{x})] dV_{\mathbf{x}'}$. If we ignore the error term, the first term on the left is the same as (2.19) and $\mathbf{K}$ is defined as the shape tensor in the state-based peridynamics. Note that the leading error term in (4.4) is the first order of the distance between particles $\mathbf{x}'$ and $\mathbf{x}$. In order to achieve more accurate deformation gradient, we can choose appropriate ω in the horizon to artificially increase the leading error order.

4.3 Discrete Formulation

4.3.1 1D discretization

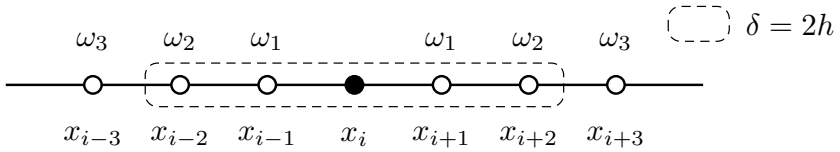

Figure 4.4: *1D particle-discretized bar with a constant spacing h. ω is a symmetric weight function on neighboring particles. Dashed box $\delta = 2h$, where δ is the horizon radius, illustrates the horizon of center particle x_i including only the nearest four particles.*

Consider a 1D particle-discretized bar with a constant particle spacing $h = x_{i+1} - x_i$. As illustrated in Fig. 4.4, there are 5 particles x_{i+j} as $j = 0, \pm 1, \pm 2$ within the horizon $\delta = 2h$, where δ is the horizon radius. The weight function is selected to be symmetric, i.e., $\omega_j = \omega(|x_{i+j} - x_i|) = \omega(|x_{i-j} - x_i|)$.The state-based peridynamic deformation gradient, defined in (2.19), can then be expressed as

$$F(x_i) = \frac{2h\omega_2(y_{i+2} - y_{i-2}) + h\omega_1(y_{i+1} - y_{i-1})}{2h^2(4\omega_2 + \omega_1)}. \tag{4.5}$$

The 1D Taylor series expansion of the deformed bond $y_{i+j} - y_i$ is

$$y_{i+j} - y_i = jh\frac{\partial y}{\partial x}\bigg|_{x_i} + \frac{(jh)^2}{2!}\frac{\partial^2 y}{\partial x^2}\bigg|_{x_i} + \frac{(jh)^3}{3!}\frac{\partial^3 y}{\partial x^3}\bigg|_{x_i} + O(h^4). \tag{4.6}$$

Substitute (4.6) into (4.5), the deformation gradient turns into

$$F(x_i) = \frac{\partial y}{\partial x}\bigg|_{x_i} + \frac{h^2}{6}\frac{(16\omega_2 + \omega_1)}{(4\omega_2 + \omega_1)}\frac{\partial^2 y}{\partial x^2}\bigg|_{x_i} + O(h^4). \tag{4.7}$$

Notice that the second term on the right hand side could vanish if $16\omega_2 + \omega_1 = 0$, and the leading error will become the fourth order of h. In other words, $\omega_1 = 1$ and $\omega_2 = -1/16$ will produce a leading error $O(h^4)$ for the horizon size $\delta = 2h$.

Same procedures can be followed to find appropriate ω values for different horizon sizes, which is shown in Table 4.1. In general, the order of leading error increases as the horizon grows, which makes the approximation of the deformation gradient more accurate.

Table 4.1: *Higher-order approximation weight functions for 1D particle discretization with a constant spacing h.*

Horizon size	Weight function values			Leading error
	ω_1	ω_2	ω_3	
$\delta = h$	1	0	0	$O(h^2)$
$\delta = 2h$	1	-1/16	0	$O(h^4)$
$\delta = 3h$	1	1/135	-1/10	$O(h^6)$

4.3.2 Higher-dimensional discretization

Higher-dimensional Taylor series expansion is applied on deriving weight functions in 2D and 3D discretization patterns. This study only considers uniform particle discretizations, i.e., quadrilateral patterns in 2D and cubic patterns in 3D, with constant spacing h and particle volume ΔV. The influence function ω is always assumed to be spherically symmetric, i.e., $\omega = \omega(|\boldsymbol{\xi}|)$. For sake of simplicity, the Einstein tensor notation is adopted in this section.

As shown in Fig. 4.3, the deformed and reference bonds can be redefined as

$$\delta\mathbf{y} = \mathbf{y}' - \mathbf{y}, \text{ and } \delta\mathbf{x} = \mathbf{x}' - \mathbf{x}, \tag{4.8}$$

respectively. The shape tensor $\mathbf{K}$ in (2.20) and deformation gradient tensor $\mathbf{F}$ in

(2.19) can be expressed in Einstein notation:

$$K_{ij} = \int_{\mathcal{H}_{\mathbf{x}}} \omega \delta x_i \delta x_j dV_{\mathbf{x}'}, \tag{4.9}$$

$$F_{pq} = (\int_{\mathcal{H}_{\mathbf{x}}} \omega \delta y_p \delta x_j dV_{\mathbf{x}'})(K^{-1})_{jq}. \tag{4.10}$$

Because of the symmetry of the discretization, the shape tensor in (4.9) becomes

$$K_{ij} = \sum_{a=1}^{N} \omega_a (\delta x_i \delta x_j)_a \Delta V = \Omega(\omega_1, \omega_2, \omega_3, ...) h^2 \Delta V \delta_{ij}, \tag{4.11}$$

where N is the total number of neighbor particles in the horizon $\mathcal{H}_{\mathbf{x}}$; Ω is a function of all independent omegas in the horizon; δ_{ij} is the Kronecker delta function.

A 2D example with a horizon size $h = 2\delta$ is shown in Fig. 4.5. While there are totally 12 neighboring particles, only three independent weight function values are labeled in the horizon, i.e., $\omega_1 = \omega(h)$, $\omega_2 = \omega(\sqrt{2}h)$, and $\omega_3 = \omega(2h)$ due to the symmetry of ω.

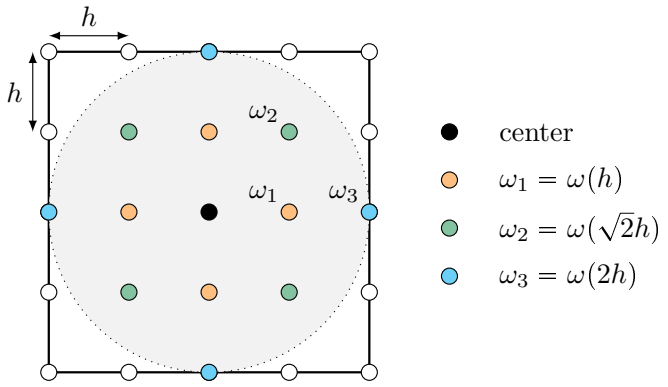

Figure 4.5: *Independent weight function values on a 2D quadrilateral particle pattern. ω is a spherically symmetric weight function on neighboring particles. The horizon radius is $\delta = 2h$, where h is the distance between nearest particles.*

Substitute (4.11) into (4.10), the deformation gradient can be simplified as

$$F_{pq} = (\int_{\mathcal{H}_{\mathbf{x}}} \omega \delta y_p \delta x_j dV_{\mathbf{x}'}) \delta_{jq} / h^2 \Omega \Delta V = \frac{1}{h^2 \Omega} \sum_{a=1}^{N} \omega_a (\delta y_p \delta x_q)_a. \tag{4.12}$$

Multidimensional Taylor series expansion of the deformed bond $\delta\mathbf{y}$ on the reference bond $\delta\mathbf{x}$ is needed. The first three terms are claimed here without proof:

$$\delta y_p = F_{pi} \delta x_i + \frac{1}{2!} G_{pij} \delta x_i \delta x_j + \frac{1}{3!} H_{pijk} \delta x_i \delta x_j \delta x_k + O(h^4), \tag{4.13}$$

where $F_{pi} = \partial \delta y_p / \partial \delta x_i$ is the deformation gradient; $G_{pij} = \partial^2 \delta y_p / \partial \delta x_i \delta x_j$ and $H_{pijk} = \partial^3 \delta y_p / \partial \delta x_i \delta x_j \delta x_k$ are the second-order and third-order derivative, respectively.

Substitute (4.13) into (4.12), the deformation gradient then turns into

$$\begin{aligned} F_{pq} = F_{pq} &+ \frac{1}{2! h^2 \Omega} G_{pij} \sum_{a=1}^{N} \omega_a (\delta x_i \delta x_j \delta x_q)_a \\ &+ \frac{1}{3! h^2 \Omega} H_{pijk} \sum_{a=1}^{N} \omega_a (\delta x_i \delta x_j \delta x_k \delta x_q)_a + O(h^3). \end{aligned} \tag{4.14}$$

It is possible to achieve higher-order approximation by selecting explicit weight functions in (4.14). Note that for a symmetric and intact horizon, a bond $(\delta\mathbf{x})_m$ always companies with another bond $(\delta\mathbf{x})_n$ symmetry about the origin, i.e., $(\delta\mathbf{x})_m = -(\delta\mathbf{x})_n$. Therefore,

$$\sum_{a=1}^{N} \omega_a (\delta x_i \delta x_j \dots \delta x_m)_a = 0, \text{ if there are odd } \delta x\text{-products.} \tag{4.15}$$

As odd δx-product summation vanishes, symmetric particle patterns with intact horizons will always lead to accuracy order equal or greater than $O(h^2)$. One additional

equation need to be satisfied to achieve $O(h^4)$:

$$A_{ijkl} = \sum_{a=1}^{N} \omega_a (\delta x_i \delta x_j \delta x_k \delta x_l)_a = 0. \tag{4.16}$$

Furthermore, the following two equations will lead to accuracy order of $O(h^6)$:

$$\begin{cases} A_{ijkl} = \sum_{a=1}^{N} \omega_a (\delta x_i \delta x_j \delta x_k \delta x_l)_a = 0 \\ B_{ijklrs} = \sum_{a=1}^{N} \omega_a (\delta x_i \delta x_j \delta x_k \delta x_l \delta x_r \delta x_s)_a = 0 \end{cases} . \tag{4.17}$$

Criteria (4.16) and (4.17) hold true for all dimensions. It is evident that larger horizons, which have more independent weight function values, can bring higher order of leading error. Nevertheless, it is unaware of the total number of equations in (4.16) and (4.17). In addition, the final selected weight function values should satisfy $\Omega(\omega_1, \omega_2, \omega_3, ...) \neq 0$ to ensure the shape tensor $\mathbf{K}$ in (4.11) is invertible. The following is a brief discussion on the number of non-trivial components in the fourth tensor A_{ijkl}.

First of all, subscript indices can be swapped:

$$A_{ijkl} = A_{jikl} = A_{ijlk}. \tag{4.18}$$

Assume we have a 2D quadrilateral particle pattern where subscript indices take on values 1 and 2. Due to (4.18) only six components are independent, which are $A_{1111}, A_{2111}, A_{2211}, A_{2221}$, and A_{2222}.

Secondly, the coordinate index 1 and 2 can be swapped as well. This is because of the axis symmetry of the horizon and particle pattern. For example,

$$A_{1111} = A_{2222}, \text{ and } A_{2111} = A_{1112}. \tag{4.19}$$

Thirdly, assume that there is a bond (x, y) with a weight function ω_1 in the horizon.

Owing to the symmetry of coordinate axes, three other bonds $(-x, y)$, $(-x, -y)$, and $(x, -y)$ are supposed to be in the horizon as well. Hence, based on the definition in (4.16),

$$A_{2221} = \omega_1 y^2(xy - xy + xy - xy) = 0. \tag{4.20}$$

Eventually, only two components of the fourth-order tensor A_{ijkl} are non-zero, which are A_{1111} and A_{2211}.

For the sake of simplicity and unity, the weight function value which is located closest to the center particle is set to be 1, i.e., $\omega_1 = 1$. In order to achieve $O(h^4)$, we need two more independent weight function values, ω_2 and ω_3. Therefore, the horizon with radius $\delta = 2h$ in Fig 4.6 is the smallest one that can achieve $O(h^4)$ in the 2D quadrilateral pattern.

In terms of horizons with excess independent weight functions but not enough to achieve higher order of errors, the weight function values are not unique. These horizon selections could possibly bring noise or numerical oscillations in the ultimate solutions. Typically, weight function values decrease from the closest particles to distant particles and the value on the farthest particle should not be zero.

For 2D quadrilateral patterns, our study is limited to horizon size $\delta \leq 3h$. Fig. 4.6 illustrates all possible distributions of neighboring particles with different horizon sizes. Only a quarter of horizon is plotted due to the symmetry of ω. Table 4.2 shows the weight function values to achieve corresponding higher accuracy.

For 3D cubic patterns, the horizon size is limited to $\delta \leq 2h$, where h is the spacing between nearest particles. Fig. 4.7 illustrates all possible distributions of neighboring particles with different horizon spheres. Similar to 2D patterns, only a quarter of sphere is plotted due to the symmetry of ω. Table 4.3 shows the weight function values to achieve corresponding higher accuracy. Note that the selected weight function values of the horizon size $\delta = \sqrt{2}h$ lead a zero shape tensor K, thus not recommended in 3D computation.

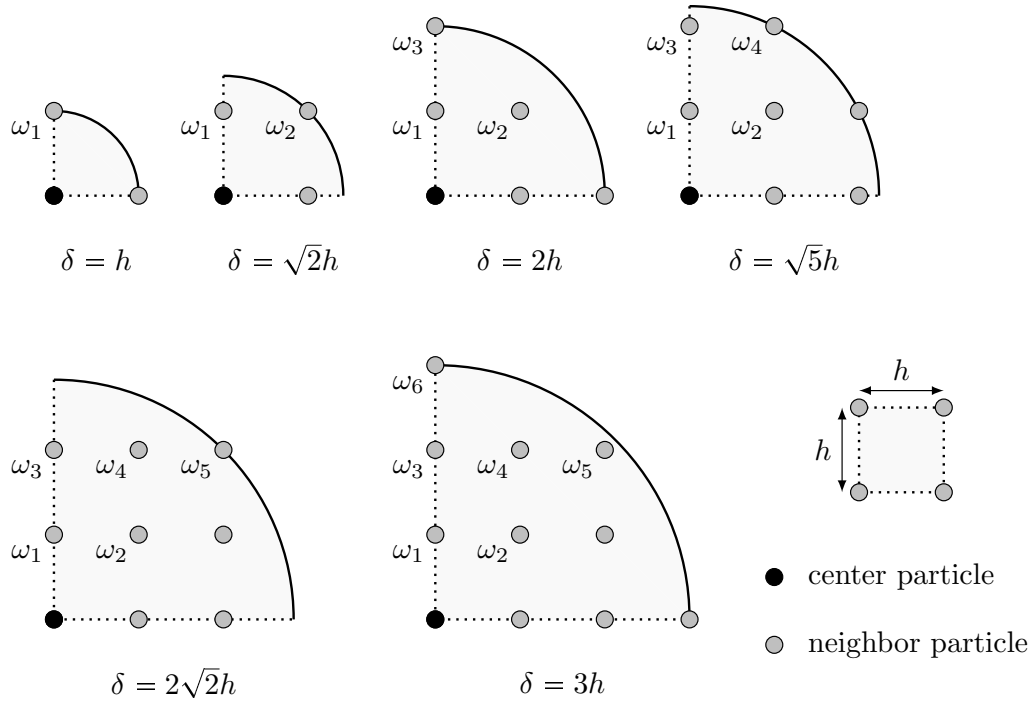

Figure 4.6: *All possible 2D horizon shapes with a quadrilateral particle discretization under $\delta \leq 3h$. Because the weight function ω is spherically symmetric, only a quarter of circle is plotted for each horizon shape.*

Table 4.2: *Higher-order approximation weight functions 2D particle discretization with a constant spacing h. For horizons δ^*, weight function values are not unique.*

Horizon size	Weight function values						Error
	ω_1	ω_2	ω_3	ω_4	ω_5	ω_6	
$\delta = h$	1	0	0	0	0	0	$O(h^2)$
$\delta^* = \sqrt{2}h$	1	1	0	0	0	0	$O(h^2)$
$\delta = 2h$	1	0	-1/16	0	0	0	$O(h^4)$
$\delta^* = \sqrt{5}h$	1	-8/46	-4/46	1/46	0	0	$O(h^4)$
$\delta = 2\sqrt{2}h$	1	-2/3	-1/4	1/6	-1/24	0	$O(h^6)$
$\delta^* = 3h$	1	4/9	0	-1/9	1/36	1/81	$O(h^6)$

4.4 Boundary Treatment

Conventional constraint conditions, such as Dirichlet and Neumann boundary conditions, are supposed to be imposed in a different form, as the PD governing

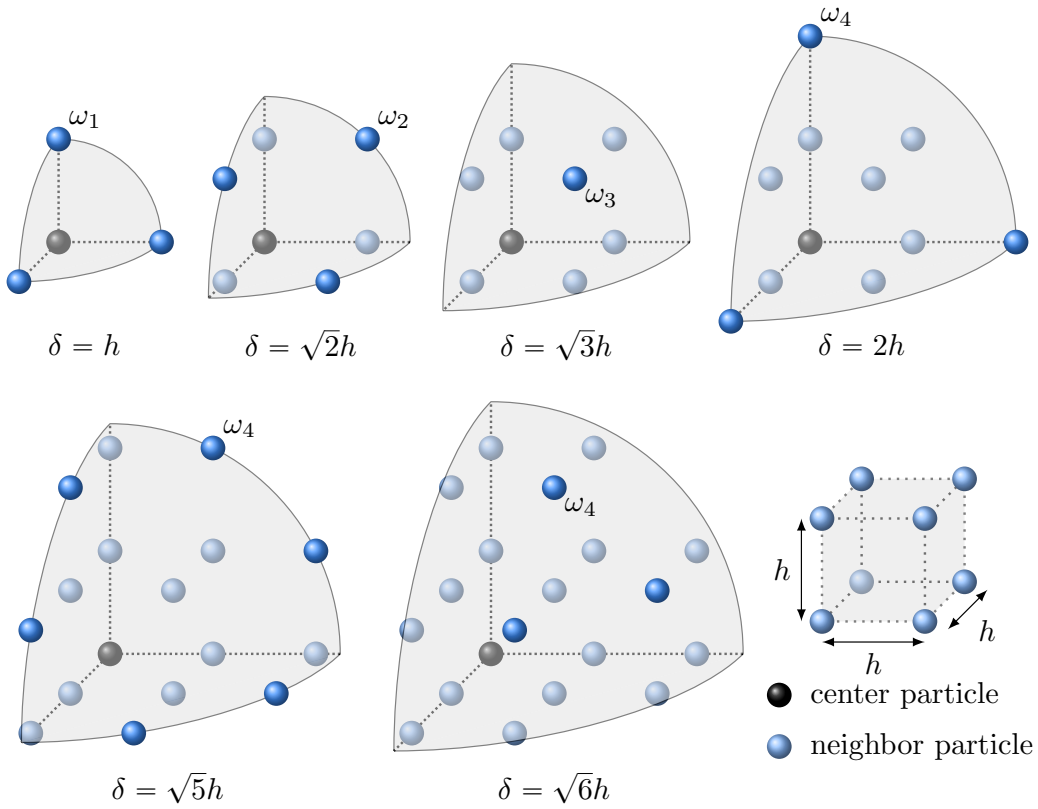

Figure 4.7: *All possible 3D horizon shapes with a cubic particle discretization under $\delta \leq 2h$. Because the weight function ω is spherically symmetric, only one eighth of the sphere is plotted for each horizon shape.*

Table 4.3: *Higher-order approximation weight functions 3D particle discretization with a constant spacing h. For horizons δ^*, weight function values are not unique. Note that weight functions of horizon $\delta = \sqrt{3}h$ results in a zero shape tensor.*

Horizon size	Weight function values						Error
	ω_1	ω_2	ω_3	ω_4	ω_5	ω_6	
$\delta = h$	1	0	0	0	0	0	$O(h^2)$
$\delta^* = \sqrt{2}h$	1	1	0	0	0	0	$O(h^2)$
$\delta = \sqrt{3}h$	1	-1/2	1/4	0	0	0	$O(h^4)$
$\delta^* = 2h$	1	-1/3	1/6	-1/48	0	0	$O(h^4)$
$\delta^* = \sqrt{5}h$	1	-47/136	43/272	-1/32	1/272	0	$O(h^4)$
$\delta = \sqrt{6}h$	1	-11/20	3/10	-1/10	1/20	-1/40	$O(h^6)$

equations are written in nonlocal formulation. In the previous chapter, no special boundary treatment is conducted because we only consider the nearest-particle family. Defect horizons with the smallest horizon can still correctly approximate the deformation gradient at boundary. However, as the horizon size increases, irregular defect horizons ultimately lead to disordered and unstable solutions around boundary particles. Since higher-order approximations are derived from internal particles with a fully symmetric horizon and spherically-symmetric influence function ω, another raised concern is that defect horizons at boundary would bring errors in approximating the deformation gradient.

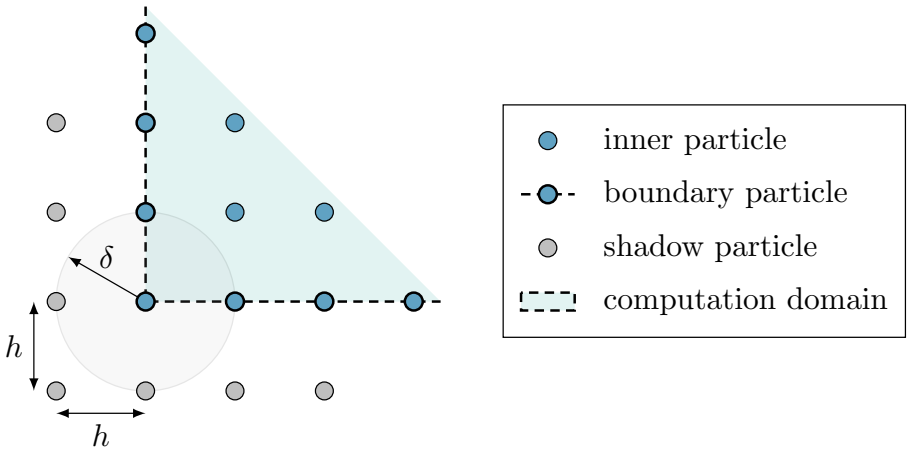

Figure 4.8: *Boundary region with shadow particles. The thickness of the shadow-particle layer is equal to the horizon size δ. A horizon of $\delta = h$ is illustrated in this plot, where h is the particle spacing.*

One possible solution, suggested by Macek and Silling [113, 15], is to apply a "fictitious material layer" along the boundary. The thickness or depth of the fictitious boundary layer should be equal to the horizon size δ to ascertain that prescribed constraints are sufficiently forced on the real material region. Same discretization is supposed to be applied in both the fictitious boundary layer and real material domain. Shadow particles are therefore introduced in the fictitious layer, as shown in Fig. 4.8.

4.4.1 Displacement constraints

Displacement constraints are commonly used in our numerical examples. Considering no information is provided outside the real material region, Madenci [15] suggested that the prescribed displacement vector should be the same as that of the closest material particle at boundary. However, this operation results in zero strain and stress in the fictitious boundary layer.

When it comes to polycrystal simulations, we apply a constant deformation gradient at boundary, as illustrated in Chapter 3.2. Hence, we are able to prescribe displacements on shadow particles based on this constant deformation gradient. Moreover, stress at shadow particles can be calculated by the correspondence constitutive $\sigma(\mathbf{F})$. These stress terms are then utilized in the equation of motion at boundary particles. Note that boundary particles are given only displacement information.

In a summary, we assume all information on shadow particles are known, i.e., both displacement and stress, in contrast with boundary particles, where only displacement is given. Our results have shown that this special boundary enforcement is particularly effective in large-horizon PD families.

4.4.2 Forces and traction

External loading conditions can be treated as an equivalent body force density in the peridynamic governing equation (2.17). Different from the displacement constraints, the thickness of the fictitious boundary layer for external loadings is supposed to be greater. Details can be found in [15].

4.5 1D Numerical Example

A 1D elastic bar test is conducted, as shown in Fig. 6.4. The bar has a total length L_{tot} and a constant cross-sectional area A. Displacement constraints, $u_1 = 0$

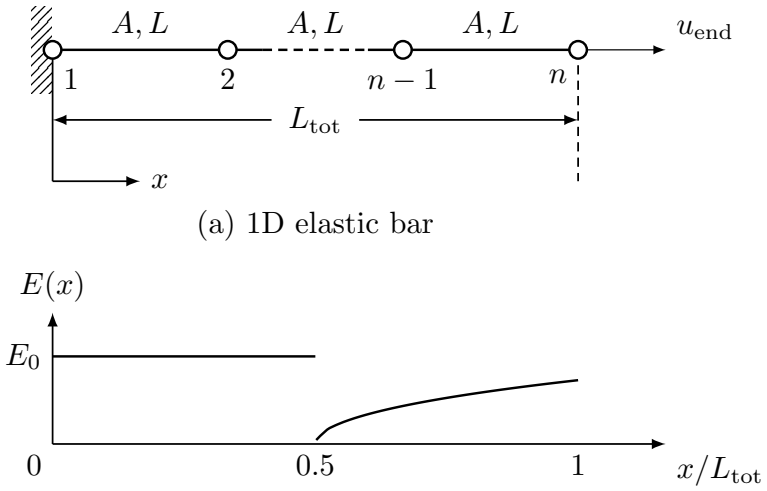

(a) 1D elastic bar

(b) Young's Mudulus along x

Figure 4.9: *A 1D elastic bar under tension with a Young's modulus varied along the x axis.*

and $u_n = u_{end}$, are applied on the two sides of the bar. A variable Young's modulus is adopted as

$$E(x) = \begin{cases} E_0 & 0 \le x \le L_{\text{tot}}/2 \\ E_0\Big(1 + \frac{\beta}{2\alpha}\frac{1}{\sqrt{x/L_{\text{tot}} - 1/2}}\Big)^{-1} & L_{\text{tot}}/2 < x \le L_{\text{tot}} \end{cases}, \tag{4.21}$$

and the analytical displacement $u(x)$ is

$$u(x) = \begin{cases} \alpha x & 0 \le x \le L_{\text{tot}}/2 \\ \alpha x + \beta L_{\text{tot}}\sqrt{x/L_{\text{tot}} - 1/2} & L_{\text{tot}}/2 < x \le L_{\text{tot}} \end{cases}, \tag{4.22}$$

where parameters are selected as $L_{\text{tot}} = 1$, $E_0 = 1$, $u_{\text{end}} = 0.005$, $\alpha = 0.001$, and $\beta = 0.004\sqrt{2}$.

A comparison between the higher-order approximation solutions and those with no control method is shown in Fig. 6.7. Since higher-order approximation approach only takes effect in large-horizon families, we provide tow horizon selections, i.e., $\delta = 2h$

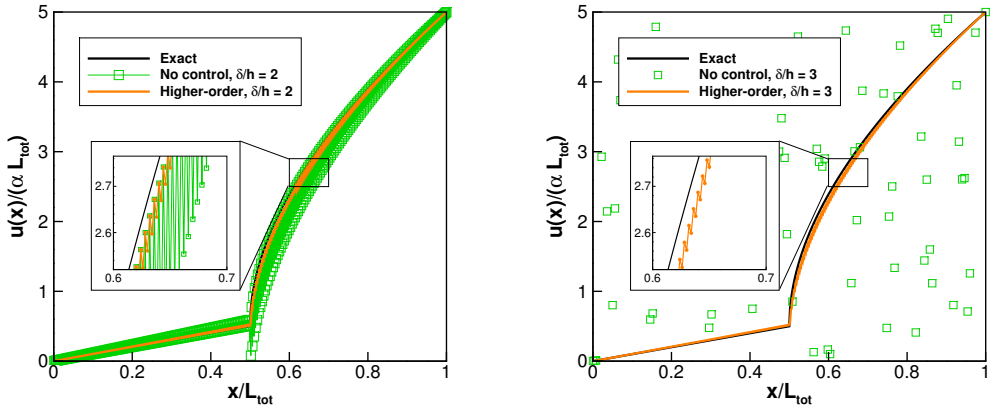

(a) $\delta = 2h$ (b) $\delta = 3h$

Figure 4.10: *Effect of zero-energy modes on the displacement field of 1D bar obtained from the higher-order approximation approach with two different horizon sizes. Results are based on a mesh with 500 particles.*

and $\delta = 3h$. As the horizon size increases, the oscillations grow dramatically if no control method is applied. Higher-order approximation method effectively suppress the oscillations in both cases, though not completely remove the zero-energy modes.

4.6 2D Numerical Example

Reconsider the plane polycrystal in Chapter III Section 3.2. A compression velocity gradient is applied on microstructure boundaries. Our boundary treatment is shown in Fig 4.11.

An inward fictitious boundary layer is selected because we are not aware of the crystal information outside the original boundary. As the fictitious layer becomes thicker, the computation domain shrinks. Fig. 4.12 provides an example showing the effect of this boundary treatment. Low-valued stress is observed around boundary without the fictitious boundary layer. This is mainly because of the erroneous deformation gradient approximated by defect horizons. In contrast, the stress field obtained from the boundary enforcement is normal with no spurious values along the

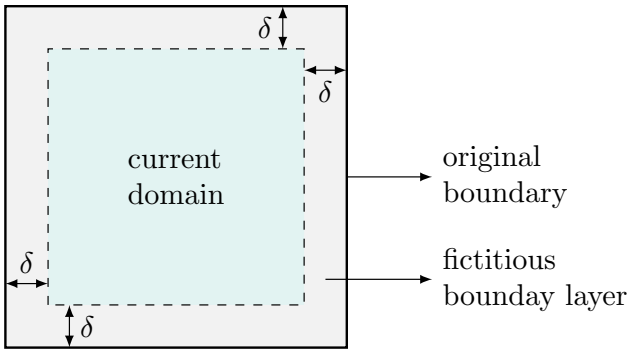

Figure 4.11: *Boundary treatment on plane polycrystals. The fictitious boundary layer is inward possessing thickness equal to the horizon radius δ .*

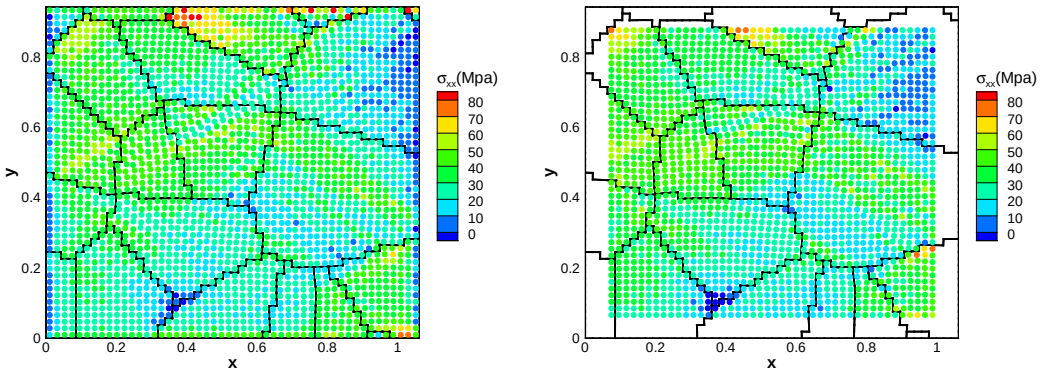

(a) no boundary treatment

(b) boundary enforcement

Figure 4.12: *The effect of boundary treatment on CPPD stress distributions with a horizon size $\delta = 3h$.*

four sides.

Following is a Y-axis compression test based on the same microstructure in Chapter III Section 3.2.2. Fig 4.13 provides a comparison of crystal orientation changes with three different horizon selections. We choose three smallest horizon sizes in Table 4.2 that leads to high order of error.

It is clear from the figure above that zero-energy modes are effectively suppressed in all three horizon selections. This is the same as what we found in the 1D elastic bar tension test seen previously, where we have compared the higher-order approach with the problem with no control. Moreover, larger horizons usually bring more accurate

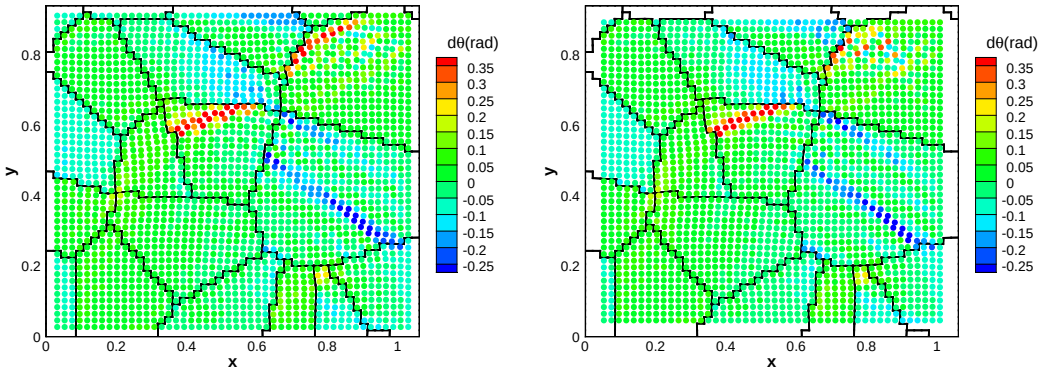

(a) $\delta = h$, $O(h^2)$

(b) $\delta = 2h$, $O(h^4)$

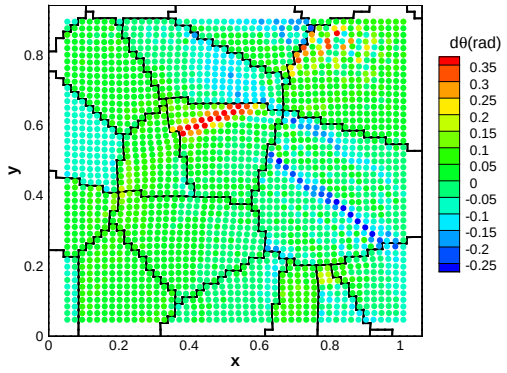

(c) $\delta = 2\sqrt{2}h$, $O(h^6)$

Figure 4.13: *Orientation changes for 2500 particles under a y-axis compression test with three different horizon sizes. δ is the horizon radius and h is the distance between nearest particles. The margin around the boundary is due to the boundary treatment.*

solutions, as the shear bands become sharper and more concentrated.

However, if two horizon selections have the same order of accuracy, the larger horizon will bring more zero-energy-mode oscillations instead. Fig. 4.14 shows a set of local amplifications of orientation changes in six selected horizon sizes. We choose a small window to capture the center crystal and the shear band in red in Fig. 4.13. We can observe that results on the right group have more oscillations of particles, whereas they have the same order of accuracy with those on the left. In other words,

by including more neighbor particles will not lead to more stable results if they are not able to achieve higher order of accuracy. The solution highly depends on the weight function values, whereas their values are not unique. This is different from the 1D bar test, in which larger horizons will definitely reduce zero-energy modes.

4.7 Conclusions

A higher-order approximation to the nonlocal deformation gradient is proposed to suppress zero-energy modes. CPPD Solutions are not effected by the horizon size in the same accuracy order. In addition, no additional computation cost is needed because only the influence functions is adjusted in the computation. Next chapter will extend the CPPD-ADRS model in 3D polycrystal simulations.

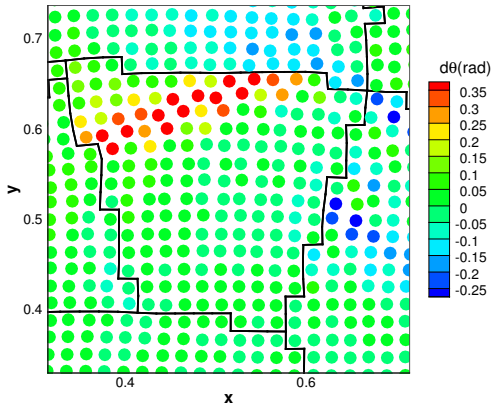

(a) $\delta = h$, $O(h^2)$

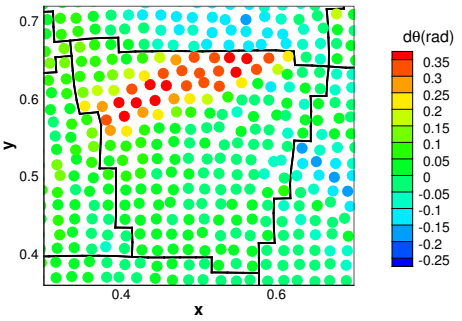

(b) $\delta = \sqrt{2}h$, $O(h^2)$

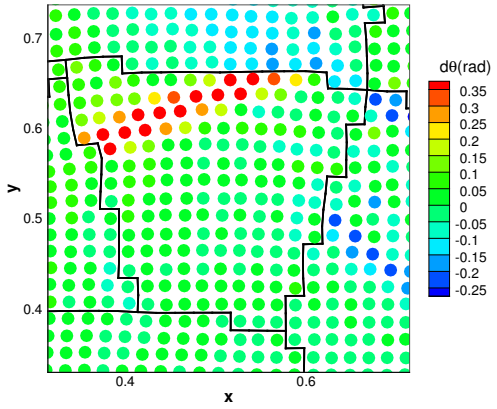

(c) $\delta = 2h$, $O(h^4)$

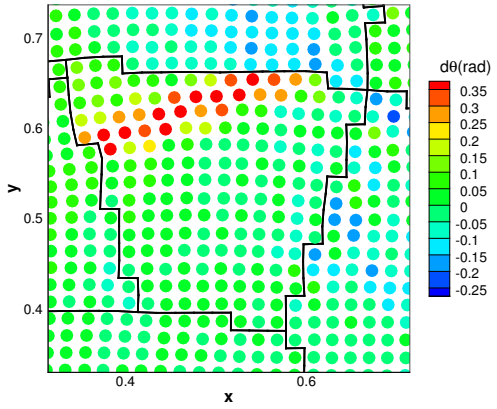

(d) $\delta = \sqrt{5}h$, $O(h^4)$

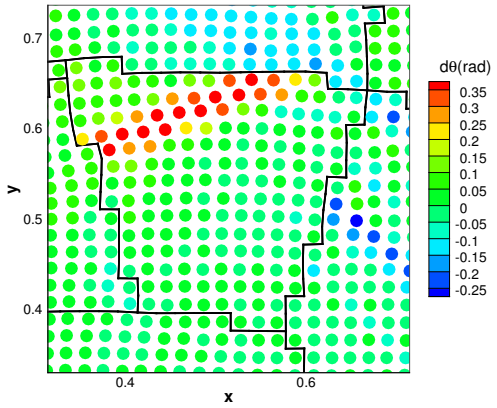

(e) $\delta = 2\sqrt{2}h$, $O(h^6)$

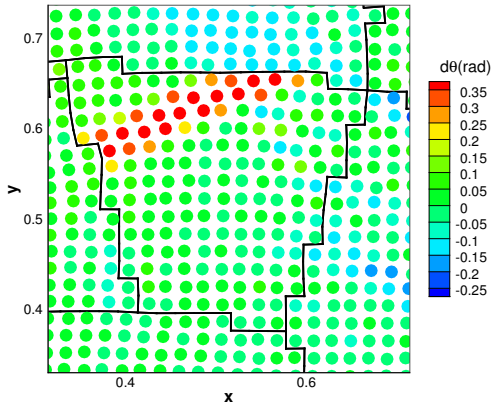

(f) $\delta = 3h$, $O(h^6)$

Figure 4.14: *Local view of orientation changes with six different horizon sizes. δ is the horizon radius and h is the distance between nearest particles.*

CHAPTER V

3D PD-ADRS Implementation with Crystal Plasticity

We propose the extension of peridynamics theory for modeling 3D polycrystals with both slip and twin activities. A 3D parallel CPPD formulation is developed in this chapter. Rate-independent crystal plasticity from previous chapter was implemented for 3D slip systems. The next section provides the validation of the code via measured crystal orientation evolution and final textures. This section presents comparisons with published data [114] under plane stress and z-rotation, respectively.

5.1 Crystal Orientations and Textures

The orientation of a crystal is the rotation needed to align a set of axes fixed to its lattice in a reference frame. We utilize the Rodrigues space to represent the crystal orientation [115, 116, 117, 118**?**], in which a rotation can be defined by its axis, $\mathbf{n}$, and angle of rotation about that axis, ϕ. The general form of the four-dimensional quaternion parameterization is

$$\mathbf{r} = \mathbf{r}(\phi, \mathbf{n}) = \tan(\phi/2)\mathbf{n}, \tag{5.1}$$

where $\mathbf{r}$ is a vector in the Rodrigues orientation space. The orientation can be alternatively expressed as a rotation matrix $\mathbf{R}$:

$$\mathbf{R}(\phi\mathbf{n}) = \mathbf{n} \otimes \mathbf{n} + \cos\phi(\mathbf{I} - \mathbf{n} \otimes \mathbf{n}) + \sin\phi(\mathbf{I} \times \mathbf{n}), \tag{5.2}$$

where $\mathbf{I}$ is the identity matrix.

Due to crystal symmetries, there exist a smallest subset that uniquely specify all possible orientations, which is called the fundamental region $\mathcal{R}$. Provided with values of ϕ^i and $\mathbf{n}^i$ associated with the symmetry operation i, a bounding plane for the fundamental region can be obtained by

$$\pm\,\mathbf{r} \cdot \mathbf{n}^i \leq \tan(\phi^i/4). \tag{5.3}$$

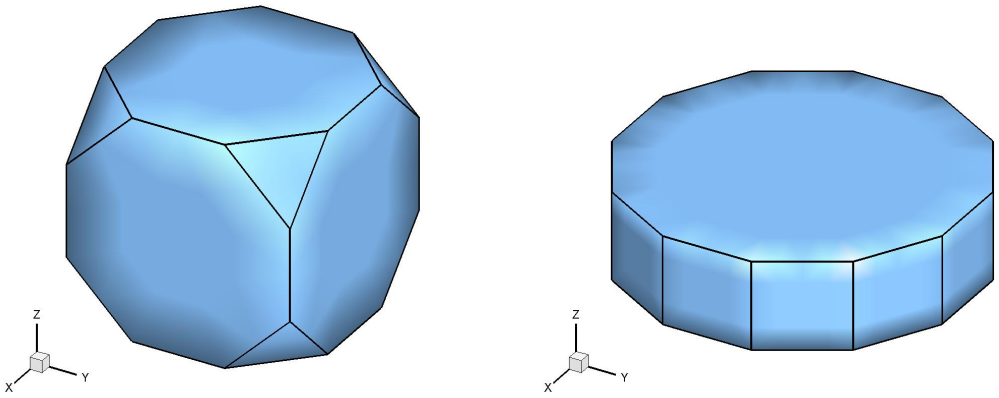

(a) FCC (b) HCP

Figure 5.1: *Fundamental regions for FCC and HCP crystals using Rodrigues parameterization.*

The fundamental regions for FCC and HCP crystals are depicted in Fig. 5.1 [119, 120]. Within the fundamental region, crystal textures can be described by the orientation distribution function (ODF), $\mathcal{A}(\mathbf{r})$, which describes the volume density of the crystal orientation $\mathbf{r}$. The ODF is normalized to unity over the fundamental

region as

$$\int_{\mathcal{R}} \mathcal{A}(\mathbf{r})dv = \sum_{n=1}^{N_{\text{elem}}} \sum_{m=1}^{N_{\text{int}}} A(\mathbf{r}_m)\omega_m |J_n| \frac{1}{(1+\mathbf{r}_m \cdot \mathbf{r}_m)^2} = 1, \tag{5.4}$$

where $A(\mathbf{r}_m)$ is the ODF value at the m^{th} integration point of the n^{th} element with the orientation coordinate $\mathbf{r}_m$; $|J_n|$ is the Jacobian determinant of the n^{th} element; ω_m is the integration weight associated with the m^{th} integration point. As shown in Fig. 5.2, the fundamental region is discretized into N independent nodes with N_{elem} tetrahedron finite elements and N_{int} integration points per element.

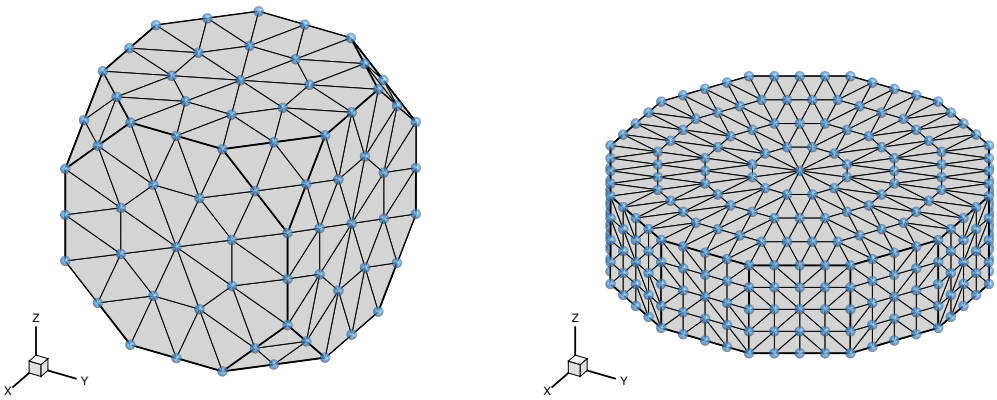

(a) FCC (b) HCP

Figure 5.2: *The Fundamental regions for FCC and HCP crystals are discretized into finite elements. Only nodes in the blue color on boundaries are independent nodes of the ODF considering the crystal symmetry using the Rodrigues parameterization.*

Only one integration point per element at the local coordinate of (0.25, 0.25, 0.25) is applied in calculating the integration in (5.4). The integration weight function is thus $\omega = 1/6$. Equation (5.4) is then simplified as

$$\mathbf{q}^{\mathrm{T}} \cdot \mathbf{A} = 1 \tag{5.5}$$

where $q_i = \frac{1}{6}|J_i| \frac{1}{(1+\mathbf{r}_i \cdot \mathbf{r}_i)^2}$ and $A_i = A(r_i)$ with $i = 1, \ldots, N_{\text{elem}}$. Crystallographic symmetry is enforced by considering the set of independent nodal points instead of

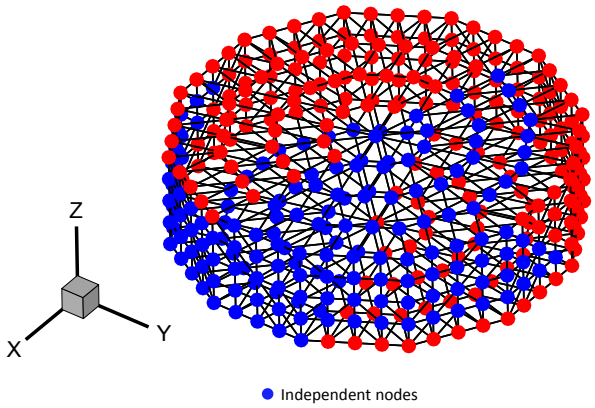

Figure 5.3: *ODF representation in the Rodrigues fundamental region for hexagonal crystal symmetry showing the location of the k=388 independent nodes of the ODF in blue color.*

the integration points [121, 122]. Independent nodal points are in a reduced set of nodes accounting for symmetry conditions at the boundaries of the fundamental region (see Fig. 5.2). Let matrix **H** be the conversion matrix between the independent nodal values and the integration point values, which can be expressed as

$$\mathrm{A}^{\mathrm{int}} = \mathbf{H}\mathrm{A}^{\mathrm{node}}, \tag{5.6}$$

where $\mathrm{A}^{\mathrm{int}}$ and $\mathrm{A}^{\mathrm{node}}$ refer to the ODF values at the integration points and element nodes, respectively. Regarding to tetrahedron elements, (5.6) can be simplified as

$$\mathrm{A}_{\mathrm{e}}^{\mathrm{int}} = \frac{1}{4}\sum_{i=1}^{4}\mathrm{A}_{e}^{i}, \tag{5.7}$$

where i is the node number from 1 to 4 for a tetrahedron element e. As a result, (5.5) turns into

$$\mathbf{q}^{\mathrm{T}} \cdot (\mathrm{H}\mathbf{A}^{\mathrm{node}}) = (\mathrm{H}^{\mathrm{T}}\mathbf{q})^{\mathrm{T}} \cdot \mathbf{A}^{\mathrm{node}} = 1, \tag{5.8}$$

so that normalization can be represented as the scalar product with the ODF values

at the independent nodal points.

The orientations from the peridynamics data are binned point-by-point to the element containing the orientation, specifically to the integration point in the element. After binning is complete, the ODF value (A_i^{int}) at the integration point in an element i contains the total number of points in the peridynamics image that have orientations lying within the element. The data is then normalized by $q^{int^T} A^{int}$. We use matrix T to convert the integration point values A^{int} to the independent nodal values A^{node}, ie., $A^{node} = TA^{int}$. Using one integration point, this matrix is defined as $T_{ij} = \delta_{ij}/f$ where δ_{ij} is one if node i (or its symmetric equivalent) is a vertex of element j and zero otherwise. The factor f is the number of elements with node i (or symmetric equivalent) as one of its vertices. This matrix is always positive and thus, $A^{node} \geq 0$.

5.2 Polycrystal Texture under Two Deformation Modes

The microstructure considered in this section is a 3D polycrystal cube with a dimension of $3 \times 3 \times 3$ mm^3. The cube is discretized into particles owning a constant particle distance h. We start the test with 24 particles in each direction, therefore, totally 13824 particles in the computation domain. Every particle is assigned with a unique orientation vector, which makes the initial texture fully random. The initial textures that we choose for FCC and HCP crystals are shown in Fig. 5.4.

We test the PD-ADRS code in two deformation modes, which are plane strain compression and uniaxial compression. Both deformation modes allow large strain considering small stability limits and suppressed failure mechanisms [114]. Similar to the 2D numerical polycrystal examples in Chapter 3.2, velocity gradients are applied on the boundary. For the plane strain compression deformation mode, the velocity

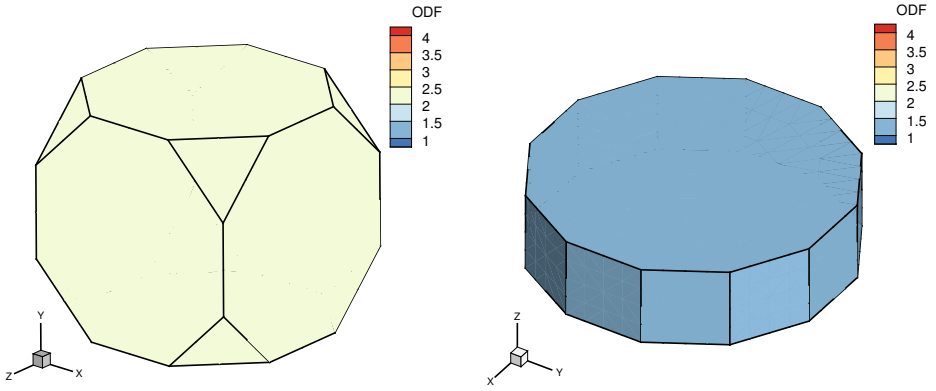

(a) FCC (b) HCP

Figure 5.4: *Initial textures of the 3D (a) FCC and (b) HCP polycrystal cubes plotted in the fundamental region.*

gradient $\mathbf{L}^{\mathrm{p}}$ is given by

$$\mathbf{L}^{\mathrm{p}} = L_0 \begin{bmatrix} 1.0 & 0.0 & 0.0 \\ & 0.0 & 0.0 \\ \text{sym.} & & -1.0 \end{bmatrix} \mathrm{s}^{-1}, \tag{5.9}$$

where $L_0 = 0.001$ is a constant strain rate. Likewise, the uniaxial compression velocity gradient is

$$\mathbf{L}^{\mathrm{u}} = L_0 \begin{bmatrix} 0.5 & 0.0 & 0.0 \\ & 0.5 & 0.0 \\ \text{sym.} & & -1.0 \end{bmatrix} \mathrm{s}^{-1}. \tag{5.10}$$

The material we choose for the FCC crystal is copper [123]. The elastic constants and hardening coefficients for the crystal plasticity model are given in Tables 5.1 and 5.2. Its twelve slip systems are listed in Table 5.3. All slip systems share the same slip constants.

Considering next sections will be focused on HCP magnesium alloys, we only conduct the plane strain compression test on the FCC copper crystal. Similar texture have been captured in the FCC crystal with the PD-ADRS compared with the results

Table 5.1: *Elastic constants (Unit: GPa) of single-crystal FCC copper [1].*

C_{11}	C_{12}	C_{44}
170.0	124.0	75.0

Table 5.2: *Slip resistance and hardening coefficients used in FCC copper [1].*

s_0 (MPa)	h_0 (MPa)	s_s (MPa)	a
16.0	180.0	148.0	2.25

Table 5.3: *FCC copper slip systems [1].*

ID	Direction	Normal	ID	Direction	Normal
1	[1 1 0]	(1 1 1)	7	[-1 0 1]	(1 -1 1)
2	[-1 0 1]	(1 1 1)	8	[0 -1 -1]	(1 -1 1)
3	[0 1 -1]	(1 1 1)	9	[1 1 0]	(1 -1 1)
4	[1 0 1]	(-1 1 1)	10	[-1 1 0]	(-1 -1 1)
5	[-1 -1 0]	(-1 1 1)	11	[1 0 1]	(-1 -1 1)
6	[0 1 -1]	(-1 1 1)	12	[0 -1 -1]	(-1 -1 1)

obtained from FEM, as shown in Fig. 5.5.

Following tests and examples are all for HCP crystals. A magnesium alloy is selected to be the HCP crystal sample, as its elastic constants given in Table 5.4. We employ 18 slip systems in plastic deformation of magnesium, which include basal$< a >$, prismatic$< a >$, pyramidal$< a >$, and pyramidal$< c+a >$ slip systems. No twinning system is considered in this texture test. The particular crystal hardening law is the same with the power law in the 2D polysrystal test, see Section 3.2 Chapter III. The following Tables 5.5 and 5.6 state the slip systems and hardening coefficients used in the HCP texture test, respectively.

Table 5.4: *Elastic constants (Unit: GPa) of single-crystal HCP Magnesium alloys [2].*

C_{11}	C_{12}	C_{13}	C_{33}	C_{44}
59.3	25.7	21.4	61.5	16.4

Simulation is then performed over 200 loading steps with a constant strain rate

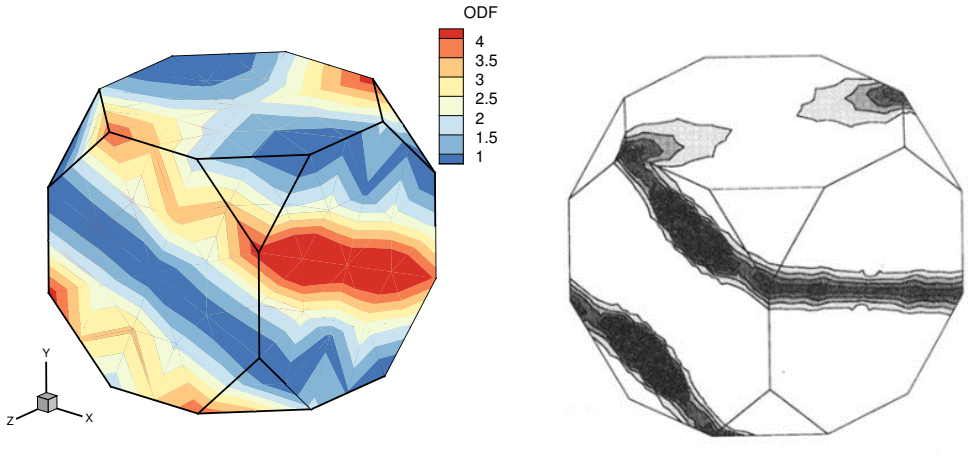

(a) PD (b) FEM

Figure 5.5: *Plane strain compression texture of the 3D FCC polycrystal cube based on (a) PD-ADRS and (b) FEM from [124].*

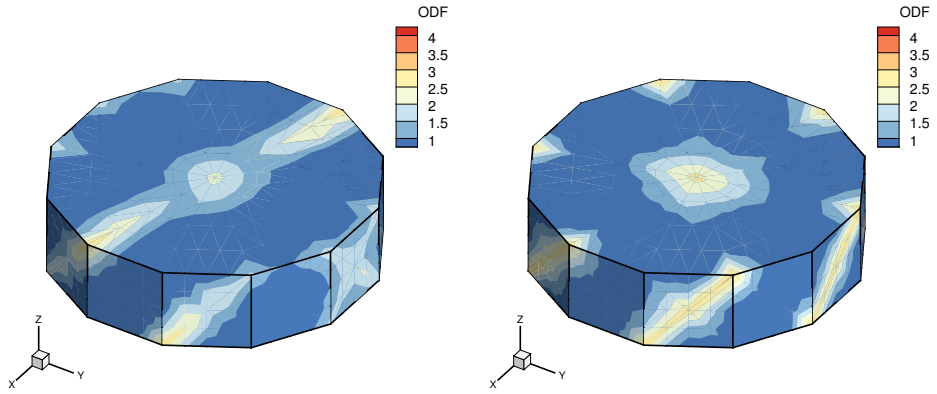

(a) Plane strain compression (b) Uniaxial compression

Figure 5.6: *3D view of the texture of the 3D HCP polycrystal cube under (a) plane strain compression and (b) uniaxial compression.*

$L_0 = 0.001$, which results in a final strain around 0.2. Two modes of deformation, plane strain compression and uniaxial compression, are applied separately with the velocity gradients $\mathbf{L}^{\mathrm{p}}$ and $\mathbf{L}^{\mathrm{u}}$ on the boundary, respectively. In order to compare with the texture computed by FEM from [114], we first present the 3D views of the textures in Fig. 5.6, and then apply the cutting planes to check the interior part of the fundamental region. Same cutting planes on the fundamental region are selected with FEM and results are shown in Figs. 5.7 and 5.8. Note that all PD results in the

Table 5.5: *HCP magnesium slip systems [3].*

Slip System	ID	Direction	Normal
Basal$< a >$	1	[1 1 -2 0]	(0 0 0 1)
	2	[-2 1 1 0]	(0 0 0 1)
	3	[1 -2 1 0]	(0 0 0 1)
Prism$< a >$	4	[1 -2 1 0]	(1 0 -1 0)
	5	[2 -1 -1 0]	(0 1 -1 0)
	6	[1 1 -2 0]	(-1 1 0 0)
Pyram$< a >$	7	[1 -2 1 0]	(1 0 -1 1)
	8	[-2 1 1 0]	(0 1 -1 1)
	9	[-1 -1 2 0]	(-1 1 0 1)
	10	[-1 2 -1 0]	(-1 0 1 1)
	11	[2 -1 -1 0]	(0 -1 1 1)
	12	[1 1 -2 0]	(1 -1 0 1)
Pyram$< c + a >$	13	[-1 -1 2 3]	(1 1 -2 2)
	14	[1 -2 1 3]	(-1 2 -1 2)
	15	[2 -1 -1 3]	(-2 1 1 2)
	16	[1 1 -2 3]	(-1 -1 2 2)
	17	[-1 2 -1 3]	(1 -2 1 2)
	18	[-2 1 1 3]	(2 -1 -1 2)
Twin$< c + a >$	19	[-1 0 1 1]	(1 0 -1 2)
	20	[1 0 -1 1]	(-1 0 1 2)
	21	[-1 1 0 1]	(1 -1 0 2)
	22	[1 -1 0 1]	(-1 1 0 2)
	23	[0 -1 1 1 1]	(0 1 -1 2)
	24	[0 1 -1 1]	(0 -1 1 2)

Table 5.6: *Slip constants used in HCP magnesium alloys [1].*

Slip System	s_0 (MPa)	h_0 (MPa)	s_s (MPa)	a
Basal$< a >$	76.0	225.6	248.7	1.0
Prism$< a >$	163.2	124.9	356.3	1.0
Pyram$< a >$	160.3	120.2	347.8	1.0
Pyram$< c + a >$	187.4	237.9	350.4	1.0
Twin$< c + a >$	116.4	105.6	238.3	1.0

texture test is based on a horizon size only included the nearest particles. Smallest-horizon PD family can produce local results to better compare with the FEM.

FEM textures exhibit more smooth and symmetric texture, while PD results show

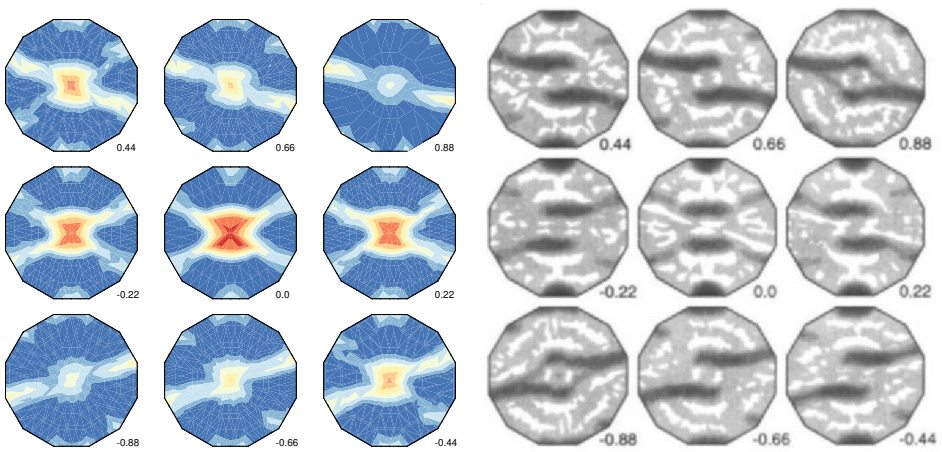

(a) PD (b) FEM

Figure 5.7: *Plane strain compression texture of the 3D HCP polycrystal cube based on (a) PD and (b) FEM [114]. The number to the right corner of each plane indicates the relative position compared to the maximum z-coordinate value in the fundamental region.*

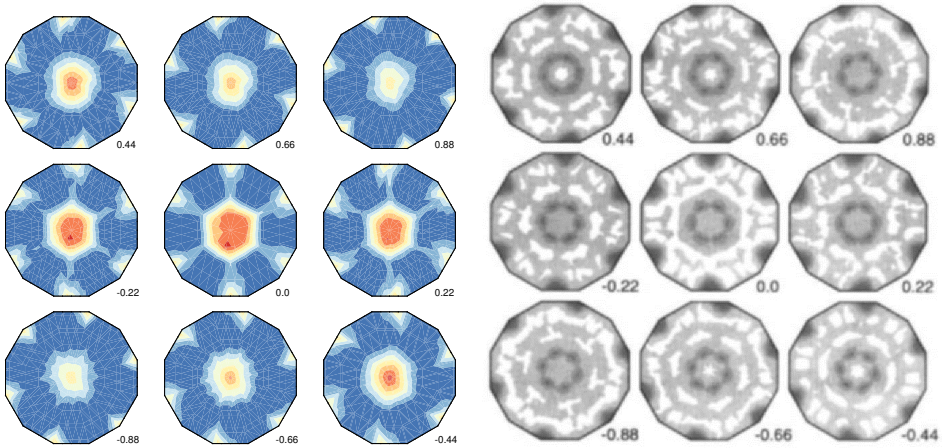

(a) PD (b) FEM

Figure 5.8: *Uniaxial compression texture of the 3D HCP polycrystal cube based on (a) PD and (b) FEM [114]. The number to the right corner of each plane indicates the relative position compared to the maximum z-coordinate value in the fundamental region.*

more numerical oscillations due to the explicit dynamic solver. The overall textures are similar under both deformation modes, which indicate the 3D PD-ADRS codes work for capturing the texture of both FCC and HCP crystals.

Next, we select a 3D polycrystal cube with 78 grains, shown in Fig. 5.9, to in-

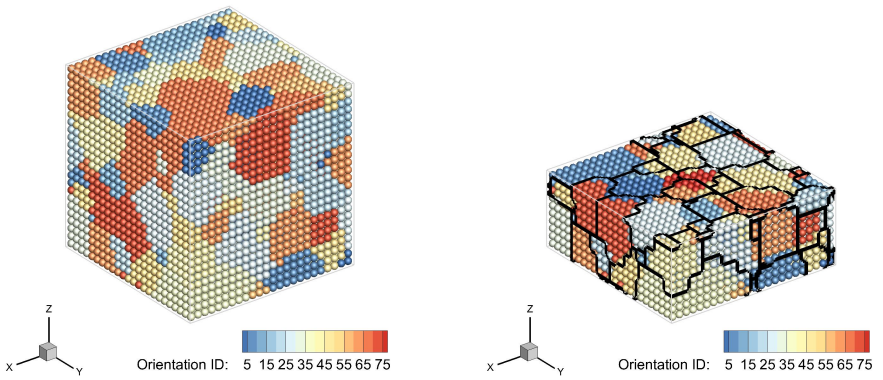

(a) Polycrystal with 78 grains (b) Cutting plane at z = 1.3 mm

Figure 5.9: *3D polycrystal cube with 78 grains. The cube is discretized into particles with a constant particle distance h. The example here has 24 particles along all three directions. Crystals owning the same orientation ID share the same orientation vector. (b) provides the interior information on the cutting plane at z = 1.3 mm. The black lines illustrate grain boundaries.*

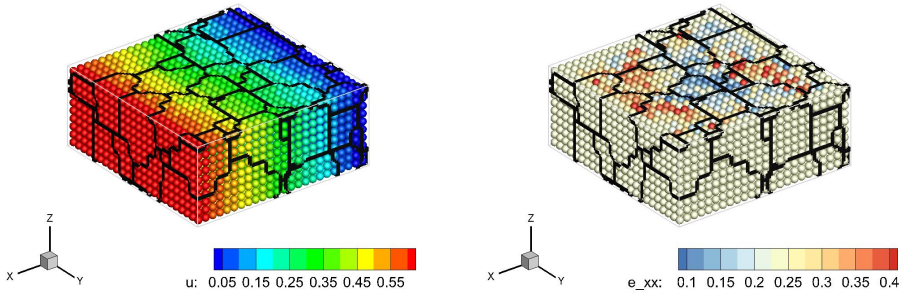

(a) u, $\delta = h$ (b) ϵ_{xx}, $\delta = h$

Figure 5.10: *3D distributions of the displacement component u and strain component* ϵ_{xx} *under plane strain compression with the smallest horizon size. The cutting plane is at* $z = 1.3$ *mm.*

vestigate the displacement and strain maps. The dimension of the cube is the same with that in the texture test, which is $3 \times 3 \times 3$ mm^3. HCP magnesium is applied and two different horizon sizes are used, i.e., $\delta = h$ and $\delta = 2h$, where δ is the horizon radius and h is the distance between nearest particles. The higher-order approximation method, elaborated in the previous chapter, is employed to stabilized the zero-energy

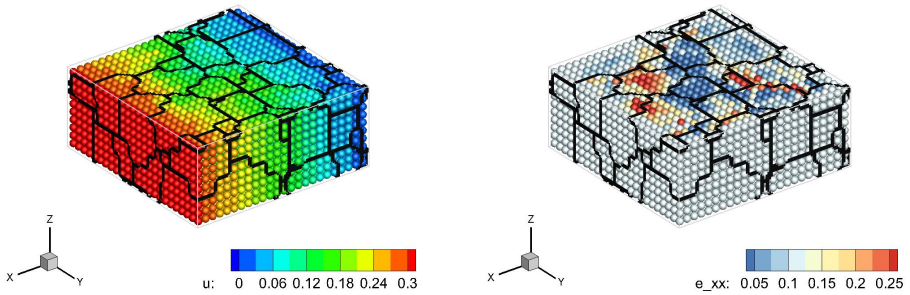

(a) u, $\delta = h$ (b) ϵ_{xx}, $\delta = h$

Figure 5.11: *3D distributions of the displacement component u and strain component ϵ_{xx} under uniaxial compression with the smallest horizon size. The cutting plane is at $z = 1.3$ mm.*

modes.

The plane strain compression velocity gradient $\mathbf{L}^{\mathrm{p}}$ in (5.9) and uniaxial compression velocity gradient $\mathbf{L}^{\mathrm{u}}$ in (5.10) are applied on the boundary, respectively, with a constant strain rate $l_0 = 0.001$. The displacement and strain map is captured at the loading step 200, as provided in Fig. 5.10.

The cutting plane $z = 1.3$ mm is used to better compare the contours with different horizon sizes. Figs. 5.12 and 5.13 give the contours of the displacement and strain with two different horizon sizes under plane strain compression and uniaxial compression, respectively. We mask the shadow particles around the boundary leading to margins along the 4 sides. The shadow particle layer typically becomes thicker as the horizon size increases.

Results obtained form larger horizons exhibit more smooth results. Thanks to the higher-order approximation method, zero-energy-mode oscillations are effectively suppressed. Next step is to increase the mesh density and investigate the convergence with larger horizons.

In the end of this section, we plot the stress-strain curves based on the two de-

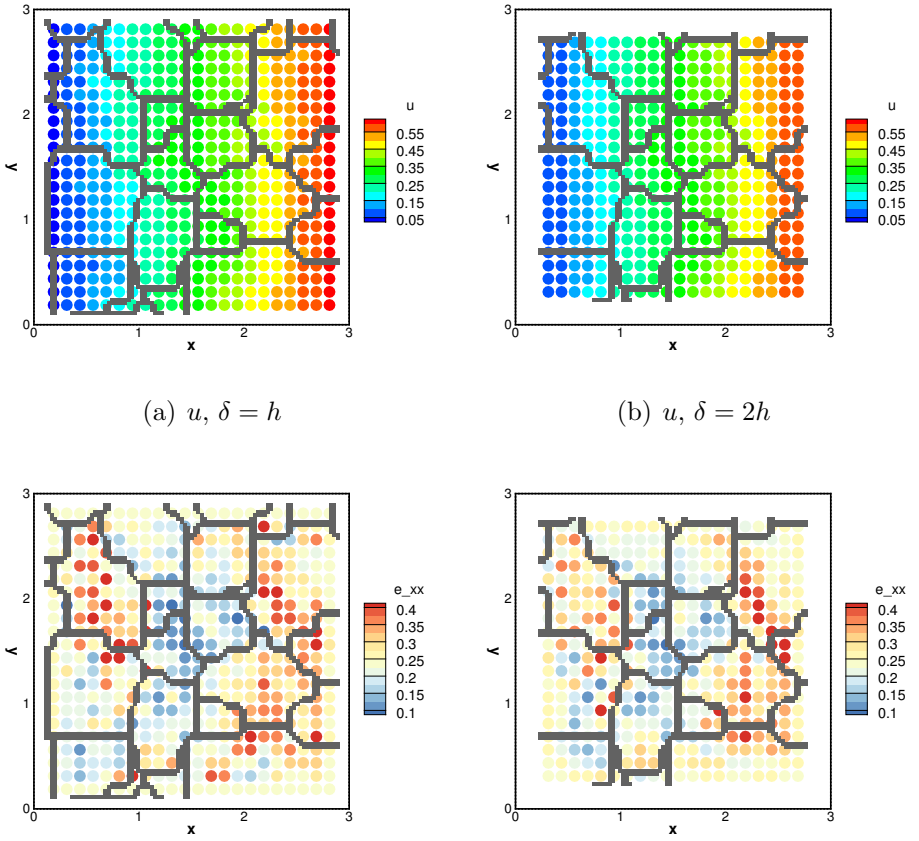

(a) u, $\delta = h$

(b) u, $\delta = 2h$

(c) ϵ_{xx}, $\delta = h$

(d) ϵ_{xx}, $\delta = 2h$

Figure 5.12: *Displacement component u and strain componenet ϵ_{xx} distributions on the cutting plane $z = 1.3$ mm under plan strain compression. Two different horizon sizes are used. Gray interior lines are grain boundaries.*

formation modes with two different horizon sizes. Fig. 5.14 shows that strain and stress behaves in a similar way with different horizon sizes, though larger horizons produce higher curves compared to smaller ones. We attribute this phenomenon to the different shadow particle layers.

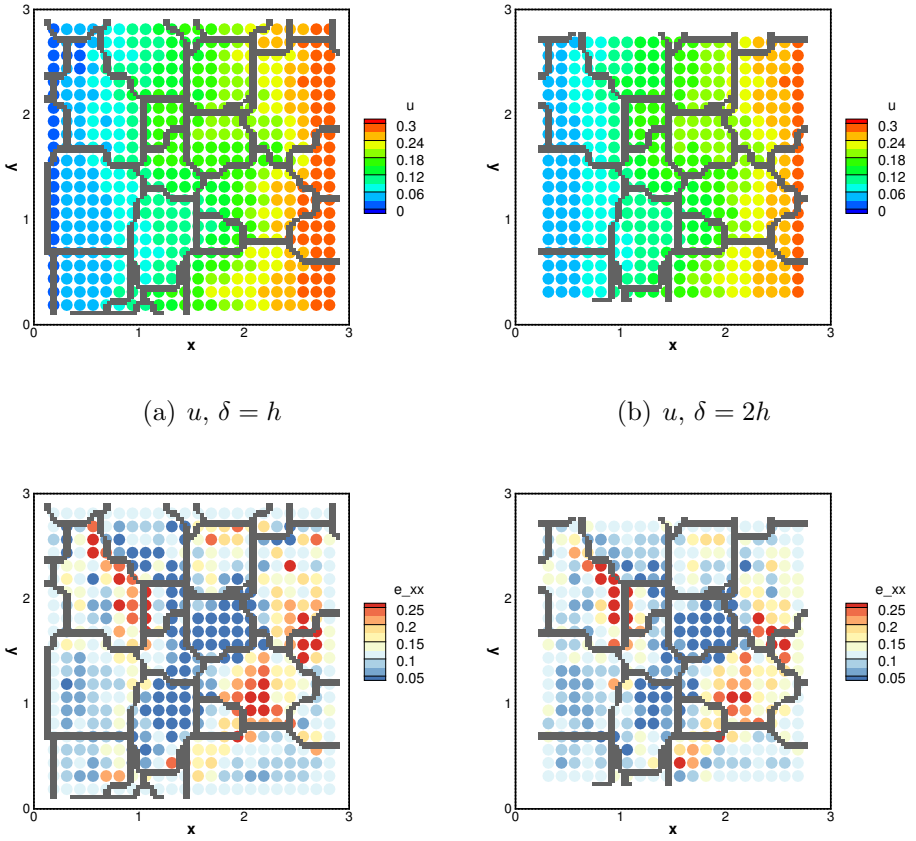

(a) u, $\delta = h$

(b) u, $\delta = 2h$

(c) ϵ_{xx}, $\delta = h$

(d) ϵ_{xx}, $\delta = 2h$

Figure 5.13: *Displacement component u and strain component ϵ_{xx} distributions on the cutting plane $z = 1.3$ mm under uniaxial compression. Two different horizon sizes are used. Gray interior lines are grain boundaries.*

5.3 Preliminary Comparisons between PD Simulations and SEM–DIC Experiment Data

The model will be validated using state-of-the-art in-situ Scanning Electron Microscope–Digital Image Correlation (SEM–DIC) data of WE43 Magnesium alloy [125]. Magnesium is the lightest structural metal and is attractive to automotive and aerospace light-weighting applications. However, magnesium alloys have traditionally exhibited low formability at room temperature. Development of WE alloys (Mg-rare earth alloys) has now allowed relatively high yield and tensile strength properties by pre-

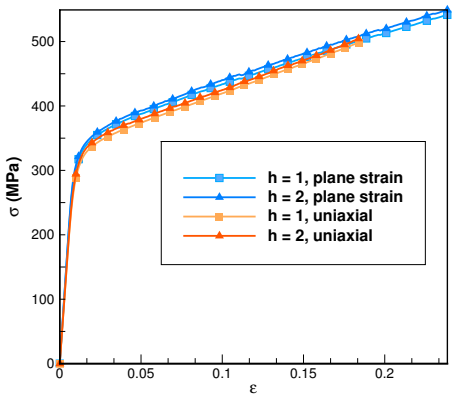

Figure 5.14: *Homogenized stress-strain responses from plane strain compression and uniaxial compression with two different horizon sizes.*

cipitate hardening [126, 127]. However, fracture and fatigue properties are sensitive to localization patterns that develop during deformation [128]. Due to a limited number of slip and twin systems, these localizations strongly depend on multiaxial stress states and the specimen texture.

5.3.1 SEM–DIC experiment data for HCP magnesium

SEM–DIC is a useful in-situ and non-destructive technique for characterizing microscopic surface strains. It tracks the deformation of a speckle pattern placed on the microstructure during thermo-mechanical loading. The details of the SEM-DIC experiments that were performed for the WE43 alloys are described in [1]. The primary material used for the experiments was a hot rolled and annealed WE43 plate of thickness 31 mm. This material is referred to as T5 temper. The samples were solution treated in an open-air furnace at 800K for 8 hours, followed by a water quench. Subsequently, it was subjected to aging treatment in a silicone oil bath at 523K for a peak aging time of 16 hours followed by water quench. This heat treated material is referred to as T6 temper. Samples from both (T5 and T6) tempers were deformed within a SEM load cell and the surface displacement distribution was measured.

EBSD scans of the surface prior to loading is also available. One of the objectives of this work is to validate the PD model by comparing with microstructural response of magnesium alloy WE43. For this purpose:

- We will incorporate a 3D elastoplastic crystal plasticity framework with deformation twinning into the peridynamic framework. The parameters of the model have already been calibrated against both macroscopic stress strain response and the texture in [1] using crystal plasticity finite element method. The slip system and material properties such as elastic modulus and slip parameters used in this thesis are given in Tables 5.4, 5.6, and 5.5.

- Preliminary comparisons will be made between the SEM–DIC experiments and PD simulations for the displacement and strain fields. More detailed tests on the effect of basal Schmid factor, grain size, and boundary conditions on strain localization will be studied in the future.

- Tensile loading: The T5 condition has a basal texture and no twinning is seen under tensile loading. Strain localizations, both intra-grain and along grain boundaries, are seen under tensile loading. The tensile loading case will be used to benchmark the slip activity and grain boundary localizations predicted in the absence of twinning.

The comparison with SEM-DIC experiments will be performed by setting up a boundary value problem (BVP) using the EBSD image of the microstructure within the DIC window. The displacement fields along the boundary of the microstructure are obtained from experiment. The measurements are made on the surface of the sample, which is traction-free, and therefore a plane-stress assumption will be made while setting up the simulation. The slip and twin systems are three-dimensional and the algorithm to solve for the shear strains and stresses in the slip systems proceeds from a 3-D deformation gradient. The problem is set-up in 3-D with a plate of small

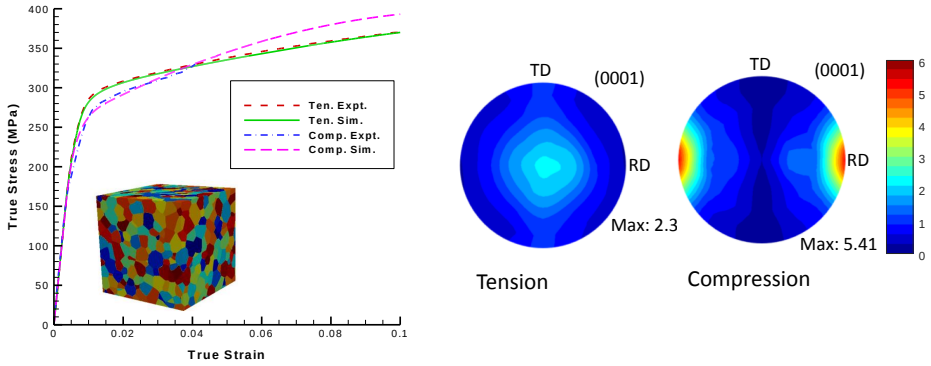

Figure 5.15: *(left) Stress–strain response calibrated using crystal plasticity finite element model for WE43-T5 Magnesium alloy under tension and compression. (right) Predicted pole figures under tension and compression.*

thickness. An example of the CPFE results based on these boundary conditions were previously shown in Fig. 5.15(b). As seen from this results, the average strain intensities are captured but the localizations (including banding, grain boundary, and size effects) are not captured by CPFE.

Fig. 5.16 provides an example of the PD computational domain. The thickness of the plate is always set to be equal to the distance between nearest particles. We have selected two different particle distances. Smallest horizons that only include the closest particles are employed considering there are only two layers of particles. The four sides of the plate are constraint based on DIC experiment data. Each loading step, we apply a small radio, e.g., 1/500 of the total displacements. In addition, the bottom surface is constraint only on the w displacement.

In HCP alloys, the predominant slip systems are the basal, prismatic, pyramidal $< a >$ and pyramidal $< c + a >$ systems [129]. The parameters for these systems, such as the initial slip system resistance and hardening constants, have been developed using a crystal plasticity finite element model previously [1] and will be used in the PD approach. It is to be noted that the $< c + a >$ slip system is the only one capable of accommodating strains along the crystal $< c >$ direction. This system is difficult to activate at room temperature due to the high initial slip resistance [130].

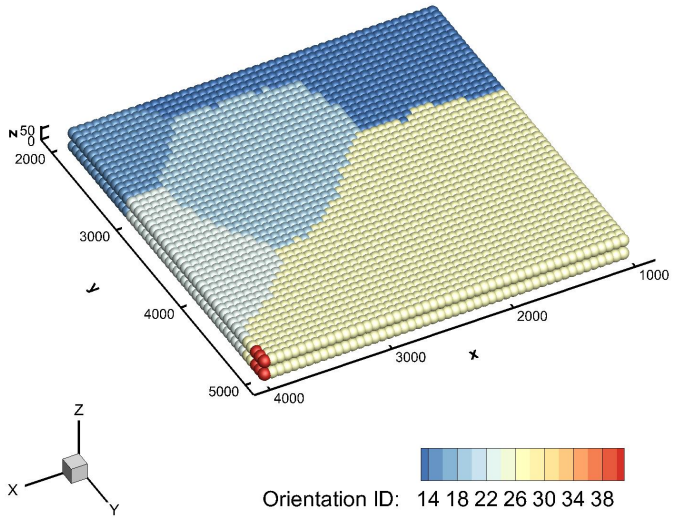

Figure 5.16: *3D PD DIC thin layer computational domain. The dimension unit is micrometer. There are 50 particles in the x and y direction in this examples. Only two layer particles are employed. The thickness of the plate is the same with the distance between nearest particles.*

Twinning provides an additional deformation mode along the $< c >$ direction, but its unidirectional nature results in a strong asymmetry in mechanical properties. In Mg alloys, the extension twinning system (which leads to a tensile strain parallel to the c-axis) is activated during in-plane compression. Under compression, low yield strength and hardening rate, followed by an increase in hardening at higher strains (due to twin exhaustion), is observed. The tensile twins significantly affect the texture by reorientation of the grains by an angle of about 86 degrees. Under cyclic loading, detwinning can also occur.

For modeling purposes, twin systems will be considered as pseudo-slip systems and are sheared until they are reoriented [131]. The total twin volume fraction, which is the total accumulated pseudo-slip divided by the characteristic shear of the twin system, will be computed in each particle. In Magnesium, extension twins are active in compression (as known from DIC trace analysis) with a characteristic shear of 12.9%. The approach for twinning is similar to the PTR scheme [131]. The main

difference from the PTR scheme is that only the particle will be reoriented here instead of reorienting an entire grain.

5.4 3D Thin Layer Simulations

Similar contours of the displacement fields can be observed between DIC experiment data and CPPD results, as shown in Fig. 5.17. Two different meshes are used: one has 50 particles in the x-direction and the other has 100 particles. Strain components ϵ_{xx}, ϵ_{yy}, and ϵ_{xy} are plotted in Fig. 5.18. Finally, The relative activity of the three basal slip systems in a mesh with 50 particles in the x direction are provided in Fig. 5.19. However, there are some errors in results with 100 particles in the x direction which we need to fix in the future.

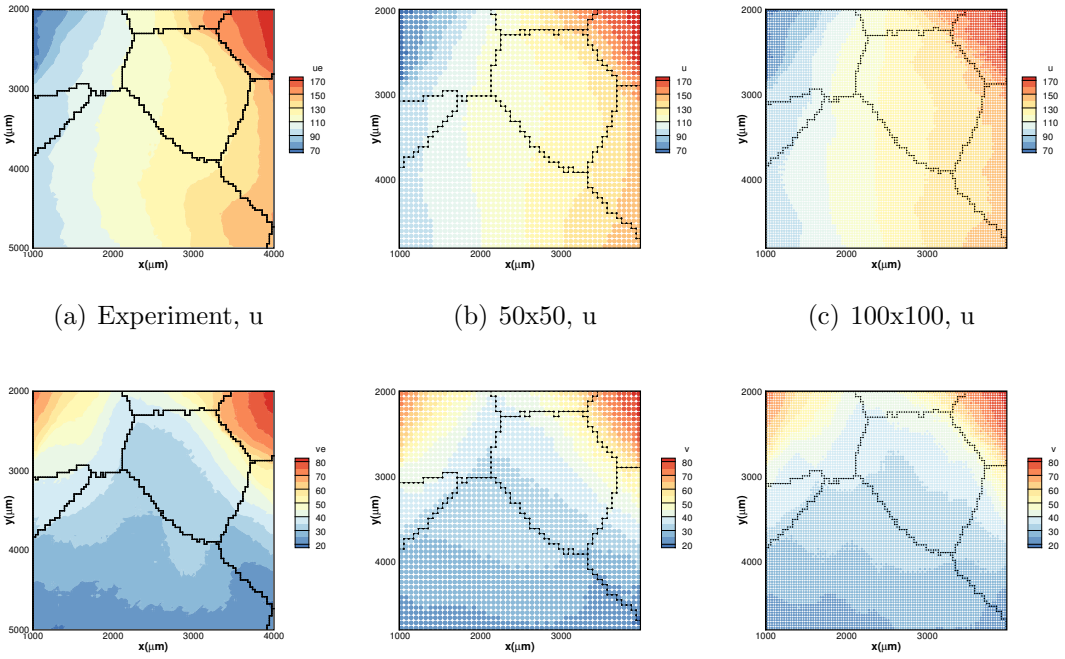

(a) Experiment, u (b) 50x50, u (c) 100x100, u

(d) Experiment, v (e) 50x50, v (f) 100x100, v

Figure 5.17: *Displacement fields oabtained from DIC data and two different particle meshes.*

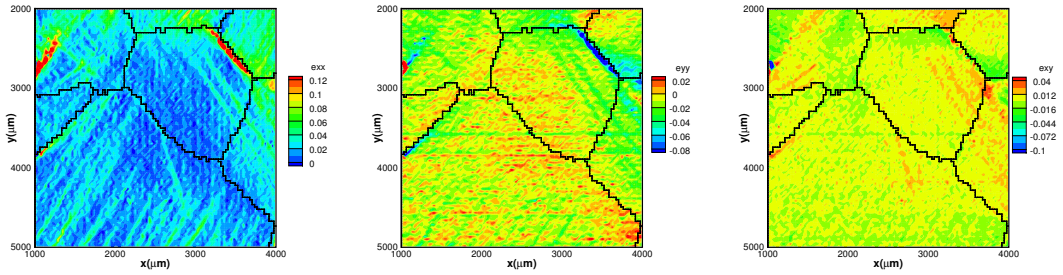

(a) Experiment, ϵ_{xx} (b) Experiment, ϵ_{yy} (c) Experiment, ϵ_{xy}

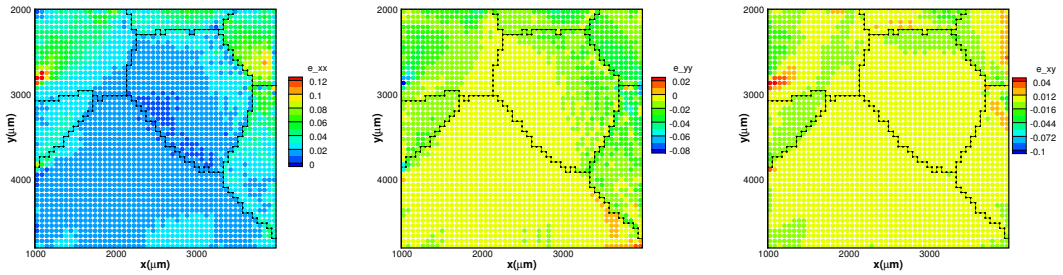

(d) 50x50, ϵ_{xx} (e) 50x50, ϵ_{yy} (f) 50x50, ϵ_{xy}

Figure 5.18: *Strain component ϵ_{xx}, ϵ_{yy}, and ϵ_{xy} fields (from top to bottom) (left) from DIC data (right) with 50 particles in the x direction.*

5.5 Conclusions

This chapter presents the first 3D implementation of crystal plasticity using peridynamics theory. We certified the CPPD model in computing the texture of FCC and HCP 3D polycrystals under two different compression deformation modes. Two horizon sizes are employed to investigate the displacement and strain fields of the 3D polycrystal cube. The PD solutions are compared with a recent DIC experiment of uniaxial tension in Magnesium WE43 alloy. Finer localization bands are found in the PD results compared with FEM. Two samples of the input files to create a 3D cube domain or a thin layer are provided in Appendix E.

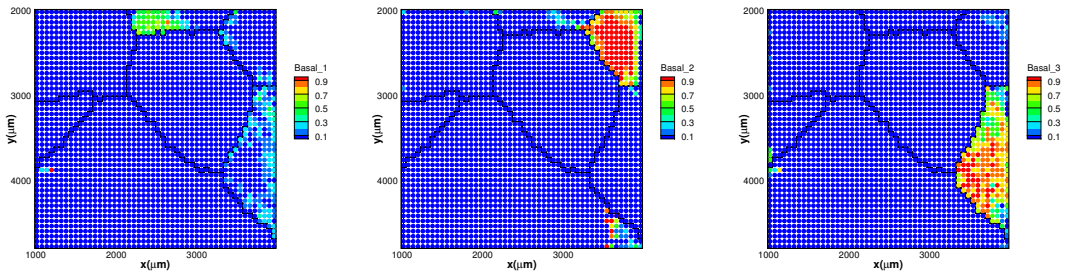

(a) $\frac{\gamma_{(0001)[11\bar{2}0]}}{\sum\gamma}$ (b) $\frac{\gamma_{(0001)[\bar{2}110]}}{\sum\gamma}$ (c) $\frac{\gamma_{(0001)[1\bar{2}10]}}{\sum\gamma}$

Figure 5.19: *The relative activity of the three basal slip systems in a mesh with 50 particles in the x direction.*

CHAPTER VI

Stress-Point Model for Stabilizing Zero-Energy Modes in PD-ADRS

In the current work, we propose a stress-point approach, as a numerical means to mitigate zero-energy modes with particle discretizations. The use of stress points has been proposed in the past for other integral methods such as smoothed particle hydrodynamics to address tensile instability issues [94, 95]. The idea is straightforward. Addition of even one more independent stress point in 1D problems leads to two gradients and three displacements which significantly reduces the null space. This stress-point peridynamic model is first demonstrated in a simple 1D problem and then applied to higher-dimensional problems. Using these numerical examples, we show that zero-energy-mode oscillations in all solutions are completely damped.

6.1 1D Stress-Point Peridynamic Scheme

Based on the stress-point approach addressing tension instability in smoothed particle hydrodynamics (SPH) methods [94], and its relevance to particle-based model of peridynamics [132], a new stress-point scheme is proposed and explained below.

In order to enhance particle connections, a few quantities related to stress are calculated twice in the horizon of particles. Take the 1D bar in Fig. 6.1 as an example.

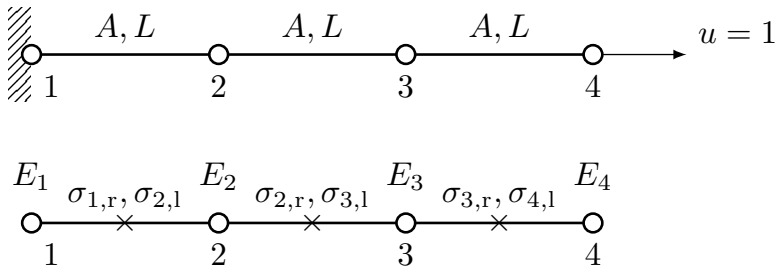

Figure 6.1: *An illustration of the stress-point peridynamic scheme on a 1D elastic bar. The bar is fixed at left with a displacement loading at right and discretized into four peridynamic particles. The total length and cross-sectional area are $3L$ and A, respectively. Assume particles only interact with nearest neighbors.*

Two stresses, σ_{l} and σ_{r}, are calculated at left and right of each particle by splitting the neighborhood and using the corresponding bond, respectively. For instance, $\sigma_{2,\mathrm{l}}$ and $\sigma_{2,\mathrm{r}}$ are calculated on the two sides of particle 2 while only $\sigma_{1,\mathrm{r}}$ is calculated at the right side of particle 1. Overall, the shape tensor, deformation gradient, strain, and stress are computed at stress points located at the middle of adjacent particles, in contrast with field variables such as displacement and material properties which are calculated at particles.

Note that, even at the same location, $\sigma_{1,\mathrm{r}}$ is not always equal to $\sigma_{2,\mathrm{l}}$. They are distributed in the horizons of particle 1 and 2, respectively. Quantities are visible only in a shared horizon to protect the completeness and closure of horizons.

Take particle 2 for example and assume particles only interact with nearest neighbors. Deformation gradients $F_{2,\mathrm{l}}$ and $F_{2,\mathrm{r}}$ only consider the corresponding bond on the left and right of particle 2, respectively (using Eq. 2.19, and $\omega = 1$):

$$\begin{aligned} F_{2,\mathrm{l}} &= [-(u_1 - u_2 - L)]AL^2/K_{2,\mathrm{l}} = \frac{u_2 - u_1}{L} + 1, \\ F_{2,\mathrm{r}} &= (u_3 - u_2 + L)AL^2/K_{2,\mathrm{r}} = \frac{u_3 - u_2}{L} + 1, \end{aligned} \tag{6.1}$$

where the shape tensors $K_{2,\mathrm{l}}$ and $K_{2,\mathrm{r}}$ are calculated as

$$K_{2,\mathrm{l}} = (-L)(-L)AL = AL^3,$$
$$K_{2,\mathrm{r}} = L \cdot L \cdot AL = AL^3. \tag{6.2}$$

As for the equation of motion at particle 2, it turns into

$$(-\sigma_{1,\mathrm{r}} K_{1,\mathrm{r}}^{-1} L - \sigma_{2,\mathrm{l}} K_{2,\mathrm{l}}^{-1} L)V + (\sigma_{2,\mathrm{r}} K_{2,\mathrm{r}}^{-1} L + \sigma_{3,\mathrm{l}} K_{3,\mathrm{l}}^{-1} L)V = 0$$
$$\Longrightarrow -\sigma_{1,\mathrm{r}} - \sigma_{2,\mathrm{l}} + \sigma_{2,\mathrm{r}} + \sigma_{3,\mathrm{l}} = 0. \tag{6.3}$$

If we make a further step to assume the material is elastic with a constant Young's modulus E and under small deformation (see Appendix B), equation (6.3) then becomes

$$u_1 - 2u_2 + u_3 = 0. \tag{6.4}$$

Compared to the original peridynamic scheme, the difference is that all particle displacements are involved in (6.4). This treatment will prevent the zero-energy mode occurring from the source.

In terms of larger-horizon peridynamic discretizations, the scheme with only two stress points is still applied in one horizon. Same process can be followed as (6.1) and (6.2) in calculating shape tensors and deformation gradients, while the force states in (6.3) is supposed to be computed based on stresses sharing the common bond. In other words, the stress term in (2.26) are calculated at the stress point owing the same bond $\boldsymbol{\xi}$. This criterion will be obeyed in higher-dimensional stress-point schemes.

6.2 Higher-Dimensional Stress-Point Peridynamic Schemes

Two guidelines are used when we extend the stress-point approach to higher dimensions. The first is to enhance connections between particles by using all particle

displacements in the deformation measures. The second is to keep the completeness and closure of horizons, by modeling stress interactions similar to the 1D scheme.

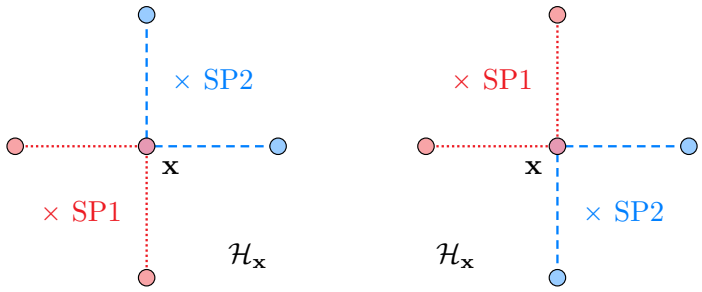

Figure 6.2: *A 2D stress-point scheme with two stress points. Blue and red stress points only take charge of bonds with the same color at the same side. There are two choices based on the location of stress points.*

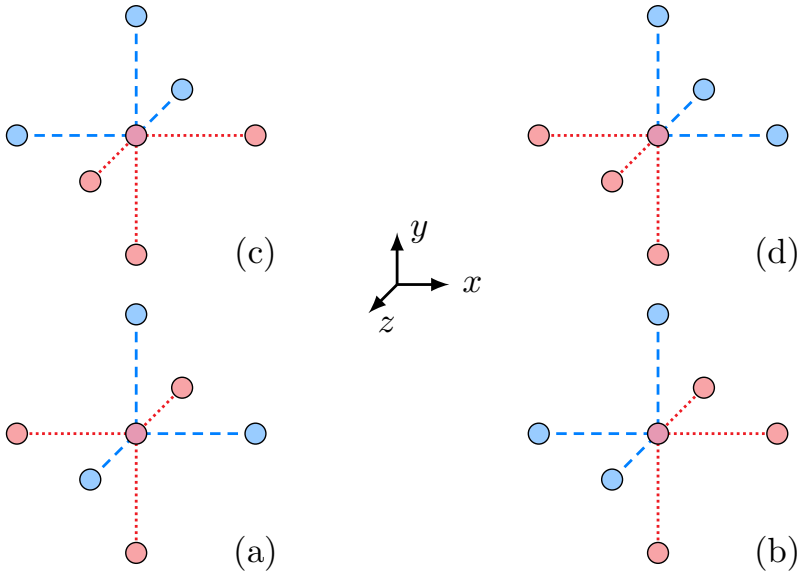

Figure 6.3: *A 3D stress-point scheme with two stress points. Blue and red stress points only take charge of bonds with the same color at the same side. There are four choices (a)–(d) based on the location of stress points.*

Assume particles can only interact with nearest neighbors. Starting from 2D problems, a scheme with two stress points is adopted. More stress points can be employed to increase the accuracy, however, higher computation cost is expected. As illustrated in Fig. 6.2, the two stress points are located at two sides of the center particle and each one only takes charge of the two bonds on the same side. For

example, blue stress points (SP2) only consider blue bonds and the same with red stress points (SP1). Hence there are two cases in 2D problems.

Similar to the 2D scheme above, only two stress points are employed in our 3D model. However, there are totally four cases in 3D problems, as shown in Fig. 6.3, and each stress point owns three bonds in the horizon. To avoid directional bias, we randomly select the location of stress-points at each particle in the following 2D and 3D examples, using a random number generator to choose one case from Figs 6.2 and 6.3 when assigning stress points to each particle.

When it comes to the equation of motion, we compute the force states based on stresses sharing the common bond, as we mentioned in the 1D stress-point model with larger horizons. During postprocessing, the stress is recalculated as the average of stress-point values in one horizon once we find the displacement fields. Another case to consider are the boundary particles because their horizons are defective. In nearest-neighbor discretizations, we allocate only one stress point to include all the bonds in the boundary particle to solve this problem. In terms of larger-neighbor discretizations, the boundary treatment introducing the fictitious boundary layer (see Chapter IV Section 4.4) will be employed.

6.3 Zero-Energy-Mode Control Methods with Supplementary Particle Forces

In order to demonstrate the effect of stress-point approach, a control method with supplementary particle forces to suppress zero-energy modes is introduced. This method has been analyzed with respect to its effect on material stability in Silling's paper [102].

In this method, an artificial force state is introduced, $\underline{\mathbf{T}}_{\mathrm{a}}[\mathbf{x}]\langle \mathbf{x}' - \mathbf{x} \rangle$, at particle $\mathbf{x}$

on the bond $\mathbf{x}' - \mathbf{x}$, which is

$$\underline{\mathbf{T}}[\mathbf{x}, t]\langle \mathbf{x}' - \mathbf{x} \rangle = \omega \mathbf{P}\mathbf{K}^{-1}\boldsymbol{\xi} + \underline{\mathbf{T}}_{\mathrm{a}}[\mathbf{x}]\langle \mathbf{x}' - \mathbf{x} \rangle. \tag{6.5}$$

This artificial force can be generated by either interconnected springs or average displacement states [87]. Linear springs are introduced between particles in the first method:

$$\underline{\mathbf{T}}_{\mathrm{a}}[\mathbf{x}]\langle \mathbf{x}' - \mathbf{x} \rangle = C_1 \omega [\mathbf{u}(\mathbf{x}') - \mathbf{u}(\mathbf{x})], \tag{6.6}$$

where C_1 is a spring constant. The second method computes the added force based on an average of all displacement states over one horizon, which is

$$\underline{\mathbf{T}}_{\mathrm{a}}[\mathbf{x}]\langle \mathbf{x}' - \mathbf{x} \rangle = C_2 \int_{\mathcal{H}_{\mathbf{x}}} \omega [\mathbf{u}(\mathbf{x}') - \mathbf{u}(\mathbf{x})] dV_{\mathbf{x}'}. \tag{6.7}$$

Another penalty approach, which is the third control method in [87, 93], is not discussed in this thesis, since it is conceptually similar to the method of applying supplemental forces along each bond.

These supplementary forces have a suppression effect on zero-energy modes. However, this effect highly depends on the mesh size and the problem itself. In addition, to determine the optimum values of the artificial coefficients, i.e., C_1 and C_2, calculations need to be performed beforehand[87, 93]. None of these methods completely suppresses zero energy modes.

6.4 Results and Discussions

We assume materials are elastic under small deformation in the following numerical examples. Strain tensor is computed as $\boldsymbol{\epsilon} = 1/2(\mathbf{F}^{\mathrm{T}} + \mathbf{F}) - \mathbf{I}$, where $\mathbf{I}$ is the identity tensor. Cauchy stress $\boldsymbol{\sigma} = \mathbf{D} : \boldsymbol{\epsilon}$, is used in lieu of $\mathbf{P}$ (assuming small deformations) in (2.26) and $\mathbf{D}$ is an isotropic elastic modulus tensor. The horizon radius δ is kept

minimum merely including the nearest neighbor particles and the influential function ω is set to be constant 1 for simplicity.

6.4.1 1D bar test

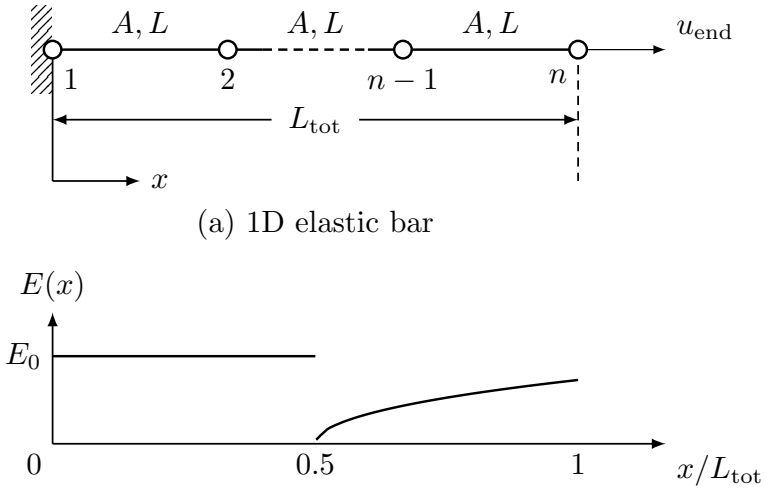

(a) 1D elastic bar

(b) Young's Mudulus along x

Figure 6.4: *A 1D elastic bar under tension with a Young's modulus varied along the x axis.*

In order to compare with the analytical solution and control methods with adding supplementary particles forces, a similar 1D elastic bar test in [87, 93] is conducted, as shown in Fig. 6.4. The bar with a total length L_{tot} is discretized as n peridynamic particles. Displacement constraints, $u_1 = 0$ and $u_n = u_{end}$, are applied on the two sides of the bar. A variable Young's modulus is adopted as

$$E(x) = \begin{cases} E_0 & 0 \le x \le L_{\text{tot}}/2 \\ E_0\left(1 + \frac{\beta}{2\alpha}\frac{1}{\sqrt{x/L_{\text{tot}} - 1/2}}\right)^{-1} & L_{\text{tot}}/2 < x \le L_{\text{tot}} \end{cases}, \tag{6.8}$$

and the analytical displacement $u(x)$ and strain $\epsilon(x)$ solutions are

$$u(x) = \begin{cases} \alpha x & 0 \le x \le L_{\text{tot}}/2 \\ \alpha x + \beta L_{\text{tot}} \sqrt{x/L_{\text{tot}} - 1/2} & L_{\text{tot}}/2 < x \le L_{\text{tot}} \end{cases}, \tag{6.9}$$

$$\epsilon(x) = \begin{cases} \alpha & 0 \le x \le L_{\text{tot}}/2 \\ \alpha + \beta \Big(2\sqrt{x/L_{\text{tot}} - 1/2} \Big)^{-1} & L_{\text{tot}}/2 < x \le L_{\text{tot}} \end{cases}, \tag{6.10}$$

where parameters are selected as $L_{\text{tot}} = 1$, $E_0 = 1$, $u_{\text{end}} = 0.005$, $\alpha = 0.001$, and $\beta = 0.004\sqrt{2}$. Note that the expression of Young's modulus is slightly different from the references [87, 93]. This is because parameters α and β adopted in this paper are dimensionless.

We define two local amplitudes of oscillation, $a_{u,i}$ and $a_{e,i}$, at particle i to quantitatively measure the effect of zero-energy modes in displacement and strain fields, respectively:

$$a_{u,i} = |\frac{u_i^{\text{num}} - u_i^{\text{exact}}}{u_i^{\text{exact}}}|, \text{and } a_{e,i} = |\frac{\epsilon_i^{\text{num}} - \epsilon_i^{\text{exact}}}{\epsilon_i^{\text{exact}}}| \tag{6.11}$$

where ϵ_i^{num} and $\epsilon_i^{\text{exact}}$ the numerical and analytical strain at particle i, respectively. The L_2 norm and amplitude is set to be zero if the analytical solution is zero.

Table 6.1: *Optimum values of C_1 and C_2 in* (6.6) *and* (6.7) *for adding artificial springs and average displacement states. Only the nearest-neighbor particle discretizations are considered. n is the number of particles.*

n	100	200	500	1000
C_1*	0.8	1.28	2	3
C_2*	60	150	500	1750

* C_1 and C_2 are not dimensionless.

The old peridynamic scheme without any control of zero-energy modes (No control), two control methods adding artificial force states by linear springs (Springs) and average displacement force states (ADS), and the new stress-point approach (Stress-

point) are applied to solve the 1D numerical problem, respectively. Four different mesh sizes are employed and first off, only the nearest-nerighbor particle discretizations are considered. Optimum values of C_1 and C_2 are obtained by multiple attempts beforehand, as elaborated in [87, 93]. These values change with the mesh size and are listed in Table 6.1.

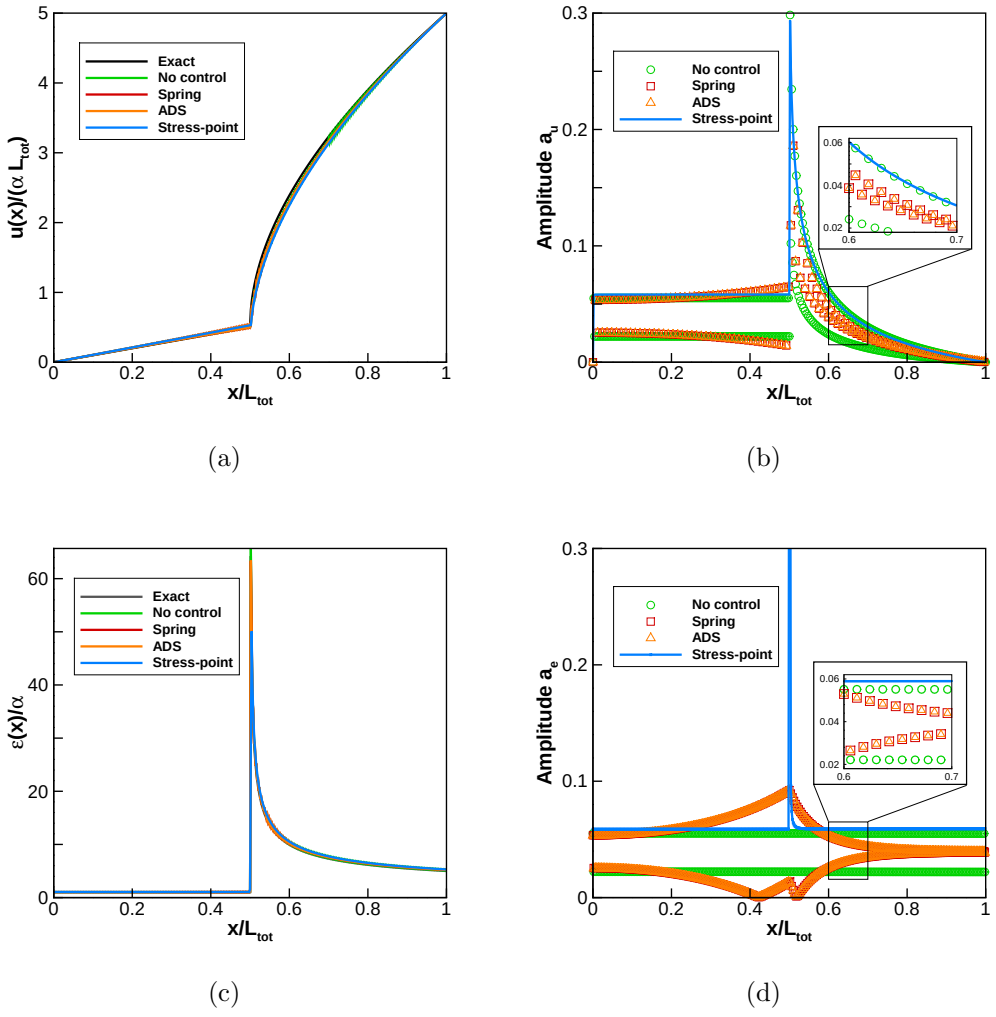

Figure 6.5: *Effect of zero-energy modes on displacement and strain fields of 1D bar based on four control methods. (a) and (c) are the displacement and strain distribution, respectively, while (b) and (d) are corresponding local amplitudes. Local zoomed-in views are provided to distinguish symbols. All Results are based on a mesh with 500 particles.*

Numerical results of the displacement and strain distribution, as well as their

relative amplitudes of oscillation are plotted in Fig. 6.5. All results are based on a mesh size with 500 peridynamic particles. Even though all numerical results are close to the analytical results, as shown in Fig. 6.5(a) and (c), zero-energy modes are not alleviated in any method other than stress-point approach. In the amplitude plots, only stress-point approach has a smooth single line. Two or more separate lines are observed in other control methods and this is because the numerical solutions are oscillating between a range, the oscillations are not shown to improve plot clarity.

We find that adding force states can indeed suppress oscillations in the nonlinear region, i.e., $L_{\text{tot}}/2 < x \leq L_{\text{tot}}$, however, it fails in the linear region, $L_{\text{tot}}/2 < x \leq L_{\text{tot}}$. Another disadvantage of adding artificial force states, as we mentioned previously, is that their constants, C_1 and C_2, are supposed to be carefully selected before satisfactory results are obtained. Even worse, their optimum values are changing with mesh sizes, as shown in Table 6.1. Hence, in higher-dimensional examples we will be only be focused on comparisons between the stress-point model and the peridynamic model with no control of zero-energy modes. The stress-point method is demonstrated to be effective on suppressing zero-energy modes in the 1D bar example. Note that higher jumps are observed in Fig. 6.5(b) and (d) compared to analytical solution. This is because we average the stress based on stress-point values on the two sides at the point of discontinuity.

Next, results based on the stress-point approach with different horizon sizes are plotted in Fig. 6.6. It shows that smallest horizon size produces the most accurate approximations. As the horizon size decreases, the approximation is closer to the analytical solution. In addition, all solutions are smooth with no zero-energy modes observed.

Finally, a comparison between the stress-point approach and the higher-order approximation (see Chapter IV) is conducted and results are shown in Fig. 6.7. We saw that using $\omega = 1$ for higher-order neighbors gives strong zero energy mode oscillations

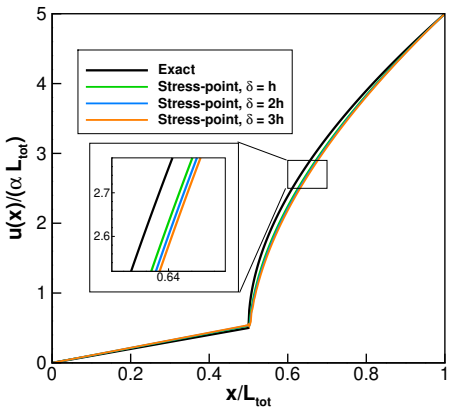

Figure 6.6: *Comparison of the displacement fields obtained from the stress-point approach based on three different horizon sizes. δ is the horizon size and h is the distance between nearest particles.*

and as the horizon size increases, the oscillations grow dramatically. Compared to the higher-order approximation method, the stress-point model removes the oscillations in call cases, though the former method is more accurate as it is closer to the analytical solution.

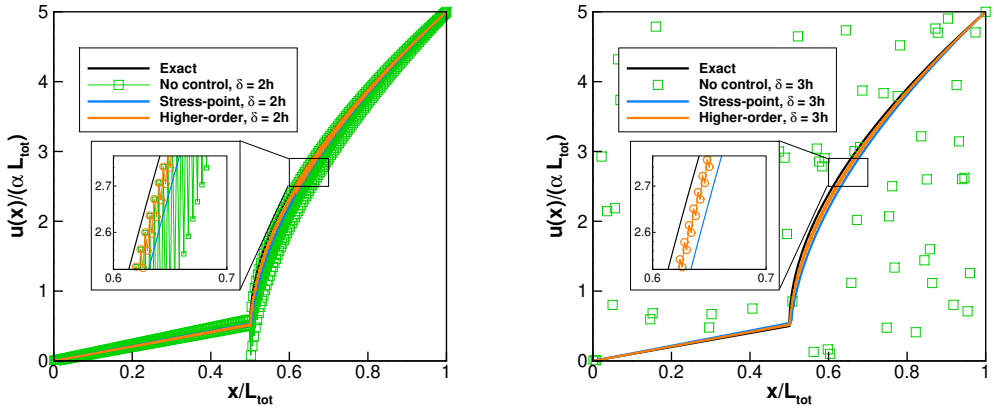

(a) $\delta = 2h$ (b) $\delta = 3h$

Figure 6.7: *Effect of zero-energy modes on displacement fields of 1D bar based on three control methods with two different horizon sizes. All Results are based on a mesh with 500 particles.*

6.4.2 2D plate test

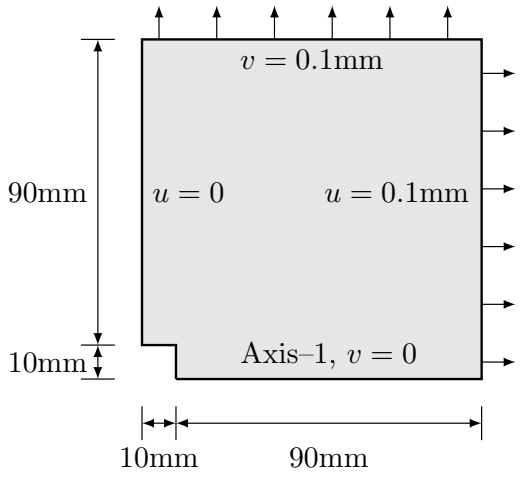

Figure 6.8: *A quarter of 2D elastic plate with a squared opening under uniform stretch. Symmetric displacement boundary conditions are applied at the border.*

An example of 2D elastic plate with a square hole at center under uniform stretch is modelled. We only consider a quarter of the plate due to symmetry with dimensions shown in Fig. 6.8. Displacement loading is applied at the four borders. The material is assumed to be isotropic elastic with Young's modulus $E = 1000$MPa and Poisson's ratio $\nu = 0.3$. As seen here, compared to the variable Young's modulus $E(x)$ in the previous 1D example, a constant E can still bring in zero-energy modes in higher-dimensional problems.

Fig. 6.9 is a comparison of u-displacement contours based on the peridynamic model without any control of zero-energy modes (No control) and the stress-point approach (Stress-point, see Section 6.2). The particle spacing is $h = 2$mm. Conspicuous oscillations can be observed around the squared opening in the results with no control of zero-energy modes, in contrast with smooth results using the stress-point method.

Next, we defined two local amplitudes of oscillation, $a_{u,i}$ and $a_{\sigma,i}$, at particle i to quantitatively measure the effect of zero-energy modes in the displacement and stress

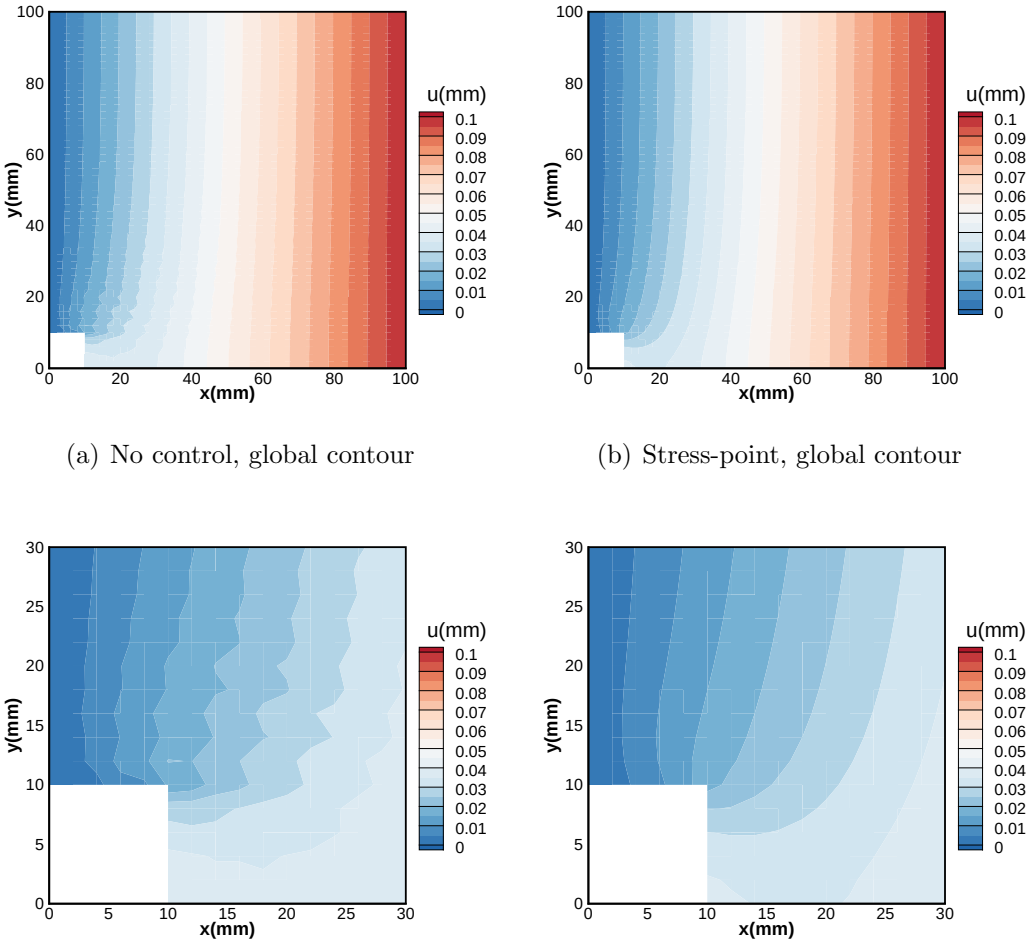

(a) No control, global contour

(b) Stress-point, global contour

(c) No control, zoomed-in opening

(d) Stress-point, zoomed-in opening

Figure 6.9: *Contours of the u-displacement obtained from the peridynamic model with no control of zero-energy modes and the new stress-point approach.*

fields, respectively:

$$a_{u,i} = |\frac{u_i^{\text{PD}} - u_i^{\text{FEM}}}{u_i^{\text{FEM}}}|, \text{and } a_{\sigma,i} = |\frac{(\sigma_{xx})_i^{\text{PD}} - (\sigma_{xx})_i^{\text{FEM}}}{(\sigma_{xx})_i^{\text{FEM}}}| \tag{6.12}$$

where superscripts PD and FEM denote the peridynamic and finite-element analysis results, respectively. We applied a quasi-static FEM formulation using four noded quadrilateral elements in the 2D problem and eight noded hexahedral elements in 3D. Finite-element nodes are assigned right at the place of peridynamic particles in order

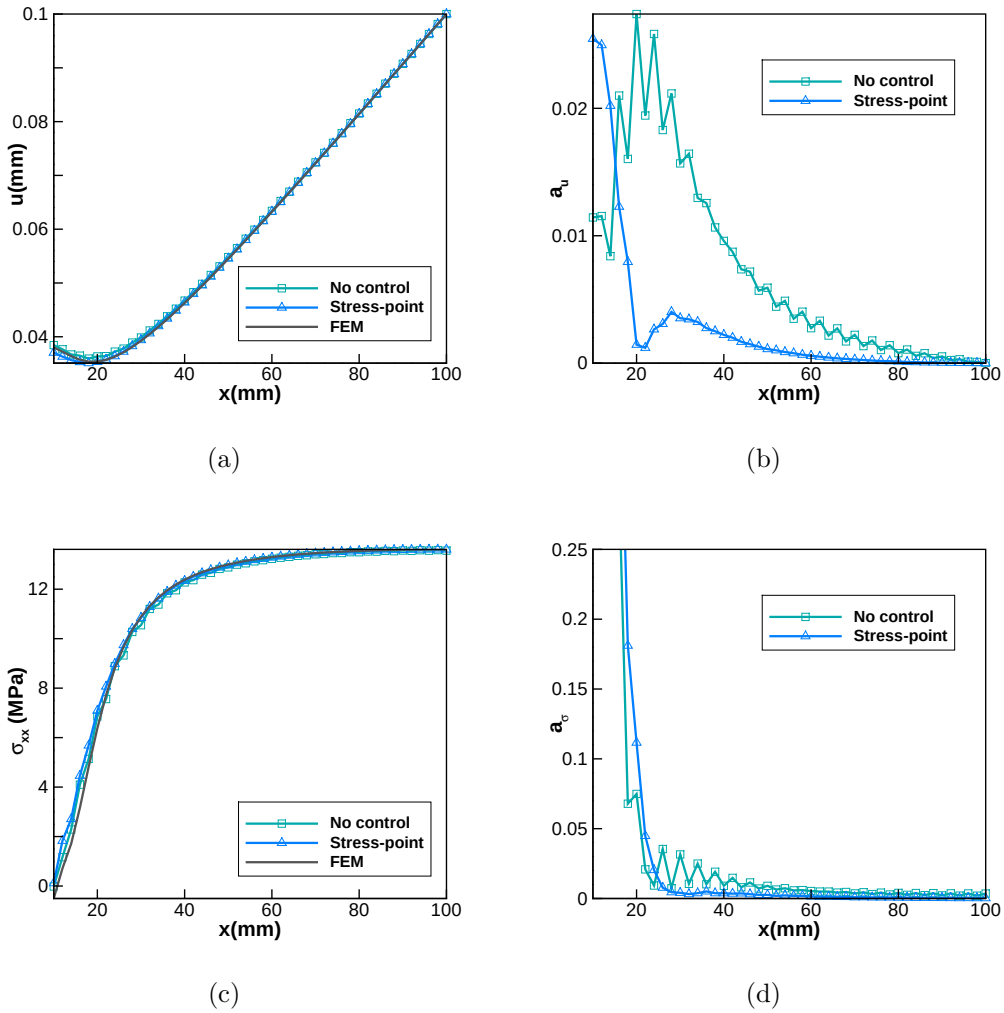

Figure 6.10: *Distributions of u-displacement, stress σ_{xx}, and their relative amplitudes along the axis-1 obtained from the peridynamic model with no control of zero-energy modes (No control), the new stress-point approach (Stress-point), and finite-element method (FEM).*

to quantitatively compare with peridynamic solutions with a vanishing horizon. Note that finite-element solutions (which are of local nature) are utilized as a reference rather than benchmark when we compare peridynamic results between the stress-point and no-control approaches.

The u-displacement, horizontal stress σ_{xx}, and their amplitudes of oscillations along the horizontal axis–1 ($y = 0$mm, see Fig. 6.8) are plotted in Fig. 6.10. The disagreement between PD and FEM solutions mainly lies near the squared opening

on the left. This is because PD is based on a non-local integral formulation wherein stress singularity at the sharp corner is avoided [7]. If we pay closer attention to the region away from the left corner, i.e., $x > 20$mm, the stress-point approach produces very smooth results, in both displacement and stress field, compared to oscillations in the old PD model without control of zero-energy modes.

6.4.3 2D polycrystal plane

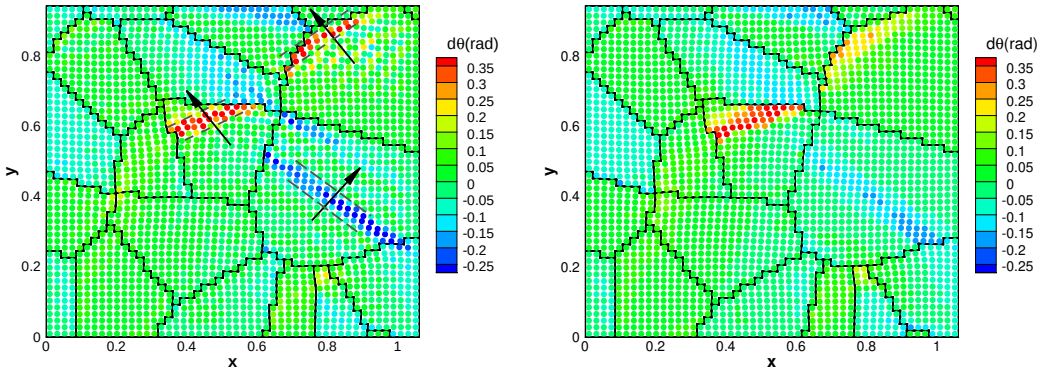

(a) No control

(b) Stress-point

Figure 6.11: *Reorientation of grains obtained from the peridynamic model with no control of zero-energy modes and the stress-point approach.*

6.4.4 3D brick test

A 3D elastic brick example is considered in this section. The length-width-height ratio of the brick is $2d : 2d : d$, where $d = 40$mm. Displacement loadings are applied on its four sides, as shown in Fig. 6.12, while the top and bottom faces are left traction-free. The material is assumed isotropic with Young's modulus $E = 1000$ MPa and Poisson's ratio $\nu = 0.3$. The particle spacing is selected as $h = d/16 = 2.5$mm.

A comparison of z-displacement contours, computed by the old peridynamic model without any control of zero-energy modes (No control) and the stress-point approach

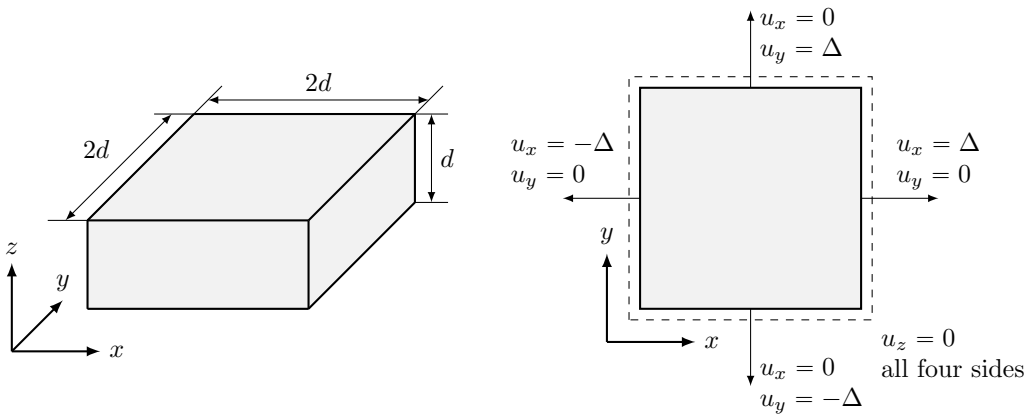

Figure 6.12: *A 3D elastic brick example with dimension $d = 40mm$. Displacement boundary conditions are applied on four sides while the top and bottom are left traction-free. The small displacement increment is $\Delta = 0.4mm$.*

(Stress-point), are plotted in Fig. 6.13. The overall contours are similar while disagreements exist. Serrated contours are observed if no control method is applied. Moreover, zero-energy modes are eliminated not only on the surface but also inside the brick, as shown in Fig. 6.13(b).

Next, we recomputed the 3D brick problem with the finite-element method and assigned element nodes right at the location of the peridynamic particles. The z-displacement and its relative amplitudes a_w, defined similar to (6.12) but based on z-displacement, on a selected line located at $x = 40$mm and $z = 0$mm varied along y-direction are shown in Fig. 6.14. The overall contours of the three methods are similar. Disagreements between peridynamics and finite–element method solutions come up near the boundaries due to the non-local integral formulation. As we move away from the boundary, zero-energy modes are more evident if no control method is applied. By contrast, the stress-point approach has a strong suppression effect on the oscillations.

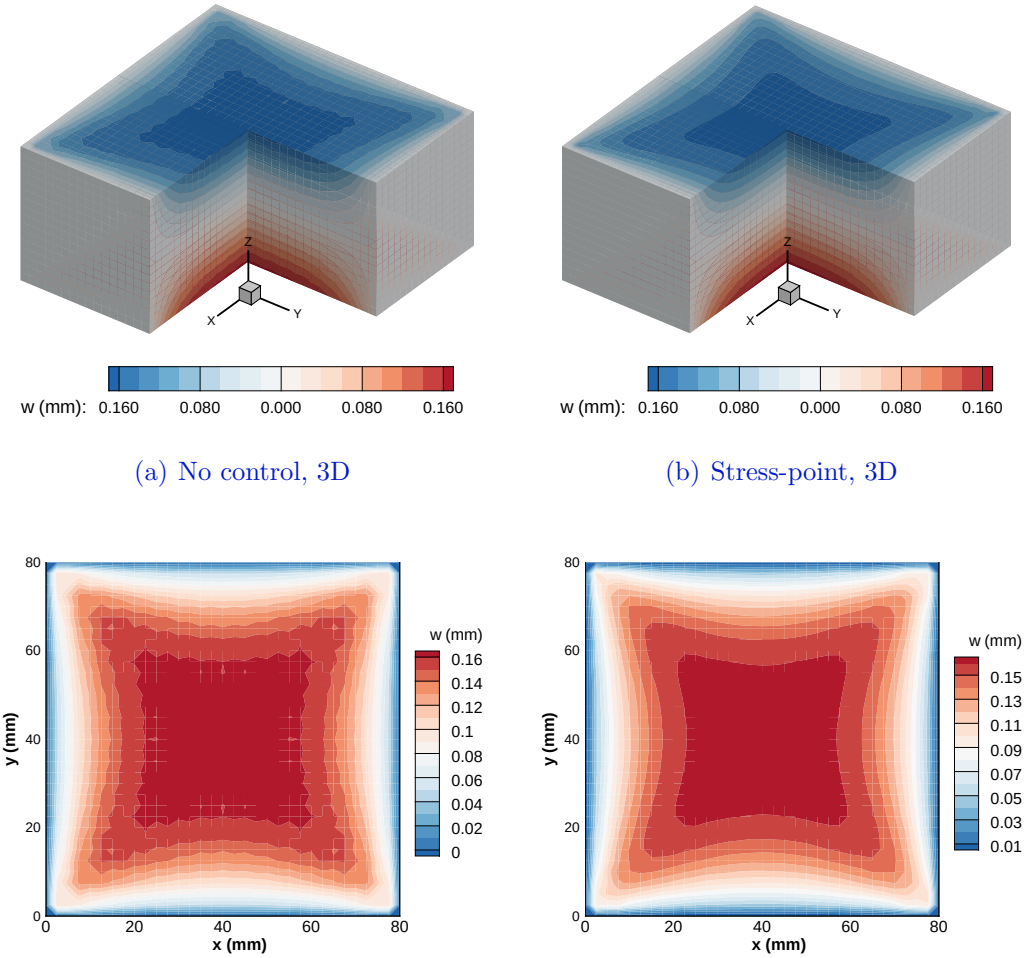

(a) No control, 3D

(b) Stress-point, 3D

(c) No control, bottom

(d) Stress-point, bottom

Figure 6.13: *Contours of z-displacement obtained from the peridynamic model with no control of zero-energy modes and the new stress-point approach. (a) and (b) are 3D contours while (c) and (d) are 2D contours of the bottom surface.*

6.4.5 Numerical efficiency test

Finally, a computation efficiency test on the new stress-point peridynamic model is conducted. We performed computational speed tests on three numerical examples including the 1D bar in Section 6.4.1, the 2D plate in Section 6.4.2, and the 3D brick in Section 6.4.4. Parallel computation was disabled and examples are run in serial on a single processor. Three different number of particles are employed in each

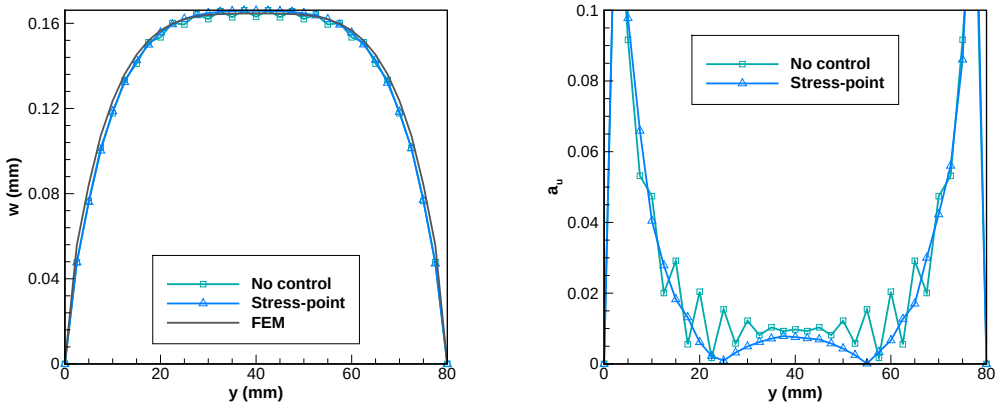

Figure 6.14: *Contours of z-displacement on a selected line located at $x = 40mm$ and $z = 0mm$ varied along y-direction. The peridynamic model with no control of zero-energy modes, the new stress-point approach, and finite–element method (FEM) are applied, respectively.*

example and the convergence criteria are the same with (2.49) as $e_l = 10^{-6}$. Results are shown in Fig. 6.15. Theoretically, the stress-point approach will take double the time compared to the old scheme because a smaller (halved) time step needed to strictly satisfy the stability condition (see Section 6.1). Furthermore, the stress-point peridynamic model has to compute more stress terms in one horizon based on the number of stress points. However, this higher computation cost is balanced by the ability to fully control zero-energy modes.

6.5 Conclusions

A stress-point approach is proposed for the non–ordinary state–based peridynamic correspondence model to fully control zero-energy modes in a nearest neightbor model. We show that by computing two deformation gradients for each particle via splitting its neighborhood, zero-energy-mode oscillations in solutions can be completely damped. The method is first demonstrated in a simple 1D problem and then applied to 2D and 3D examples. In the 1D example, the stress-point approach is compared

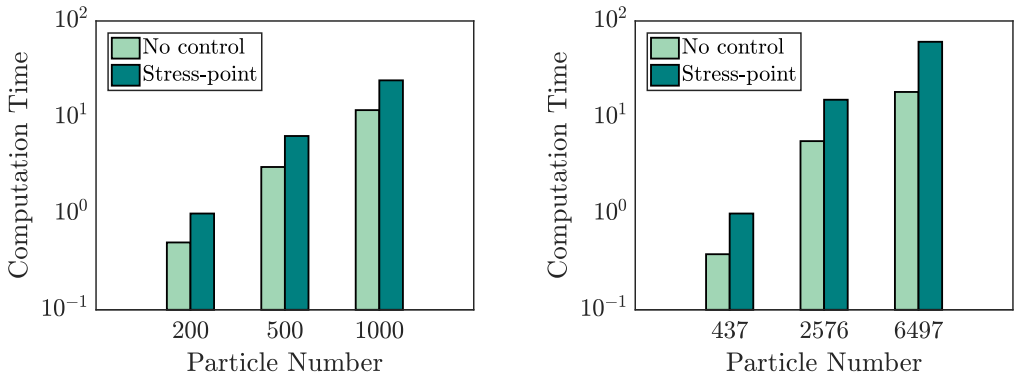

(a) 1D bar

(b) 2D plate

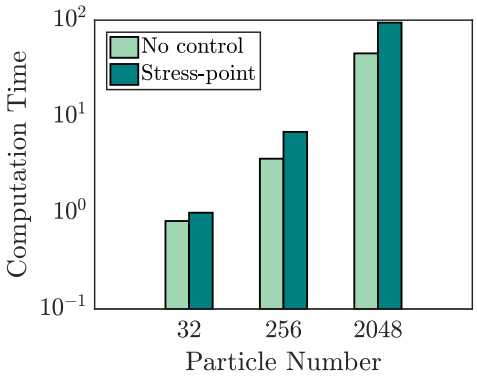

(c) 3D brick

Figure 6.15: *Performance tests between the peridynamic model with no control of zero-energy modes and the stress-point approach. The computation time is normalized by the stress-point case with least particle numbers in each test.*

with analytical solutions and with finite element approach in higher dimensions. The method is demonstrated to be superior to other control methods with introduced supplementary force states. Future work will include extension of this approach to larger horizon sizes and non-linear problems involving plasticity.

CHAPTER VII

Conclusions and Future Work

7.1 Summary

The primary purpose of this dissertation is to propose a 3D peridynamic crystal plasticity model with an adaptive dynamic relaxation solver:

- Chapter II introduces the framework of non-ordinary state-based peridynamics and explicit adaptive relaxation method. This PD-ADRS is first verified in 1D and 3D elastic examples. The flow chart of the algorithm is provided in Section 2.3 and the C++ peridynamic code is attached in Appendix C.

- Chapter III concentrates on 2D planar polycrystal simulations. We examined the use of PD-ADRS algorithm with a rate-independent crystal plasticity model for predicting localizations in crystals. The strain fields and stress-strain response computed by the PD model is compared with those obtained from FEM. Sharper and more numerous strain localizations have been observed in the PD results. In addition, PD-ADRS distinguishes from the implicit solver, which is explained in Section 2.4, for its faster computation speed and feasibility for easier addition of more constitutive models due to the lack of need for computing tangent moduli. The performance of the crystal plasticity is enhanced in our C++ code, which can be seen in Appendix D.

- Chapter IV recognizes the need for dealing with zero energy modes that arises from the use of the correspondence principle for computing deformation gradients. We studied higher-order numerical approximations to deal with the zero-energy modes. As seen in the 1D example, the zero energy mode amplitudes are significantly decreased when using higher order approximations. We also explained the boundary treatment to apply conventional boundary conditions in the PD model by introducing shadow particle layers whose thicknesses are equal to the horizon radius. By using this approach, we showed that consistent and stabilized PD results can be achieved in crystal plasticity within a range of different horizon sizes.

- Chapter V is subdivided into two parts and provides the first 3D implementation of crystal plasticity using peridynamics theory. Part 1 certifies the CPPD model in computing the texture of FCC and HCP 3D polycrystals under two different compression deformation modes. Two horizon sizes are employed to investigate the displacement and strain field of the 3D polycrystal cube. Part 2 investigates the PD solutions with a recent DIC experiment of uniaxial tension in Magnesium WE43 alloy. Finer localization bands are found in the PD results compared with FEM. Two samples of the input files to create a 3D cube domain or a thin layer are provided in Appendix E.

- Chapter VI proposes a stress-point method to fully suppress zero-energy modes in a nearest-neighbor PD family. The stress-point approach is compared with analytical solutions in the 1D example and verifies with the finite element method in higher dimensions. This stress-point PD method is demonstrated superior to other control methods with introduced supplementary force states and we show that it can be used to completely damp the zero energy modes albeit with a larger computational cost than the higher order approximation

explained in the previous chapters.

The C++ source code will be integrated in the PRISMS crystal plasticity family [133] to enable more comprehensive crystal plasticity simulations of localization phenomena. The approach can also be used to validate the mechanical responses of synthetically reconstructed microstructures [115, 134, 135, 136, 137] using the image pixels or voxels as the particle grid.The future work envisaged for this effort is listed below.

7.2 Damage and Contact Models

Since peridynamics theory was originally developed to deal with phenomena such as damage and fracture, attempts for incorporating classical continuum damage models into peridynamics have been made in recent studies [138, 91]. The basic idea in continuum damage mechanics is to represent the damage state by means of a damage variable and then to formulate an equation describing the development and mechanical behavior of the damaged material using this damage variable [139, 140].

The simplest way is to define a positive scalar ω_{D} as

$$\omega_{\mathrm{D}} = S_{\mathrm{D}}/S, \tag{7.1}$$

where S_{D} represents the defect area in the considered plane while S is the total area. Instead of the standard uniaxial stress $\sigma = F/S$, the effective stress becomes

$$\tilde{\sigma} = \frac{F}{S - S_{\mathrm{D}}} = \frac{\sigma}{1 - \omega}. \tag{7.2}$$

However, a direct implementation of damage models within the state-based peridynamics will lead to instabilities associated with unphysical diffusion of the damage zone [138]. Another issue brought in is the inapplicability of the inverse of shape

tensors as a result of breaking bonds in a defect horizon. Hence, a peridynamic bond degradation criterion based on the accumulated material damage is introduced in [138]. A brief introduction is given below.

Consider an effective influence function of the form

$$\tilde{\omega} = \omega \times \omega_{\mathrm{D}}(D), \tag{7.3}$$

where ω is the conventional influence function, $\omega_{\mathrm{D}}(D)$ is a non-increasing function between 0 and 1, and D is an accumulated damage parameter. When $\omega_{\mathrm{D}} = 1$, materials are in a continuum state; when $\omega_{\mathrm{D}} = 0$, the bonds between particles are set to be broken and discontinuities arise.

A specific form of ω_{D} is

$$\omega_{\mathrm{D}} = \begin{cases} 0 & D > D_{\mathrm{c}} \\ 1 & \text{otherwise} \end{cases}, \tag{7.4}$$

and the key becomes to find the most appropriate function incorporating the parameter D. Different damage models such as Johnson-Cook damage model [138] have been tried, which includes the effect of the plastic shearing rate and Von Mises equivalent stress.

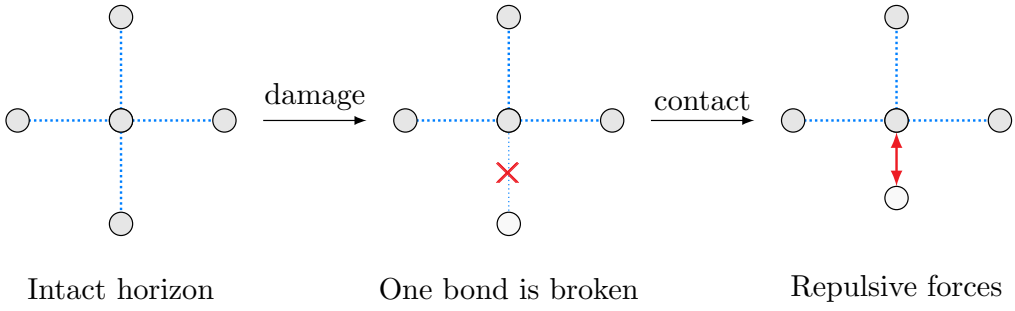

Figure 7.1: *Illustration of a contact model. One bond is broken due to accumulated damage. Contact forces, or repulsive forces, are added when two non-interacting particles become too close.*

In the peridynamic model we discussed so far, particles interact only through their bond forces. If the bond between two particles is broken due to accumulated damage, these two particles may become closer and, finally, interpenetration of material occurs [141]. As illustrated in Fig. 7.1, it is necessary to introduce contact forces when non-interacting particles become too close. We can add an extra bond force in (2.44) as the following:

$$\mathbf{f}_{\mathrm{S}}(\mathbf{y}_p, \mathbf{y}_q) = \min\Big\{0, S_{pq}\big(\|\mathbf{y}_p - \mathbf{y}_q\| - d_{pq}\big)\Big\}\frac{\mathbf{y}_p - \mathbf{y}_q}{\|\mathbf{y}_p - \mathbf{y}_q\|}, \tag{7.5}$$

where $\mathbf{y}_p$ and $\mathbf{y}_q$ represent the locations of particle p and q in the current configuration, respectively, d_{pq} is a *short-range interaction distance* between particles p and q, and S_{pq} is a selected constant [142]. For the short-range interaction distance, we can choose

$$d_{pq} = \min\big\{0.9\|\mathbf{x}_p - \mathbf{x}_q\|, \gamma\big\}, \tag{7.6}$$

where $\mathbf{x}_p$ and $\mathbf{x}_q$ represent the locations of particle p and q in the reference configuration, respectively, γ is a constant related to the lattice size [142]. Note that the short-range force is always repulsive and appears only when particles are under compression.

In the future work, damage and contact models can be added in the new CPPD model. Past efforts have relied on various crack initiation criteria and crack path search algorithms for performing crack prediction in polycrystalline materials [143, 144] while peridynamics is expected to evolve the cracks naturally. The primary challenge here is the need for higher order discretization to ensure that the deformation gradients can be computed even with weakened horizons where some bonds have been broken. A procedure to reestimate the influence functions for various damage scenarios may prove useful. Multiscale extension of the work where peridynamics is used to model localized regions where damage occurs and continuum plasticity is used in the

far field [145] is also of future interest.

7.3 Microstructural Factors Affecting Deformation

Stress development in Mg alloy microstructures are sensitive to the polar nature of twin deformation, texture, and loading. Simulations for different sample orientations and initial texture for gaining improved understanding of localization patterns should be performed. A detailed study of the effect of influence function and the degree of non-locality of particles on the localization patterns should be carried out.

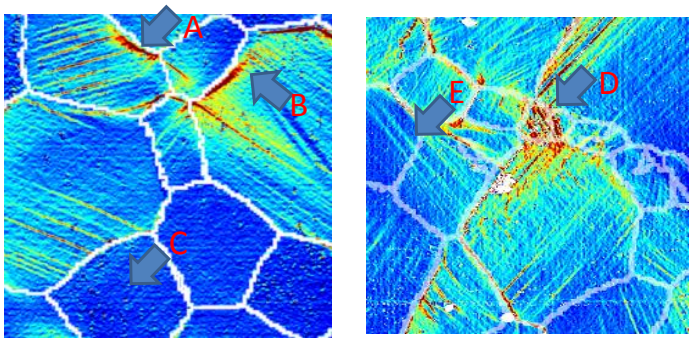

Figure 7.2: *Localization features seen in SEM–DIC of WE43–T5 alloy tension test: Grain boundaries act as barriers to slip transmission in places marked A and B. Grain C is a low Schmid factor grain and shows no localizations. Grain D is a smaller grain and has developed intense strains. Case E shows easy slip transmission across a grain boundary.*

Effects such as non-uniform lattice rotations along localization and the effect of latent hardening parameters on non-Schmid localization behavior should be the focus of future computational studies. Both symmetric and non-symmetric loading should be considered and formation of various kinds of localization including slip bands, kink bands, and non-crystallographic bands should be studied.

Grain boundaries play an important role in polycrystal plasticity, for example, by acting as obstacles to dislocation motion, as sources to new dislocations and as sinks for dislocation annihilation [146, 147, 148]. Grain boundaries are subject to high local

stresses and pile ups that can initiate cracks. Grain boundaries are not explicitly modeled in conventional crystal plasticity, and the interaction between crystal plasticity and grain boundaries is complex and an ongoing topic of research [149, 150]. Since, peridynamics is a non-local model, some basic GB functionalities such as size effect can be simulated by considering the non-local interactions [151, 152, 153] across the grain boundary. DIC data for tensile loading in Magnesium shows several interesting grain boundary–slip band interactions (Fig. 7.2).

The data indicates that the ease of slip transmission across grain boundaries depend upon the 3D geometry incoming slip plane and the grain boundary. The transmission also depends on the critical stresses on incoming and outgoing slip planes across adjacent grains. Some of these effects are shown in Fig. 7.2. Cases of easy transmission and grain boundary blocking are shown. During easy transmission, slip bands glide through the grain boundary under low resolved shear stresses. In the case of a high and low Schmid factor grain boundary, dislocations can only pass through under very high stresses generally arising from dislocation piling up. In addition, small grains favorably oriented for slip develop high stresses compared to the larger grains. One of the goals should be to understand the grain boundary behavior in the context of changing non-local horizon and influence functions at a grain boundary.

In DIC data, strain localization progresses in the form of a laminated pattern. The lamellae bear a relationship with slip direction, and the traces drawn along the lamellae can be correlated to the slip systems in play during loading. Fig. 7.2(a) depicts the experimentally characterized slip traces from DIC data using a geometric analysis. The active slip systems will be identified in peridynamics model using relative activity of each system (e.g. Fig. 7.2(b) for basal system). This plot contains the local changes in activity for each slip/twin system within the grains. The geometric relationship of the localization patterns observed in peridynamics will be compared against the predicted slip/twin activity. All components of the strain tensor (y-strain

and xy-shear) predicted by peridynamics will be compared against the DIC data. These strains may display localization in regions that are different from those seen in the x-strain contours. DIC slip bands of all three basal systems are coincident and hard to distinguish. Similarly, several of the prismatic and pyramidal traces can be nearly parallel to each other. Using peridynamics, we plan to computationally (rather than geometrically) differentiate between these traces. Classification of these localization patterns will be performed into twin bands, slip bands, shear bands and kink bands. Slip bands are the most common and appear along the glide direction at low to moderate strains. Kink bands that are perpendicular to the glide direction have also been reported in literature [154]. Kink banding is associated with strong lattice rotation whereas slip banding generally has a smaller effect depending on boundary constraints. If multiple slip occurs inside a localization band, the more general term shear band will be used. 3D localization analysis should be performed in order to see reorientations and activation of multiple slip systems within a band.

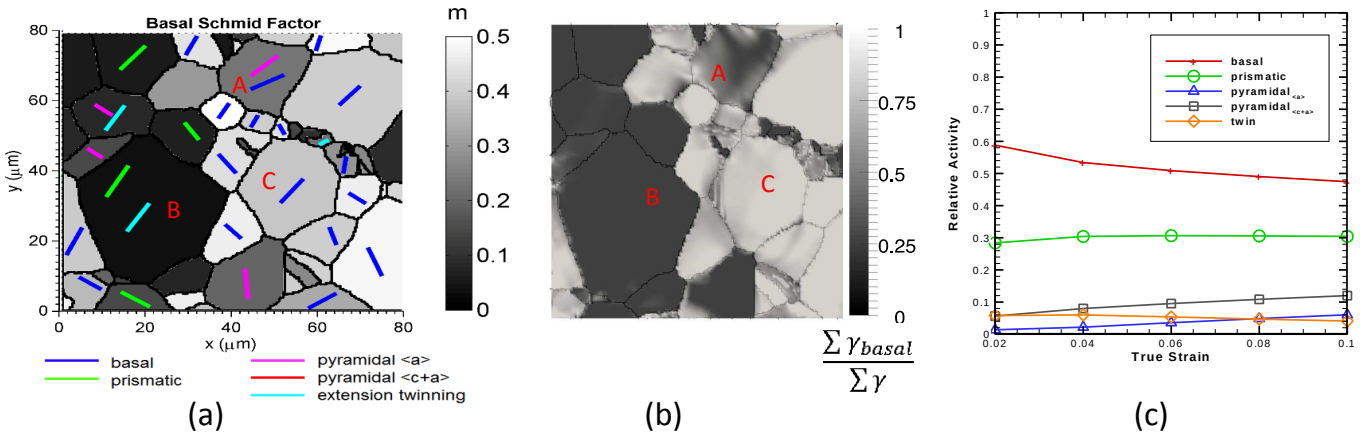

Figure 7.3: *(a) Traces of localization (both slip and twin) as obtained from the in-situ data under tension for a WE43-T5 microstructure. (b) Predicted basal activity from finite element shows regions of high basal activity largely correspond to measured traces (c) Relative activity of various slip and twin systems under tension as a function of strain.*

There are grains where multiple slip systems can be active, that is, the grain is partitioned into sections where basal system is either highly active and inactive.

These grains have multi-slip interactions, are sensitive to latent hardening parameters and are interesting case–studies for intragranular misorientation development [155]. Recent experiments [156] also indicate that misorientations initiate in the form of lamellae of localized strain that eventually merge to form larger localized structures. To test this aspect, time evolution of misorientations within bands may be studied as a function of strain to identify relationships, if any, between grain, grain boundary features and the slip/twin geometry.

APPENDICES

APPENDIX A

Crystal Plasticity Constitutive Update Scheme

All quantities below are described in the local crystal frame. Quantities at the current time step are denoted by subscript $(n+1)$. The deformation gradient $\mathbf{F}_{n+1}$ at the current time step is known before hand. The update procedure below is applied on numerically computing the PK-I stress $\mathbf{P} = \mathcal{F}(\mathbf{F}_{n+1})$, where the operator function $\mathcal{F}$ is the constitutive model.

An Euler-backward time integration scheme for (3.1) leads to the following approximation with the assumption that $\Delta\gamma$ is small:

$$\mathbf{F}^{\mathrm{p}} = \exp\Big(\Delta t \sum_{\alpha} \dot{\gamma}^{\alpha} \mathbf{S}_0^{\alpha} \mathrm{sign}(\tau^{\alpha})\Big)\mathbf{F}_n^{\mathrm{p}} \approx \Big(\mathbf{I} + \sum_{\alpha} \Delta\gamma^{\alpha} \mathbf{S}_0^{\alpha} \mathrm{sign}(\tau^{\alpha})\Big)\mathbf{F}_n^{\mathrm{p}}. \tag{A.1}$$

Substitute (A.1) into the multiplicative decomposition $\mathbf{F} = \mathbf{F}^{\mathrm{e}}\mathbf{F}^{\mathrm{p}}$ and reform the equation:

$$\mathbf{F}^{\mathrm{e}} = \mathbf{F}^{\mathrm{e}}_{\mathrm{trial}}\Big(\mathbf{I} - \sum_{\alpha} \Delta\gamma^{\alpha} \mathbf{S}_0^{\alpha} \mathrm{sign}(\tau^{\alpha})\Big), \tag{A.2}$$

where $\mathbf{F}^{\mathrm{e}}_{\mathrm{trial}} = \mathbf{F}_{n+1}(\mathbf{F}_n^{\mathrm{p}})^{-1}$is the trial elastic deformation gradient. At the first time step, $\mathbf{F}_0^{\mathrm{p}}$ is initialized as the identity tensor $\mathbf{I}$. The Green elastic strain measure is

computed using (A.2) as

$$\bar{\mathbf{E}}^{e} = \frac{1}{2}\big(\mathbf{F}^{\mathrm{e}\mathrm{T}}\mathbf{F}^{\mathrm{e}} - \mathbf{I}\big) = \bar{\mathbf{E}}^{e}_{\mathrm{trial}} - \frac{1}{2}\sum_{\alpha}\Delta\gamma^{\alpha}\mathbf{B}^{\alpha}\mathrm{sign}(\tau^{\alpha}), \tag{A.3}$$

where $\bar{\mathbf{E}}^{e}_{\mathrm{trial}}$ and $\mathbf{B}^{\alpha}$ are defined as

$$\bar{\mathbf{E}}^{e}_{\mathrm{trial}} = \frac{1}{2}\Big((\mathbf{F}^{\mathrm{e}}_{\mathrm{trial}})^{\mathrm{T}}\mathbf{F}^{\mathrm{e}}_{\mathrm{trial}} - \mathbf{I}\Big), \tag{A.4}$$

$$\mathbf{B}^{\alpha} = (\mathbf{S}^{\alpha}_{0})^{\mathrm{T}}(\mathbf{F}^{\mathrm{e}}_{\mathrm{trial}})^{\mathrm{T}}\mathbf{F}^{\mathrm{e}}_{\mathrm{trial}} + (\mathbf{F}^{\mathrm{e}}_{\mathrm{trial}})^{\mathrm{T}}\mathbf{F}^{\mathrm{e}}_{\mathrm{trial}}\mathbf{S}^{\alpha}_{0}. \tag{A.5}$$

Using (A.3) in the constitutive relation for conjugate stress $\bar{\mathbf{T}} = \mathcal{L}^{\mathrm{e}}[\bar{\mathbf{E}}^{\mathrm{e}}]$ leads to the following:

$$\bar{\mathbf{T}} = \bar{\mathbf{T}}_{\mathrm{trial}} - \frac{1}{2}\sum_{\alpha}\Delta\gamma^{\alpha}\mathcal{L}^{\mathrm{e}}[\mathbf{B}^{\alpha}]\mathrm{sign}(\tau^{\alpha}_{\mathrm{trial}}), \tag{A.6}$$

where $\bar{\mathbf{T}}_{\mathrm{trial}} = \mathcal{L}^{\mathrm{e}}[\bar{\mathbf{E}}^{\mathrm{e}}_{\mathrm{trial}}]$.

A trial resolved shear stress $\tau^{\alpha}_{\mathrm{trial}} = \bar{\mathbf{T}}_{\mathrm{trial}} : \mathbf{S}^{\alpha}_{0}$ is then computed. A potentially active set $\mathcal{PA}$ of slip systems can be identified based on the trial resolved stress as the systems with $|\tau^{\alpha}_{\mathrm{trial}}| - s^{\alpha} > 0$.

During plastic flow, the active systems are assumed to follow the consistency condition: $|\tau^{\alpha}| = s^{\alpha}$. Increment in shearing rates $\Delta\gamma^{\beta}$ at each time step is obtained by solving the following equation obtained by resolving (A.6) along slip directions:

$$|\tau^{\alpha}| = s^{\alpha} = |\tau^{\alpha}_{\mathrm{trial}}| - \frac{1}{2}\mathrm{sign}(\tau^{\alpha}_{\mathrm{trial}})\Big(\sum_{\beta}\Delta\gamma^{\beta}\mathcal{L}^{\mathrm{e}}[\mathbf{B}^{\beta}]\mathrm{sign}(\tau^{\beta}_{\mathrm{trial}})\Big) : \mathbf{S}^{\alpha}_{0}, \tag{A.7}$$

where $\alpha, \beta \in \mathcal{PA}$.

A system of equations is obtained of the following form:

$$\sum_{\beta\in\mathcal{PA}} A^{\alpha\beta}\Delta\gamma^{\beta} = b^{\alpha}, \tag{A.8}$$

where

$$A^{\alpha\beta} = h^{\alpha\beta} + \frac{1}{2}\text{sign}(\tau^{\alpha}_{\text{trial}})\text{sign}(\tau^{\beta}_{\text{trial}})\mathcal{L}^{\text{e}}[\mathbf{B}^{\beta}] : \mathbf{S}^{\alpha}_{0},$$

$$b^{\alpha} = |\tau^{\alpha}_{trial}| - s^{\alpha}. \tag{A.9}$$

If for any system $\Delta\gamma^{\beta} \leq 0$, then this system is removed from the set of potentially active systems. The system is repeatedly solved until for all systems $\Delta\gamma^{\beta} > 0$.

APPENDIX B

Stress-Point Approach Stability Analysis

The impact of zero-energy modes, manifesting as numerical oscillations and serrated contours, is conspicuous in Figs. 2.9 and 2.10. This inherent stability issue is a result of the weak couplings between particles. In order to better understand the essential characteristics such as accuracy and convergence of the PD numerical discretization scheme, a concise stability analysis on a 1D problem is conducted below.

Typically, wave motions in solid mechanics are modeled by hyperbolic partial differential equations [7, 100]. Assume a 1D bar is elastic under small deformation, and ignore the body force and damping ratio, the equation of motion can be expressed by displacement u as

$$\frac{\partial^2 u}{\partial t^2} = \frac{1}{\rho}\frac{\partial \sigma}{\partial x} = c_{\mathrm{s}}^2 \frac{\partial^2 u}{\partial x^2} \tag{B.1}$$

where $c_{\mathrm{s}} = \sqrt{E/\rho}$ is the speed of sound; E and ρ are the Young's modulus and density, respectively.

In a discrete system with totally N particles, let u_j^n indicate the displacement component of particle j at time $t = n\Delta t$, where Δt is the time step assumed constant, and $\mathbf{u}^n = [u_1^n, u_2^n, \ldots, u_N^n]$ be the displacement vector at $t = n\Delta t$. With a central difference discretization at time and a peridynamic discrete operator $\mathcal{A}$ at space,

(B.1) turns into

$$\frac{\mathbf{u}^{n+1} - 2\mathbf{u}^n + \mathbf{u}^{n-1}}{(\Delta t)^2} = \mathcal{A}(\mathbf{u}^n). \tag{B.2}$$

No-Control Scheme

Follow on the discretization scheme (2.44) in Chapter 2.3, the peridynamic operator can be rewritten as an explicit matrix form, i.e., $\mathcal{A}(\mathbf{u}^n) = \mathbf{A}_1\mathbf{u}^n$, with

$$\mathbf{A}_1 = \frac{c_{\mathrm{s}}^2}{4(\Delta x)^2}\begin{bmatrix} \dots & & & & \dots & & & \dots \\ \dots & 1 & 0 & -2 & 0 & 1 & & \dots \\ \dots & & 1 & 0 & -2 & 0 & 1 & \dots \\ \dots & & & 1 & 0 & -2 & 0 \quad 1 & \dots \\ \dots & & & & \dots & & & \dots \end{bmatrix}. \tag{B.3}$$

Consequently, it becomes a standard initial value problem for hyperbolic systems. Modified equations analysis is an illuminating approach to reveal stability behaviors of the numerical solution [100]. The main idea of modified equations analysis is to find another partial differential equation which is approximated better by current discretization scheme. By doing Taylor series expansions, the modified equation of (B.2) is calculated as

$$\frac{\partial^2 u}{\partial t^2} - c_{\mathrm{s}}^2\frac{\partial^2 u}{\partial x^2} = -\frac{1}{12}c_{\mathrm{s}}^2(\Delta x)^2\Big[\mu_{\mathrm{c}}^2 - 4\Big]\frac{\partial^4 u}{\partial x^4} + \cdots \tag{B.4}$$

where $\mu_{\mathrm{c}} = c_{\mathrm{s}}\frac{\Delta t}{\Delta x}$ is the Courant or CFL number. Thus, (B.4) is the partial differential equation better approximated by (B.2). Based on the right side of (B.4), this numerical scheme is a second order accurate approximation to the true solution of (B.1). In addition, the leading term leads to a diffusion behavior.

The stability condition to avoid ill-posed problem, necessary but not sufficient, is

$$\mu_{\rm c}^2 - 4 \leq 0 \Longrightarrow \Delta t \leq 2\Delta x/c_{\rm s}. \tag{B.5}$$

Therefore, the critical time step is $\Delta t_c = 2\Delta x/c_{\rm s}$. Yet, when extended to higher dimensions, the critical time step should change correspondingly and, basically, it is more constrained in higher dimensions. For example, in 2D problems, the critical time step is reduced to $\Delta t_c = \Delta x/c_{\rm s}$, which is the same as (2.41) in Chapter 2.2.

The main reason for instability is the weak coupling of particle displacements to strains. A new scheme described next solves the issue.

Stress-Point Scheme

Motivated by the stress-point approach for tension instability in smoothed Particle Hydrodynamics methods [94], and its similarity to PD [132], a new scheme is proposed and explained below.

Based on (6.3) and (B.5), the peridynamic space operator in (B.2) can be expressed as a new explicit matrix production, i.e., $\mathcal{A}(\mathbf{u}^n) = \mathbf{A}_2\mathbf{u}^n$, with

$$\mathbf{A}_2 = \frac{c_{\rm s}^2}{(\Delta x)^2}\begin{bmatrix} \dots & & & \dots & & & \dots \\ \dots & 1 & -2 & 1 & & & \dots \\ \dots & & 1 & -2 & 1 & & \dots \\ \dots & & & 1 & -2 & 1 & \dots \\ \dots & & & \dots & & & \dots \end{bmatrix}, \tag{B.6}$$

which is more compact than $\mathbf{A}_1$ in (B.3). The modified equation for the new scheme becomes

$$\frac{\partial^2 u}{\partial t^2} - c_{\rm s}^2\frac{\partial^2 u}{\partial x^2} = -\frac{1}{12}c_{\rm s}^2(\Delta x)^2\Big[\mu_{\rm c}^2 - 1\Big]\frac{\partial^4 u}{\partial x^4} + \cdots \tag{B.7}$$

with the stability condition

$$\mu_{\mathrm{c}}^2 - 1 \leq 0 \Longrightarrow \Delta t \leq \Delta x / c_{\mathrm{s}}. \tag{B.8}$$

Theoretically, this new scheme enhances the connections between particles and preserves the second order of accuracy at the same time. However, the critical time step is reduced to a half of the old scheme. Moreover, the computation cost is doubled since the stress at each particle is supposed to be calculated twice.

It is notable that Von Neumann analysis, another powerful stability analysis method [100, 157], produces the exactly same stability condition as (B.5) and (B.8). If necessary, a phase analysis on dispersion can be conducted in the future research.

APPENDIX C

Peridynamics Core Function

```
/*-------------------------------------------------------------------
Peridynamics: solve the equation of motion dotdot{u} + Ku = 0
-------------------------------------------------------------------*/
void MyEquation::peridynamics()
{
    double vf = vperatom;  //particle volume
    int i, j, ii, nodeID, i_proc;  //c++ loop index

    //MPI: pass the new position vector
    //boundary condition is forced inside the function
    newpos_comm_MPIfunc();

    //compute the deformation gradient
    defgradient();
    //deformation gradient values at shadow points
    for (i = 0; i < siz_SP; i++) {
        nodeID = particleID_SP[i];
        F[nodeID] = F_sp;
    }

    //compute PKI stress P_i by the constitutive model
    ArrayXd P_i;
    double *s_alpha_t_i = new double [siz_slips]();
    for (i_proc = 0; i_proc < np_proc; i_proc++) {
        //i_box_proc stores the particle ID in the current processor
        i = i_box_proc[i_proc + myid * np_proc];
        //parameter initialization
        for (j = 0; j < siz_slips; j++) {
```

```
            ii = i* siz_slips + j;
            s_alpha_t_i[j] = s_alpha_t[ii];
        }

        //constitutive model function, output is an Eigen array
        P_i = constitutive(F[i], Fp_t[i], Fe_t[i],
            s_alpha_t_i, Rotmat[i], Schmid_Tensor,
            h_alpha_beta_t, Dmat, siz_slips, siz_twins, 0);

        //outputs collect/gather
        int matrix_siz = dim * dim;
        for (j = 0; j < matrix_siz; j++) {
            //P, column-major order
            ii = j + i * matrix_siz;
            P_temp[ii] = P_i(j);
        }
    }
    delete[] s_alpha_t_i;

    //MPI: pass the PKI stress matrix
    P_comm_MPIfunc();

    Vector3d xi, ke;
    Matrix3d Ki, Kj;  //shape tensor Ki and Kj
    int s, list;      //c++ loop index
    double ome = 0.;  //omega, influence function

    for (i_proc = 0; i_proc < np_proc; i_proc++) {
        i = i_box_proc[i_proc + myid * np_proc];
        ke.setZero();
        //Ki = Kinv[i] or a constant
        Ki = Kconst;
        for (s = 0; s < neighbors[i]; s++) {
            list = neighborlist[i*Nb + s];
            for (j = 0; j < dim; j++) {
                xi(j) = initpos[list*dim + j]
                    - initpos[i*dim + j];
            }
            ome = omega(xi.data());
            //Kj = Kinv[list], or a constant
            Kj = Ki;
            ke.noalias() += ome * vf * (PKI[list] * Kj
                + PKI[i] * Ki) * xi;
        }
```

```
    for (j = 0; j < dim; j++) {
        ii = i*dim + j;
        Ku[ii] = ke(j);
    }
}

//Adaptive Dynamic Relaxation Solver (ADRS)
double k_local = 0., U_square = 0.;
double k_local_sum = 0., U_square_sum = 0.;
if (t_dynamics >= dt) {
    //start at the second virtual time step
    for (i_proc = 0; i_proc < np_proc; i_proc++) {
        i = i_box_proc[i_proc + myid * np_proc];
        for (j = 0; j < dim; j++) {
            ii = i * dim + j;
            //velocity field should not be zero
            if (abs(currentdisp[ii] - olddisp[ii]) >= 1e-10) {
                //diagonal "local" stiffness matrix
                k_local += (Ku_prev[ii] - Ku[ii]) /
                    (currentdisp[ii] - olddisp[ii])
                    * currentdisp[ii] * currentdisp[ii];
            }
            U_square += currentdisp[ii] * currentdisp[ii];
        }
    }
    MPI_Allreduce(&k_local, &k_local_sum, 1, MPI_DOUBLE,
        MPI_SUM, MPI_COMM_WORLD);
    MPI_Allreduce(&U_square, &U_square_sum, 1, MPI_DOUBLE,
        MPI_SUM, MPI_COMM_WORLD);
    //new damping ratio, U_square is always >= 0.
    damp = -2.*sqrt(abs(k_local_sum) / U_square_sum);
}

//Dynamics: central difference scheme
double d_t = dt;
double Damp = damp / d_t, Mass = mass / d_t / d_t;
double *new_disp = new double[np*dim];

for (i_proc = 0; i_proc < np_proc; i_proc++) {
    i = i_box_proc[i_proc + myid * np_proc];
    for (j = 0; j < dim; j++) {
        ii = i * dim + j;
        acceleration[ii] = Ku[ii] / mass;

        //Initialize the first step
```

```
            if (t_dynamics == 0.) {
                velocity[ii] = 0.;
                olddisp[ii] = currentdisp[ii] - velocity[ii] * d_t +
                    acceleration[ii] * d_t*d_t / 2.;
            }

            new_disp[ii] = (Ku[ii] + 2.*Mass*currentdisp[ii]
                - (Damp / 2. + Mass)*olddisp[ii])
                / (-Damp / 2. + Mass);
            velocity[ii] = (new_disp[ii] - olddisp[ii]) / 2. / d_t;
            olddisp[ii] = currentdisp[ii];
            currentdisp[ii] = new_disp[ii];

            //update error_Ku
            Ku_prev[ii] = Ku[ii];
        }
    }

    //force the boundary condition
    for (i = 0; i < siz_BC * dim; i++) {
        currentdisp[essBC1[i]] = essBC2[i];
    }

    //update the virtual dynamic time step
    t_dynamics += dt;

    delete[] new_disp;
}
```

APPENDIX D

Crystal Plasticity Constitutive Model Code for PD-ADRS

```
/*-------------------------------------------------------------
Enhanced crystal plasticity constitutive model
Inputs: F (3 x 3), deformation gradient;
        Fp_t (3 x 3), deformation gradient plastic part;
        Fe_t (3 x 3), deformation gradient elastic part;
        s_alpha_t (siz_slips x 1), slip resistance;
        rotmat (3 x 3), rotation matrix;
        Schmid_Tensor (3 x 3, siz_slips), Schmid factor;
        h_alpha_beta_t (siz_slips x siz_slips), initial hardening
   coefficients;
        Dmat (1 x 6), stiffness in vector format;
        siz_slips, number of slip systems;
        siz_twins, number of twin systems;
        short/long outputs O = 0/1
Return: Eigen array outputs (size depends on O)
-------------------------------------------------------------*/
ArrayXd constitutive(const Matrix3d &F, const Matrix3d &Fp_t,
    const Matrix3d &Fe_t, const double s_alpha_t[],
    const Matrix3d &rotmat, const Matrix3d *Schmid_Tensor,
    const double h_alpha_beta_t[], const double Dmat[],
    const int siz_slips, const int siz_twins, const int O)
{
    int i, j, ii;          //c++ loop indices
    int dim = 3;           //dimension = 3
    Matrix3d eye = Matrix3d::Identity();  //identity matrix, I
```

```
Matrix3d F_tau, temp, rot_inv;
rot_inv = rotmat.transpose();
F_tau.noalias() = rot_inv * F * rotmat;
//.noalias() is used for speed-up (Eigen library function)

/*----------- Step 1 -----------*/
Matrix3d Fe_tau_trial, Ce_tau_trial, Ee_tau_trial;
Fe_tau_trial.noalias() = F_tau * Fp_t.inverse();
temp = Fe_tau_trial.transpose();
Ce_tau_trial = temp * Fe_tau_trial;
Ee_tau_trial = 0.5*(Ce_tau_trial - eye);

/*----------- Step 2 -----------*/
Matrix3d T_star_tau_trial;
//.data() is the address of the Eigen variable
T_star_tau_trial = Dmatmul_pointer(Dmat, Ee_tau_trial.data());

/*----------- Step 3 -----------*/
int *PA = new int [siz_slips](); //active slip systems
int nPA = 0;    //number of active slip systems
double *b = new double[siz_slips]();
double *resolved_shear_tau = new double [siz_slips]();
double *resolved_shear_tau_trial = new double [siz_slips]();

for (i = 0; i < siz_slips; i++)
{
    resolved_shear_tau_trial[i] =
        Energy_product_pointer(T_star_tau_trial.data(),
Schmid_Tensor[i].data());

    /*----------- Step 4 -----------*/
    b[i] = abs(resolved_shear_tau_trial[i]) - s_alpha_t[i];
    if (i < siz_slips - siz_twins) { //normal slip systems
        if (b[i] >= 0.) {
            nPA++;
            PA[nPA - 1] = i; //potentially active slip systems
        }
    }
    else  //twinning systems
    {
        if (b[i] >= 0. && resolved_shear_tau_trial[i] > 0) {
            nPA++;
            PA[nPA - 1] = i; //potentially active slip systems
        }
```

```
    }
    resolved_shear_tau[i] = abs(resolved_shear_tau_trial[i]);
}

/*----------- Step 5 -----------*/
double *A = new double [siz_slips * siz_slips]();

//Most expensive loop for the explicit solver
Matrix3d symm, symm1, symm2;
double L1, L2;
for (j = 0; j < siz_slips; j++) {
    symm1.noalias() = Ce_tau_trial * Schmid_Tensor[j];
    temp = symm1.transpose();
    temp += symm1;
    symm2 = 0.5*temp;
    symm = Dmatmul_pointer(Dmat, symm2.data());
    for (i = 0; i < siz_slips; i++) {
        L1 = Energy_product_pointer(Schmid_Tensor[i].data(),
            symm.data());
        L2 = resolved_shear_tau_trial[i]
            * resolved_shear_tau_trial[j];
        ii = i * siz_slips + j;
        if (L2 > 0.)
            A[ii] = h_alpha_beta_t[ii] + L1;
        else
            A[ii] = h_alpha_beta_t[ii] - L1;
    }
}

//update data information
Matrix3d Fp_tau = Fp_t;
double *s_alpha_tau = new double [siz_slips]();
for (i = 0; i < siz_slips; i++) {
    s_alpha_tau[i] = s_alpha_t[i];
}
Matrix3d Fe_tau, T_tau, PK1;
Fe_tau.noalias() = F_tau * Fp_tau.inverse();
temp = Fe_tau.transpose();
T_tau.noalias() = Fe_tau * T_star_tau_trial * temp
    / Fe_tau.determinant();
temp = F_tau.transpose();
PK1.noalias() = F_tau.determinant() * T_tau * temp.inverse();

double *x_beta = new double [siz_slips]();
if (nPA > 0) {
```

```
        //remove inactive slip systems
        INACTIVE_SLIP_REMOVAL(A, b, PA, nPA, siz_slips, x_beta);

        /*----------- Step 6 -----------*/
        for (i = 0; i < siz_slips; i++) {
            L1 = x_beta[i] * sign(resolved_shear_tau_trial[i]);
            Fp_tau.noalias() += L1 * Schmid_Tensor[i] * Fp_t;
        }

        /*----------- Step 7 -----------*/
        //L1 = pow(Fp_tau.determinant(), 1. / 3.);
        //Fp_tau /= L1;

        /*----------- Step 8 -----------*/
        Fe_tau.noalias() = F_tau*Fp_tau.inverse();
        Matrix3d T_star_tau;  T_star_tau.setZero();
        for (i = 0; i < siz_slips; i++) {
            temp = Schmid_Tensor[i];
            symm1 = Ce_tau_trial * temp;
            temp = symm1.transpose();
            temp += symm1;
            symm2 = 0.5*temp;
            symm = Dmatmul_pointer(Dmat, symm2.data());

            L1 = x_beta[i] * sign(resolved_shear_tau_trial[i]);
            T_star_tau -= L1 * symm;
        }
        T_star_tau += T_star_tau_trial;

        /*----------- Step 9 -----------*/
        temp = Fe_tau.transpose();
        T_tau.noalias() = Fe_tau * T_star_tau * temp
        / Fe_tau.determinant();
        temp = F_tau.transpose();
        PK1.noalias() = F_tau.determinant() * T_tau * temp.inverse()
    ;

        //update the resistance
        for (i = 0; i < siz_slips; i++) {
            L1 = 0.;
            for (j = 0; j < siz_slips; j++) {
                ii = i * siz_slips + j;
                L1 += h_alpha_beta_t[ii] * x_beta[j];
            }
            s_alpha_tau[i] = s_alpha_t[i] + L1;
```

```
    }
}  //loop end of removal of inactive slip systems

Matrix3d P;
P.noalias() = rotmat * PK1 * rot_inv;

//output
int siz_o = dim * dim;
ArrayXd Output(siz_o);
//only output PKI stress for dynamic iterations
if (O == 0) {
    ii = 0;
    //P, column-major order, PKI stress
    for (j = 0; j < dim; j++) {
        for (i = 0; i < dim; i++) {
            Output(ii) = P(i, j);
            ii++;
        }
    }
}

//output for updatadata function after convergence
else {
    int siz_o = dim*dim*3 + siz_slips*2 + 1 + dim;
    Output.resize(siz_o);
    ii = 0;

    //P, column-major order, PKI stress
    for (j = 0; j < dim; j++) {
        for (i = 0; i < dim; i++) {
            Output(ii) = P(i, j);
            ii++;
        }
    }
    //Fp_tau, column-major order
    for (j = 0; j < dim; j++) {
        for (i = 0; i < dim; i++) {
            Output(ii) = Fp_tau(i, j);
            ii++;
        }
    }
    //Fe_tau, column-major order
    for (j = 0; j < dim; j++) {
        for (i = 0; i < dim; i++) {
            Output(ii) = Fe_tau(i, j);
```

```
            ii++;
        }
    }

    //s_alpha_tau, resistance
    for (i = 0; i < siz_slips; i++) {
        Output(ii) = s_alpha_tau[i];
        ii++;
    }
    //d_gamma, x_beta
    for (i = 0; i < siz_slips; i++) {
        Output(ii) = x_beta[i];
        ii++;
    }

    //de_p
    double slip_energy = 0.;
    for (i = 0; i < siz_slips; i++) {
        for (j = 0; j < siz_slips; j++) {
            symm1.noalias() = Ce_tau_trial * Schmid_Tensor[j];
            symm2 = 0.5*(symm1 + symm1.transpose());
            symm = Dmatmul_pointer(Dmat, symm2.data());
            L1 = Energy_product_pointer(Schmid_Tensor[i].data(),
                symm.data());
            L2 = resolved_shear_tau_trial[i]
                * resolved_shear_tau_trial[j];
            resolved_shear_tau[i] -= sign(L2) * L1 * x_beta[j];
        }
        //sum of tau^alpha * d_gamma^alpha
        slip_energy += x_beta[i] * resolved_shear_tau[i];
    }
    Matrix3d T_p;
    //T_tau is Cauchy stress
    T_p = T_tau - eye * T_tau.trace() / 2.;
    double S_eff = sqrt(1.5 * Energy_product_pointer(T_p.data(),
        T_p.data())); //VM stress
    Output[ii] = slip_energy / S_eff; //de_p
    if (S_eff == 0.) Output(ii) = 0.0;
    ii++;

    //dr, reorientation
    Vector3d dr;
    dr = Reorient(rotmat, Fe_tau, Fe_t);
    for (i = 0; i < dim; i++) {
        Output(ii) = dr(i);
```

```
            ii++;
        }
    }

    delete[] A; delete[] PA; delete[] b; delete[] x_beta;
    delete[] s_alpha_tau; delete[] resolved_shear_tau;
    delete[] resolved_shear_tau_trial;

    return Output;  //Eigen array
}
```

APPENDIX E

Input File Examples

Initialization.input for a 3D cube domain.

```
/--------------- Mesh Parameters -------------/
//xmin, xmax, number of particles between
0.0 3.0 24

/--------------- Dynamics ----------------/
//time step [dx/sqrt(E_max/ro)], initial damping
4e-4 1.0

//max iterations, record frequency, tolerate error
1000 150 1e-5

/-------------- PD Horizon Size -------------/
//if \delta = sqrt(5)*h, then put 5 below
1

/-------------- Boundary Condition -------------/
//strain rate, total loading steps, record frequency
0.001 200 40

//velocity gradient L(3x3)
1 0 0
0 0 0
0 0 -1

/-------------- Output Variables -------------/
//How many variables do you want to output?
```

```
9
//Which ones? please write down their IDs
1 2 3 4 5 7 16 17 18
//Note: u, v, w, e_xx, e_yy, e_xy, reort1x3


/*-------------- Available Variables Table -----------------
//displacement:
    u, v, w (3)
//strain:
    e_xx, e_yy, e_zz, e_xy, e_xz, e_yz (6)
//stress:
    S_xx, S_yy, S_zz, S_xy, S_xz, S_yz (6)
//reorientation:
    reort1, reort2, reort3 (3)
//equivalent plastic strain increment:
    de_p (1)
//slip increment:
    n1 -> n_(siz_slips)
------------------------------------------------------------*/
```

Initialization.input for a DIC thin layer.

```
/--------------- Mesh Parameters -------------/
//number of particles in the x-direction
50

/--------------- Dynamics ----------------/
//time step [dx/sqrt(E_max/ro)], initial damping
0.06 0.5

//max iterations, record frequency, tolerate error
2000 400 1e-5

/-------------- Boundary Condition --------------/
//loading factor (u/500), record frequency, stop loading
500 50 500

/-------------- Output Variables --------------/
//How many variables do you want to output?
9
//Which ones? please write down their IDs
1 2 3 4 5 7 16 17 18
//Note: u, v, w, e_xx, e_yy, e_xy, reort1x3


/*------------- Available Variables Table ----------------
//displacement:
    u, v, w (3)
//strain:
    e_xx, e_yy, e_zz, e_xy, e_xz, e_yz (6)
//stress:
    S_xx, S_yy, S_zz, S_xy, S_xz, S_yz (6)
//reorientation:
    reort1, reort2, reort3 (3)
//equivalent plastic strain increment:
    de_p (1)
//slip increment:
    n1 -> n_(siz_slips)
-------------------------------------------------------*/
```

SlipConstant.input for HCP with 6 twin slip systems

```
//number of slip systems, twinning systems, threshold FT
24 6 0.25

//Magnesium T5(2), C matrix [C11, C12, C13, C33, C44, C66]
59.3e3 25.7e3 21.4e3 61.5e3 16.4e3 16.8e3

//s0, a_cp, h0_cp, s_s_cp,
//basal, prismatic, pyramidal_a, pyramidal_c+a, twinning

76.0 76.0 76.0 163.2 163.2 163.2
160.3 160.3 160.3 160.3 160.3 160.3
187.4 187.4 187.4 187.4 187.4 187.4
116.4 116.4 116.4 116.4 116.4 116.4

1.0 1.0 1.0 1.0 1.0 1.0
1.0 1.0 1.0 1.0 1.0 1.0
1.0 1.0 1.0 1.0 1.0 1.0
1.0 1.0 1.0 1.0 1.0 1.0

225.6 225.6 225.6 124.9 124.9 124.9
120.2 120.2 120.2 120.2 120.2 120.2
237.9 237.9 237.9 237.9 237.9 237.9
105.6 105.6 105.6 105.6 105.6 105.6

248.7 248.7 248.7 356.3 356.3 356.3
347.8 347.8 347.8 347.8 347.8 347.8
350.4 350.4 350.4 350.4 350.4 350.4
238.3 238.3 238.3 238.3 238.3 238.3
```

BIBLIOGRAPHY

BIBLIOGRAPHY

[1] S. Ganesan. *Microstructural response of magnesium alloys: 3D crystal plasticity and experimental validationk*. PhD thesis, University of Michigan, Ann Arbor, 2017.

[2] R. F. S. Hearmon. The elastic constants of crystals and other anisotropic materials. *Landolt-Bornstein Tables, III/18*, page 1154, 1984.

[3] A. V. Staroselsky. *Crystal plasticity due to slip and twinning*. PhD thesis, Massachusetts Institute of Technology, 1998.

[4] A. D. Kammers and S. Daly. Digital image correlation under scanning electron microscopy: methodology and validation. *Experimental Mechanics*, 53(9):1743–1761, 2013.

[5] A. Guery, F. Hild, F. Latourte, and S. Roux. Slip activities in polycrystals determined by coupling DIC measurements with crystal plasticity calculations. *International Journal of Plasticity*, 81:249–266, 2016.

[6] N. A. Fleck and J. W. Hutchinson. Strain gradient plasticity. *Advances in Applied Mechanics*, 33:296–361, 1997.

[7] A. F. Bower. *Applied mechanics of solids*. CRC press, 2009.

[8] G. Liu. *Meshfree methods: Moving beyond the finite element method*. Taylor & Francis, 2009.

[9] S. A. Silling. Reformulation of elasticity theory for discontinuities and long-range forces. *Journal of the Mechanics and Physics of Solids*, 48(1):175–209, 2000.

[10] S. A. Silling, M. Epton, O. Weckner, J. Xu, and E. Askari. Peridynamic states and constitutive modeling. *Journal of Elasticity*, 88(2):151–184, 2007.

[11] E. Askari, F. Bobaru, R.B. Lehoucq, M. L. Parks, S. A. Silling, and O. Weckner. Peridynamics for multiscale materials modeling. In *Journal of Physics: Conference Series*, volume 125, page 012078. IOP Publishing, 2008.

[12] J. T. Foster, S. A. Silling, and W. W. Chen. Viscoplasticity using peridynamics. *International journal for numerical methods in engineering*, 81(10):1242–1258, 2010.

[13] Y. D. Ha and F. Bobaru. Studies of dynamic crack propagation and crack branching with peridynamics. *International Journal of Fracture*, 162(1-2):229–244, 2010.

[14] Y. D. Ha and F. Bobaru. Characteristics of dynamic brittle fracture captured with peridynamics. *Engineering Fracture Mechanics*, 78(6):1156–1168, 2011.

[15] E. Madenci and E. Oterkus. *Peridynamic theory and its applications*, volume 17. Springer, 2014.

[16] W. H. Gerstle. *Introduction to practical peridynamics: Computational solid mechanics without stress and strain*, volume 1. World Scientific Publishing Co Inc, 2015.

[17] S. V. Harren and R. J. Asaro. Nonuniform deformations in polycrystals and aspects of the validity of the taylor model. *Journal of the Mechanics and Physics of Solids*, 37(2):191–232, 1989.

[18] C. A. Bronkhorst, S. R. Kalidindi, and L. Anand. Polycrystalline plasticity and the evolution of crystallographic texture in fcc metals. *Philosophical Transactions of the Royal Society of London. Series A: Physical and Engineering Sciences*, 341(1662):443–477, 1992.

[19] R. Becker and S. Panchanadeeswaran. Effects of grain interactions on deformation and local texture in polycrystals. *Acta metallurgica et materialia*, 43(7):2701–2719, 1995.

[20] A. J. Beaudoin, H. Mecking, and U. F. Kocks. Development of localized orientation gradients in fcc polycrystals. *Philosophical Magazine A*, 73(6):1503–1517, 1996.

[21] S. Sun and V. Sundararaghavan. A peridynamic implementation of crystal plasticity. *International Journal of Solids and Structures*, 51(19):3350–3360, 2014.

[22] F. Roters, P. Eisenlohr, L. Hantcherli, D. D. Tjahjanto, T. R. Bieler, and D. Raabe. Overview of constitutive laws, kinematics, homogenization and multiscale methods in crystal plasticity finite-element modeling: Theory, experiments, applications. *Acta Materialia*, 58(4):1152–1211, 2010.

[23] H. Lim, C. C. Battaile, J. Carroll, T. E. Buchheit, B. Boyce, and C. Weinberger. Multi-scale modeling of plasticity in tantalum. Technical report, Sandia National Laboratories, Albuquerque, NM (United States), 2015.

[24] F. Roters, P. Eisenlohr, T. R. Bieler, and D. Raabe. *Crystal plasticity finite element methods: In materials science and engineering*. John Wiley & Sons, 2011.

[25] O. Engler and J. Hirsch. Texture control by thermomechanical processing of aa6xxx al-mg-si sheet alloys for automotive applications - a review. *Materials Science and Engineering: A*, 336(1-2):249–262, 2002.

[26] H. Inoue and T. Takasugi. Texture control for improving deep drawability in rolled and annealed aluminum alloy sheets. *Materials transactions*, 48(8):2014–2022, 2007.

[27] G. B. Burger, A. K. Gupta, P. W. Jeffrey, and D. J. Lloyd. Microstructural control of aluminum sheet used in automotive applications. *Materials Characterization*, 35(1):23–39, 1995.

[28] M. Matsuo. Texture control in the production of grain oriented silicon steels. *ISIJ international*, 29(10):809–827, 1989.

[29] V. Sundararaghavan and N. Zabaras. A multi-length scale sensitivity analysis for the control of texture-dependent properties in deformation processing. *International Journal of Plasticity*, 24(9):1581–1605, 2008.

[30] P. Acar and V. Sundararaghavan. Linear solution scheme for microstructure design with process constraints. *AIAA Journal*, pages 4022–4031, 2016.

[31] R. Liu, A. Kumar, A. Chen, A. Agrawal, V. Sundararaghavan, and A. Choudhary. A predictive machine learning approach for microstructure optimization and materials design. *Scientific reports*, 5:11551, 2015.

[32] E. M. Summers, R. Meloy, and S. M. Na. Magnetostriction and texture relationships in annealed galfenol alloys. *Journal of Applied Physics*, 105(7):07A922, 2009.

[33] G. B. Sarma, B. Radhakrishnan, and P. R. Dawson. Mesoscale modeling of microstructure and texture evolution during deformation processing of metals. *Advanced Engineering Materials*, 4(7):509–514, 2002.

[34] V. Sundararaghavan and N. Zabaras. Design of microstructure-sensitive properties in elasto-viscoplastic polycrystals using multi-scale homogenization. *International Journal of Plasticity*, 22(10):1799–1824, 2006.

[35] M. A. S. Qidwai, A. C. Lewis, and A. B. Geltmacher. Using image-based computational modeling to study microstructure–yield correlations in metals. *Acta Materialia*, 57(14):4233–4247, 2009.

[36] A. D. Kammers and S. Daly. Small-scale patterning methods for digital image correlation under scanning electron microscopy. *Measurement Science and Technology*, 22(12):125501, 2011.

[37] M. Calcagnotto, D. Ponge, E. Demir, and D. Raabe. Orientation gradients and geometrically necessary dislocations in ultrafine grained dual-phase steels studied by 2d and 3d ebsd. *Materials Science and Engineering: A*, 527(10-11):2738–2746, 2010.

[38] T. J. Ruggles and D. T. Fullwood. Estimations of bulk geometrically necessary dislocation density using high resolution ebsd. *Ultramicroscopy*, 133:8–15, 2013.

[39] M. D. Uchic, P. A. Shade, and D. M. Dimiduk. Plasticity of micrometer-scale single crystals in compression. *Annual Review of Materials Research*, 39:361–386, 2009.

[40] H. Abdolvand, M. Majkut, J. Oddershede, S. Schmidt, U. Lienert, B. J. Diak, P. J. Withers, and M. R. Daymond. On the deformation twinning of magnesium az31b: a three-dimensional synchrotron x-ray diffraction experiment and crystal plasticity finite element model. *International journal of plasticity*, 70:77–97, 2015.

[41] J. C. Stinville, M. P. Echlin, P. G. Callahan, V. M. Miller, D. Texier, F. Bridier, P. Bocher, and T. M. Pollock. Measurement of strain localization resulting from monotonic and cyclic loading at 650 degrees in nickel base superalloys. *Experimental Mechanics*, pages 1–21, 2017.

[42] R. J. Amodeo and N. M. Ghoniem. Dislocation dynamics. ii. applications to the formation of persistent slip bands, planar arrays, and dislocation cells. *Physical Review B*, 41(10):6968, 1990.

[43] D. Walgraef and E. C. Aifantis. Dislocation patterning in fatigued metals as a result of dynamical instabilities. *Journal of applied physics*, 58(2):688–691, 1985.

[44] H. M. Zbib, M. Rhee, and J. P. Hirth. On plastic deformation and the dynamics of 3d dislocations. *International Journal of Mechanical Sciences*, 40(2-3):113–127, 1998.

[45] T. Tang, S. Kim, and M. F. Horstemeyer. Fatigue crack growth in magnesium single crystals under cyclic loading: Molecular dynamics simulation. *Computational Materials Science*, 48(2):426–439, 2010.

[46] A. Cao, Y. Wei, and E. Ma. Grain boundary effects on plastic deformation and fracture mechanisms in cu nanowires: Molecular dynamics simulations. *Physical Review B*, 77(19):195429, 2008.

[47] S. V. Harren, H. E. Deve, and R. J. Asaro. Shear band formation in plane strain compression. *Acta Metallurgica*, 36(9):2435–2480, 1988.

[48] M. Zhang, F. Bridier, P. Villechaise, J. Mendez, and D. L. McDowell. Simulation of slip band evolution in duplex ti–6al–4v. *Acta materialia*, 58(3):1087–1096, 2010.

[49] E. Hornbogen and K. K. H. Z. Gahr. Distribution of plastic strain in alloys containing small particles. *Metallography*, 8(3):181–202, 1975.

[50] Z. P. Bazant, T. B. Belytschko, and T. P. Chang. Continuum theory for strain-softening. *Journal of Engineering Mechanics*, 110(12):1666–1692, 1984.

[51] M. P. Echlin, J. C. Stinville, V. M. Miller, W. C. Lenthe, and T. M. Pollock. Incipient slip and long range plastic strain localization in microtextured ti-6al-4v titanium. *Acta Materialia*, 114:164–175, 2016.

[52] R. J. Asaro and J. R. Rice. Strain localization in ductile single crystals. *Journal of the Mechanics and Physics of Solids*, 25(5):309–338, 1977.

[53] M. Dao and R. J. Asaro. Localized deformation modes and non-schmid effects in crystalline solids. part i. critical conditions of localization. *Mechanics of materials*, 23(2):71–102, 1996.

[54] M. Dao and R. J. Asaro. Non-schmid effects and localized plastic flow in intermetallic alloys. *Materials Science and Engineering: A*, 170(1-2):143–160, 1993.

[55] M. Dao and R. J. Asaro. Localized deformation modes and non-schmid effects in crystalline solids. part ii. deformation patterns. *Mechanics of materials*, 23(2):103–132, 1996.

[56] D. Zhou, J. C. Moosbrugger, and D. J. Morrison. Finite element simulation of psb macroband nucleation and propagation in single crystal nickel cycled at low plastic strain amplitudes. *International journal of plasticity*, 22(7):1336–1366, 2006.

[57] L. Anand and S. R. Kalidindi. The process of shear band formation in plane strain compression of fcc metals: Effects of crystallographic texture. *Mechanics of Materials*, 17(2-3):223–243, 1994.

[58] J. Oliver. A consistent characteristic length for smeared cracking models. *International Journal for Numerical Methods in Engineering*, 28(2):461–474, 1989.

[59] E. Samaniego and T. Belytschko. Continuum–discontinuum modelling of shear bands. *International Journal for Numerical Methods in Engineering*, 62(13):1857–1872, 2005.

[60] F. Armero and K. Garikipati. An analysis of strong discontinuities in multiplicative finite strain plasticity and their relation with the numerical simulation of strain localization in solids. *International Journal of Solids and Structures*, 33(20-22):2863–2885, 1996.

[61] V. Sundararaghavan and A. Kumar. Probabilistic modeling of microstructure evolution using finite element representation of statistical correlation functions. *International Journal of Plasticity*, 30:62–80, 2012.

[62] S. Sun and V. Sundararaghavan. A probabilistic crystal plasticity model for modeling grain shape effects based on slip geometry. *Acta Materialia*, 60(13-14):5233–5244, 2012.

[63] E. O. Hall. The deformation and ageing of mild steel: iii. discussion of results. *Proceedings of the Physical Society. Section B*, 64(9):747, 1951.

[64] N. J. Petch. The cleavage strengh of polycrystals. *Journal of the Iron and Steel Institute*, 174:25–28, 1953.

[65] L. F. Liu, L. H. Dai, and G. W. Yang. Strain gradient effects on deformation strengthening behavior of particle reinforced metal matrix composites. *Materials Science and Engineering: A*, 345(1):190–196, 2003.

[66] W. D. Nix and H. Gao. Indentation size effects in crystalline materials: a law for strain gradient plasticity. *Journal of the Mechanics and Physics of Solids*, 46(3):411–425, 1998.

[67] U. F. Kocks, C. N. Tomé, and H. R. Wenk. *Texture and anisotropy: preferred orientations in polycrystals and their effect on materials properties*. Cambridge university press, 2000.

[68] R. W. Armstrong, I. Codd, R. M. Douthwaite, and N. J. Petch. The plastic deformation of polycrystalline aggregates. *Philosophical Magazine*, 7(73):45–58, 1962.

[69] G. J. Weng. A micromechanical theory of grain-size dependence in metal plasticity. *Journal of the Mechanics and Physics of Solids*, 31(3):193–203, 1983.

[70] N. Nicaise, S. Berbenni, F. Wagner, M. Berveiller, and X. Lemoine. Coupled effects of grain size distributions and crystallographic textures on the plastic behaviour of if steels. *International Journal of Plasticity*, 27(2):232–249, 2011.

[71] B. Raeisinia, C. W. Sinclair, W. J. Poole, and C. N. Tomé. On the impact of grain size distribution on the plastic behaviour of polycrystalline metals. *Modelling and Simulation in Materials Science and Engineering*, 16(2):025001, 2008.

[72] M. D. Uchic, D. M. Dimiduk, J. N. Florando, and W. D. Nix. Sample dimensions influence strength and crystal plasticity. *Science*, 305(5686):986–989, 2004.

[73] D. M. Dimiduk, C. Woodward, R. LeSar, and M. D. Uchic. Scale-free intermittent flow in crystal plasticity. *Science*, 312(5777):1188–1190, 2006.

[74] J. R. Greer, W. C. Oliver, and W. D. Nix. Size dependence of mechanical properties of gold at the micron scale in the absence of strain gradients. *Acta Materialia*, 53(6):1821–1830, 2005.

[75] R. Maaß, S. Van Petegem, H. Van Swygenhoven, P. M. Derlet, C. A. Volkert, and D. Grolimund. Time-resolved laue diffraction of deforming micropillars. *Physical review letters*, 99(14):145505, 2007.

[76] K. S. Ng and A. H. W. Ngan. Effects of trapping dislocations within small crystals on their deformation behavior. *Acta Materialia*, 57(16):4902–4910, 2009.

[77] S. Li, W. Han, J. Li, E. Ma, and Z. Shan. Small-volume aluminum alloys with native oxide shell deliver unprecedented strength and toughness. *Acta Materialia*, 126:202–209, 2017.

[78] L. J. Sluys and Y. Estrin. The analysis of shear banding with a dislocation based gradient plasticity model. *International journal of solids and structures*, 37(46-47):7127–7142, 2000.

[79] J. Y. Shu and N. A. Fleck. Strain gradient crystal plasticity: size-dependent deformation of bicrystals. *Journal of the Mechanics and Physics of Solids*, 47(2):297–324, 1999.

[80] A. Acharya and A. J. Beaudoin. Grain-size effect in viscoplastic polycrystals at moderate strains. *Journal of the Mechanics and Physics of Solids*, 48(10):2213–2230, 2000.

[81] W. A. Counts, M. V. Braginsky, C. C. Battaile, and E. A. Holm. Predicting the hall-petch effect in fcc metals using non-local crystal plasticity. *International Journal of Plasticity*, 24(7):1243–1263, 2008.

[82] L. P. Evers, W. A. M. Brekelmans, and M. G. D. Geers. Scale dependent crystal plasticity framework with dislocation density and grain boundary effects. *International Journal of solids and structures*, 41(18):5209–5230, 2004.

[83] T. L. Warren, S. A. Silling, A. Askari, O. Weckner, M. A. Epton, and J. Xu. A non-ordinary state-based peridynamic method to model solid material deformation and fracture. *International Journal of Solids and Structures*, 46(5):1186–1195, 2009.

[84] D. Walgraef and E. C. Aifantis. Dislocation patterning in fatigued metals as a result of dynamical instabilities. *Journal of applied physics*, 58(2):688–691, 1985.

[85] M. Glazov, L. M. Llanes, and C. Laird. Self-organized dislocation structures (sods) in fatigued metals. *physica status solidi (a)*, 149(1):297–321, 1995.

[86] M. Ortiz and E. A. Repetto. Nonconvex energy minimization and dislocation structures in ductile single crystals. *Journal of the Mechanics and Physics of Solids*, 47(2):397–462, 1999.

[87] M. S. Breitenfeld, P. H. Geubelle, O. Weckner, and S. A. Silling. Non-ordinary state-based peridynamic analysis of stationary crack problems. *Computer Methods in Applied Mechanics and Engineering*, 272:233–250, 2014.

[88] M. R. Tupek and R. Radovitzky. An extended constitutive correspondence formulation of peridynamics based on nonlinear bond-strain measures. *Journal of the Mechanics and Physics of Solids*, 65:82–92, 2014.

[89] C. T. Wu and B. Ben. A stabilized non-ordinary state-based peridynamics for the nonlocal ductile material failure analysis in metal machining process. *Computer Methods in Applied Mechanics and Engineering*, 291:197–215, 2015.

[90] H. Ren, X. Zhuang, Y. Cai, and T. Rabczuk. Dual-horizon peridynamics. *International Journal for Numerical Methods in Engineering*, 108(12):1451–1476, 2016.

[91] D. J. Littlewood. A nonlocal approach to modeling crack nucleation in AA 7075-t651. In *ASME 2011 International Mechanical Engineering Congress and Exposition*, pages 567–576. American Society of Mechanical Engineers, 2011.

[92] E. Madenci, A. Barut, and M. Futch. Peridynamic differential operator and its applications. *Computer Methods in Applied Mechanics and Engineering*, 304:408–451, 2016.

[93] A. Yaghoobi and M. G. Chorzepa. Higher–order approximation to suppress the zero-energy mode in non-ordinary state-based peridynamics. *Computers and Structures*, 188:63–79, 2017.

[94] C. T. Dyka, P. W. Randles, and R. P. Ingel. Stress points for tension instability in sph. *International Journal for Numerical Methods in Engineering*, 40(13):2325–2341, 1997.

[95] R. Vignjevi, J. Campbell, and L. Libersky. A treatment of zero-energy modes in the smoothed particle hydrodynamics method. *Computer Methods in Applied Mechanics and Engineering*, 184(1):67–85, 2000.

[96] F. J. Harewood and P. E. McHugh. Comparison of the implicit and explicit finite element methods using crystal plasticity. *Computational Materials Science*, 39(2):481–494, 2007.

[97] S. A. Silling and R. B. Lehoucq. Convergence of peridynamics to classical elasticity theory. *Journal of Elasticity*, 93(1):13, 2008.

[98] F. Bobaru, M. Yang, L. F. Alves, S.A. Silling, E. Askari, and J. Xu. Convergence, adaptive refinement, and scaling in 1d peridynamics. *International Journal for Numerical Methods in Engineering*, 77(6):852–877, 2009.

[99] B. Kilic and E. Madenci. An adaptive dynamic relaxation method for quasi-static simulations using the peridynamic theory. *Theoretical and Applied Fracture Mechanics*, 53(3):194–204, 2010.

[100] R. J. LeVeque. *Finite difference methods for ordinary and partial differential equations: Steady-state and time-dependent problems*. SIAM, 2007.

[101] S. A. Silling and E. Askari. A meshfree method based on the peridynamic model of solid mechanics. *Computers and Structures*, 83(17-18):1526–1535, 2005.

[102] S. A. Silling. Stability of peridynamic correspondence material models and their particle discretizations. *Computer Methods in Applied Mechanics and Engineering*, 322:42–57, 2017.

[103] L. Anand and M. Kothari. A computational procedure for rate-independent crystal plasticity. *Journal of the Mechanics and Physics of Solids*, 44(4):525–558, 1996.

[104] J. Dolbow and T. Belytschko. A finite element method for crack growth without remeshing. *International Journal for Numerical Methods in Engineering*, 46(1):131–150, 1999.

[105] J. Luo, A. Ramazani, and V. Sundararaghavan. Simulation of micro–scale shear bands using peridynamics with an adaptive dynamic relaxation method. *International Journal of Solids and Structures*, 130:36–48, 2018.

[106] S. Sun. *Multiscale modeling of fracture in polycrystalline materials.* PhD thesis, University of Michigan, Ann Arbor, 2014.

[107] A. Kumar and V. Sundararaghavan. Simulation of magnetostrictive properties of galfenol under thermomechanical deformation. *Finite Elements in Analysis and Design*, 127:1–5, 2017.

[108] J. A. Zimmerman, D. J. Bammann, and H. Gao. Deformation gradients for continuum mechanical analysis of atomistic simulations. *International Journal of Solids and Structures*, 46(2):238–253, 2009.

[109] A. C. Eringen. On differential equations of nonlocal elasticity and solutions of screw dislocation and surface waves. *Journal of Applied Physics*, 54(9):4703–4710, 1983.

[110] P. Seleson and M. Parks. On the role of the influence function in the peridynamic theory. *International Journal of Multiscale Computational Engineering*, 9(6):689–706, 2011.

[111] J. Luo and V. Sundararaghavan. Stress-point method for stabilizing zero-energy modes in non-ordinary state-based peridynamics. *International Journal of Solids and Structures*, 2018.

[112] D. P. Flanagan and T. Belytschko. A uniform strain hexahedron and quadrilateral with orthogonal hourglass control. *International Journal for Numerical Methods in Engineering*, 17(5):679–706, 1981.

[113] R. W. Macek and S. A. Silling. Peridynamics via finite element analysis. *Finite Elements in Analysis and Design*, 43(15):1169–1178, 2007.

[114] P. R. Dawson and E. B. Marin. Processes using polycrystal plasticity. *Advances in Applied Mechanics*, 34:77, 1997.

[115] V. Sundararaghavan and N. Zabaras. A dynamic material library for the representation of single-phase polyhedral microstructures. *Acta Materialia*, 52(14):4111–4119, 2004.

[116] V. Sundararaghavan N. Zabaras. Linear analysis of texture–property relationships using process-based representations of rodrigues space. *Acta materialia*, 55(5):1573–1587, 2007.

[117] V. Sundararaghavan N. Zabaras. A statistical learning approach for the design of polycrystalline materials. *Statistical Analysis and Data Mining*, 1(5):306–321, 2009.

[118] P. Acar and V. Sundararaghavan. Utilization of a linear solver for multiscale design and optimization of microstructures. *AIAA Journal*, 54(5):1751 – 1759, 2016.

[119] P. Acar, V. Sundararaghavan, and M. DeGraef. Computational modeling of crystallographic texture evolution over cubochoric space. *Modelling and Simulation in Materials Science and Engineering*, 26(6):065012, 2018.

[120] P. Acar, S. Srivastava, and V. Sundararaghavan. Stochastic design optimization of microstructures with utilization of a linear solver. *AIAA Journal*, 55(9):3161–3168, 2017.

[121] P. Acar and V. Sundararaghavan. Uncertainty quantification of microstructural properties due to variability in measured pole figures. *Acta Materialia*, 124:100–108, 2017.

[122] P. Acar and V. Sundararaghavan. Uncertainty quantification of microstructural properties due to experimental variations. *AIAA Journal*, pages 2824–2832, 2017.

[123] O. Dmitrieva, P. W. Dondl, S. Müller, and D. Raabe. Lamination microstructure in shear deformed copper single crystals. *Acta Materialia*, 57(12):3439–3449, 2009.

[124] Cristian Teodosiu. *Large Plastic Deformation of Crystalline Aggregates*, volume 376. Springer, 1997.

[125] A. Githens, S. Ganesan, Z. Chen, J. E. Allison, V. Sundararaghavan, and S. Daly. Characterizing microscale deformation mechanisms and macroscopic tensile properties of a high strength magnesium rare-earth alloy: A combined experimental and crystal plasticity approach. *Acta Materialia (submitted)*, 2017.

[126] S. R. Agnew. Wrought magnesium: a 21st century outlook. *Jom*, 56(5):20–21, 2004.

[127] E. Solomon, A. Natarajan, A. Roy, V. Sundararaghavan, A. VanderVen, and E. Marquis. Stability and strain-driven evolution of β' precipitate in mg-y alloys. *Acta Materialia*, 166:148–157, 2019.

[128] S. N. Mathaudhu and E. A. Nyberg. Magnesium alloys in us military applications: Past, current and future solutions. In *Essential Readings in Magnesium Technology*, pages 71–76. Springer, 2016.

[129] S. Panwar, S. Sun, and V. Sundararaghavan. Modeling fatigue failure using the variational multiscale method. *Engineering Fracture Mechanics*, 162:290–308, 2016.

[130] P. Acar, A. Ramazani, and V. Sundararaghavan. Crystal plasticity modeling and experimental validation with an orientation distribution function for ti-7al alloy. *Metals*, 7(11):459, 2017.

[131] C. N. Tomé and G. C. Kaschner. Modeling texture, twinning and hardening evolution during deformation of hexagonal materials. In *Materials Science Forum*, volume 495, pages 1001–1006. Trans Tech Publ, 2005.

[132] G. C. Ganzenmüller, S. Hiermaier, and M. May. On the similarity of meshless discretizations of peridynamics and smooth-particle hydrodynamics. *Computers & Structures*, 150:71–78, 2015.

[133] L.K. Aagesen, J.F. Adams, J.E. Allison, W.B. Andrews, V. Araullo-Peters, T. Berman, Z. Chen, S. Daly, S. Das, S. DeWitt, and V. Sundararaghavan. Prisms: An integrated, open-source framework for accelerating predictive structural materials science. *JOM*, 70(10):2298–2314, 2018.

[134] V. Sundararaghavan and N. Zabaras. Classification and reconstruction of three-dimensional microstructures using support vector machines. *Computational Materials Science*, 32(2):223–239, 2005.

[135] V. Sundararaghavan. Reconstruction of three-dimensional anisotropic microstructures from two-dimensional micrographs imaged on orthogonal planes. *Integrating Materials and Manufacturing Innovation*, 3(1):19, 2014.

[136] A. Kumar, L. Nguyen, M. DeGraef, and V. Sundararaghavan. A markov random field approach for microstructure synthesis. *Modelling and Simulation in Materials Science and Engineering*, 24(3):035015, 2016.

[137] P. Acar and V. Sundararaghavan. A markov random field approach for modeling spatio-temporal evolution of microstructures. *Modelling and Simulation in Materials Science and Engineering*, 24(7):075005, 2016.

[138] M. R. Tupek, J. J. Rimoli, and R. Radovitzky. An approach for incorporating classical continuum damage models in state-based peridynamics. *Computer Methods in Applied Mechanics and Engineering*, 263:20–26, 2013.

[139] D. Kondo, H. Welemane, and F. Cormery. Basic concepts and models in continuum damage mechanics. *Revue Européenne de Génie Civil*, 11(7-8):927–943, 2007.

[140] S. Murakami. *Continuum damage mechanics: A continuum mechanics approach to the analysis of damage and fracture*, volume 185. Springer Science & Business Media, 2012.

[141] F. Bobaru, S. A. Silling, and H. Jiang. Peridynamic fracture and damage modeling of membranes and nanofiber networks. In *XI International Conference on Fracture, Turin, Italy*, 2005.

[142] M. L. Parks, P. Seleson, J. P. Steven, S. A. Silling, and R. B. Lehoucq. Peridynamics with LAMMPS: A user guide, v0.3 Beta. *Sandia Report (2011–8253)*, 2011.

[143] S. Sun and V. Sundararaghavan. Modeling crack propagation in polycrystalline microstructure using variational multiscale method. *Mathematical Problems in Engineering*, 2016(4715696):1 – 14, 2016.

[144] V. Sundararaghavan and S. Srivastava. Microfract: An image based code for microstructural crack path prediction. *SoftwareX*, 6:94–97, 2017.

[145] S. Sun, A. Ramazani, and V. Sundararaghavan. A hybrid multi-scale model of crystal plasticity for handling stress concentrations. *Metals*, 7(9):345, 2017.

[146] C. Heinrich and V. Sundararaghavan. A method to predict fatigue crack initiation in metals using dislocation dynamics. *Corrosion Reviews*, 35(4-5):325–341, 2017.

[147] S. Panwar and V. Sundararaghavan. Dislocation theory-based cohesive model for microstructurally short fatigue crack growth. *Materials Science and Engineering: A*, 708:395–404, 2017.

[148] S. Panwar, J. F. Adams, J. E. Allison, J. W. Jones, and V. Sundararaghavan. A grain boundary interaction model for microstructurally short fatigue cracks. *International Journal of Fatigue*, 113:401–406, 2018.

[149] S. Lee and V. Sundararaghavan. Calibration of nanocrystal grain boundary model based on polycrystal plasticity using molecular dynamics simulations. *International Journal for Multiscale Computational Engineering*, 8(5), 2010.

[150] S. Ganesan and V. Sundararaghavan. An atomistically-informed energy based theory of environmentally assisted failure. *Corrosion Reviews*, 33(6):455 – 466, 2015.

[151] V. Sundararaghavan and A. Waas. Non-local continuum modeling of carbon nanotubes: Physical interpretation of non-local kernels using atomistic simulations. *Journal of the Mechanics and Physics of Solids*, 59(6):1191–1203, 2011.

[152] S. Ghosh, A. Kumar, V. Sundararaghavan, and A. M. Waas. Non-local modeling of epoxy using an atomistically-informed kernel. *International Journal of Solids and Structures*, 50(19):2837–2845, 2013.

[153] S. Ghosh, V. Sundararaghavan, and A. M. Waas. Construction of multi-dimensional isotropic kernels for nonlocal elasticity based on phonon dispersion data. *International Journal of Solids and Structures*, 51(2):392–401, 2014.

[154] S. Forest. Modeling slip, kink and shear banding in classical and generalized single crystal plasticity. *Acta Materialia*, 46(9):3265–3281, 1998.

[155] V. Sundararaghavan, A. Kumar, and S. Sun. Crystal plasticity simulations using nearest neighbor orientation correlation function. *Acta Materialia*, 93:12–23, 2015.

[156] R. Zhu, J. Zhou, H. Jiang, and D. Zhang. Evolution of shear banding in fully dense nanocrystalline ni sheet. *Mechanics of Materials*, 51:29–42, 2012.

[157] C. Hirsch. *Numerical computation of internal and external flows: The fundamentals of computational fluid dynamics*. Butterworth-Heinemann, 2007.